DTU Library

Mode-III fracture characterization of composites

Sabbadin, Pietro

Publication date:
2020

Document Version
Publisher's PDF, also known as Version of record

Link back to DTU Orbit

Citation (APA):
Sabbadin, P. (2020). *Mode-III fracture characterization of composites*. Technical University of Denmark.

Mode-III fracture characterization of composites

Pietro Sabbadin

PhD Thesis

Mode-III fracture characterization of composites

Pietro Sabbadin

A thesis presented for the degree of
Doctor of Philosophy

DTU

Technical University of Denmark
Department of Mechanical Engineering
Lightweight Structures Group
March 2020

ii

I'll fail in the same way to understand with my reason why I pray, and yet I will pray—but my life now, my whole life, regardless of all that may happen to me, every minute of it, is not only not meaningless, as it was before, but has the unquestionable meaning of the good which it is in my power to put into it!

Anna Karenina, Lev Tolstoj

ii

PREFACE

This thesis is submitted to the Technical University of Denmark in partial fulfillment of the requirements for the degree of Doctor of Philosophy, Ph.D. The work has been carried out in the Lightweight Structures Group under the Section of Solid Mechanics, Department of Mechanical Engineering during the period from March 2017 to August 2020. The project was supervised by Associate Professor Christian Berggreen, Associate Professor Brian Nyvang Legarth and as external research consultant Professor Brian Hayman.

Interface debonding is studied when out-of-plane shear loads induce a local Mode-III stress state along the debond front in monolithic laminates and foam-cored sandwich structures. The debonding phenomenon is studied under the assumptions made by Linear Elastic Fracture Mechanics. In his work, a test procedure is developed involving analytical, numerical and experimental analyses.

Kgs. Lyngby, Denmark, April 2021

Pietro Sabbadin

iv

ABSTRACT

Composite monolithic laminates and sandwich materials are employed to build structures that demands a high stiffness to weight ratio, a high strength to weight ratio, good thermal and acoustic insulation and high capacity of energy absorption due to impact loads. Nowadays, composite materials are increasingly substituting metallic materials in different structural applications as in the aerospace, marine and wind energy sectors.

A composite sandwich structure can develop a wide variety of damages under static and fatigue loads. The principal kind of damages observed during the in-service life of a sandwich structure are: face-core interface debonding, core indentation, core-shear failure, face wrinkling and dimpling, shear crimping and general buckling. The robustness of a structural component can be affected by the aforementioned damages. Therefore, it is of vital importance that each different damage mode is meticulously analysed and studied in order to be able to predict the remaining life of a sandwich structure.

This PhD thesis deals with the analysis and fracture characterization of face-core interface debonding in foam-cored sandwich material systems and delaminations in monolithic laminates, when the defect is subjected to out-of-plane shear loads. The bonding strength of a disbond or a delamination can be assessed by determining the energy required to separate a unit area of the bonded material at the interface. This amount of energy is called fracture toughness and it is dependent on the mode-mixity present along the debond/delamination front. Several test fixtures and analytical models are present in the literature regarding interface fracture characterization of debonds/delaminations under mode-I, mode-II and mixed I-II modes. Instead, mode-III fracture characterization of debonds and delaminations is a less explored topic (especially for sandwich materials) and fewer test rigs and analytical models (respect to mode I-II characterization) are available in the literature.

First of all, an objective of this PhD thesis was to make a literature review of the developed test rigs and data reduction methods for mode-III fracture characterization of composite monolithic laminates. The different characteristics of the known test fixtures are illustrated and commented. The shear torsion bending (STB) test rig was identified as the one that provides the most uniform distribution of energy release rate (ERR) mode-III component along the delamination front. Therefore, the design of the novel test rig for mode-III fracture characterization of foam-cored sandwiches was inspired by the STB fixture.

A data reduction method is essential to compute the ERR in function of the external loads, material properties and geometry of the debonded/delaminated specimen. An improved data reduction method is first presented for the STB test designed for monolithic laminates. Subsequently, the applicability of the STB rig is extended to foam-cored sandwich composites subjected to out-of-plane shear loadings. The data reduction method

consists in an analytical model based on first order shear deformation theory, Vlasov theory for non-uniform torsion of beams and near tips effects are also taken into account. A 3D finite element model was build in order to verify the analytical model and generate both global and local predictions of the ERR distributions along the crack front.

Experimental results are shown and discussed in the last part of the thesis with the direct application of the analytical model used to extract the experimental fracture toughness values.

Resumé

Monolitiske laminater og sandwich-materialer anvendes til at bygge konstruktioner, der kræver et højt stivheds / vægtforhold og styrke / vægtforhold, god termisk og akustisk isolering og høj kapacitet for energiabsorption ved stødbelastninger. I dag erstatter kompositmaterialer i stigende grad metalliske materialer i forskellige strukturelle anvendelser som inden for luftfarts-, den maritime og vindenergi-sektoren. En sandwich-konstruktion kan udvikle en lang række skader under statisk og udmattelses-belastning. Den væsentligste form for skader, der observeres i løbet af en sandwich-konstruktions levetid, er: vedhæftningsfejl mellem skind og kerne, indtrykning i kernen, kerne-forskydningssvigt, wrinkling og dimpling, forskydningsbuling og generel buling. Robustheden af en strukturel komponent kan påvirkes af de ovennævnte skader. Derfor er det af afgørende betydning, at hver skadestype analyseres omhyggeligt for at kunne forudsige den resterende levetid af sandwich-strukturen. Denne ph.d.-afhandling beskæftiger sig med analyse og brudkarakterisering af skind-kerne vedhæftningsfejl i skum-kerne sandwich-materialesystemer og delamineringer i monolitiske laminater under påvirkning af ud-af-planet forskydningsbelastninger. Vedhæftningsstyrken af en sandwich vedhæftningsfejl eller en delaminering i et laminat kan vurderes ved at bestemme den nødvendige energi til at adskille et enhedsareal af materialet ved revnespidsen. Denne mængde energi kaldes brudenergien, og den er afhængig af forholdet mellem brud-formerne (mode-I, II og III) langs med vedhæftningsfronten. Flere testmetoder og analysemodeller findes i litteraturen vedrørende karakterisering af brudenergien under mode-I, mode-II og blandede mode I-II-tilstande. Mode-III-brudkarakterisering af sandwich vedhæftningsfejl og delamineringer i lamianter et et mindre udforsket emne i litteraturen (især for sandwich-materialer). Først og fremmest var et mål med denne ph.d.-afhandling at foretage en litteratur-gennemgang af de udviklede test-fiksturer og datareduktionsmetoder til mode-III karakterisering af brudegenskaber for monolitiske laminater. De forskellige egenskaber ved de kendte test-fiksturer er illustreret og kommenteret. Test-fiksturet til forskydnings-torsions-bøjning (STB) blev identificeret som det fikstur, der giver den mest ensartet fordeling af mode-III-komponenten af energifrigivelsesrate (ERR) langs delaminerings-fronten. Derfor blev designet af det nye test-fikstur til mode-III-brudkarakterisering af skumkerne sandwich-materialer inspireret af STB-fiksturet. En valid data-reduktionsmetode er afgørende for at beregne ERR som funktion af de påførte belastninger, materialegenskaber og geometri af test-emnet. En forbedret data-reduktionsmetode præsenteres først til STB-testen beregnet til monolitiske laminater. Derefter udvides anvendelsen af STB-riggen til skumkerne sandwich-kompositter, der udsættes for forskydningsbelastninger ud-af-plan. Data-reduktionsmetoden består i en analytisk model baseret på første ordens forskydnings-deformationsteori, hvor der tages også højde for Vlasov-teori for ikke-ensartet vridning af bjælker. En 3D FEM model blev bygget op for at verificere den analytiske model og generere både globale og lokale forudsigelser af ERR-fordelingen langs revnefronten. Eksperimentelle resultater er vist og diskuteret i

den sidste del af afhandlingen med direkte anvendelse af analysemodellen, der anvendes til at uddrage de eksperimentelle værdier for brudenergien.

Publications

Journal papers

[P1] An improved analysis of a STB specimen for fracture characterization of laminates and foam-cored sandwich composites under mode III loads. *Published June 2020, Engineering Fracture Mechanics.*

[P2] A novel test fixture for mode III fracture characterization of monolithic laminates and composite sandwich specimens. *Submitted to Journal of Composite Materials.*

Conference papers

[C1] Development of a Data Reduction Method for Composite Fracture Characterization Under Mode III Loadings. *Published in Springer Nature, AIMETA 2019 LNME proceedings.*

x

CONTENTS

List of Figures

List of Tables

Nomenclature

Greek Symbols

$(E\Gamma)_i$	Warping stiffness of a delaminated arm section	$[mm^6]$
κ_d	Shear correction factor for the upper arm	[-]
κ_s	Shear correction factor for the lower arm	[-]
θ_z^i	Angle of twist along the z-axis of a beam section	$[rad]$
$\varphi_d(z)$	Rotation of the section of the upper delaminated arm around the x-axis	$[rad]$
$\varphi_s(z)$	Rotation of the section of the lower delaminated arm around the x-axis	$[rad]$

Indices

d, s	Indices for upper delaminated facesheet and lower substrate
LAM, SAN	Indices referring either to the monolithic laminate or the sandwich
r	Index indicating the term *rotational*
t	Index indicating the term *translational*

Latin Symbols

a	Crack length	$[mm]$
b	Specimen width	$[mm]$
E_c	Elastic Young modulus of the core	$[N/mm^2]$
E_f	Longitudinal Young modulus of the facesheet	$[N/mm^2]$
G	Energy release rate	$[N/m]$
G_c	Elastic shear modulus of the core	$[N/mm^2]$
G_f	Elastic shear modulus of the facesheet	$[N/mm^2]$
h	Height of the load tabs	$[mm]$
k_r^d	Stiffness of the rotational spring of the upper delaminated arm	$[Nmm]$
k_r^s	Stiffness of the rotational spring of the lower delaminated arm	$[Nmm]$

k_t^d Stiffness of the translational spring of the upper delaminated arm $[N/mm]$

k_t^s Stiffness of the translational spring of the lower delaminated arm $[N/mm]$

L Total specimen length $[mm]$

M_X Moment acting on delaminated arms along the X-axis $[N/mm]$

$M_x^d(z)$ Moment acting along the x-axis on the upper delaminated arm $[N/mm]$

$M_x^s(z)$ Moment acting along the x-axis on the lower delaminated arm $[N/mm]$

$M_z(z)$ Moment along the z-axis acting on a delaminated arm at coordinate z $[N/mm]$

M_Z^d Moment acting on the upper delaminated arm along the Z-axis $[N/mm]$

M_Z^{Rd} Reaction moment acting on the upper load tab in the Z-direction $[N/mm]$

M_Z^{Rs} Reaction moment acting on the lower load tab in the Z-direction $[N/mm]$

M_Z^s Moment acting on the lower delaminated arm along the Z-axis $[N/mm]$

P External load $[N]$

P^R Reaction force acting on the upper load tab in the Y-direction $[N]$

t_c Core thickness $[mm]$

t_f Face-sheet thickness $[mm]$

$u_y^d(z)$ Vertical displacement of the shear center axis of the upper delaminated arm $[mm]$

$u_y^s(z)$ Vertical displacement of the shear center axis of the lower delaminated arm $[mm]$

$V_y^d(z)$ Shear force acting on the upper delaminated arm $[N]$

$V_y^s(z)$ Shear force acting on the lower delaminated arm $[N]$

W Width of the bonded part of the specimen $[mm]$

X, Y, Z Axes labels of coordinate reference system for the specimen $[-]$

x, y, z Axes labels of coordinate reference system for the structural model $[-]$

1. Introduction

An introduction to composite monolithic and sandwich structures is made to explain what a composite structure is and give a brief background on the practical applications of monolithic and sandwich composite materials. Moreover, the different types of failure modes are introduced along with the motivation that has driven the work presented in this PhD thesis.

1.1 Background: monolithic and sandwich composite structures

A composite structure usually consists of a multi-material system that is used to build structural components that can carry different types of external loads. Monolithic or sandwich composite structural components are often built as flat or curved panels in different kind of industrial sectors as: the automotive, the aerospace, the transportation and the marine sectors (see fig. 1.1). Beam components made of monolithic and sandwich composite materials are less often employed as primary structural components.

Figure 1.1. Typical examples of primary users of sandwich composites.

A monolithic composite laminate is usually composed of glass or carbon fibers impregnated by a specific resin system. Instead, a sandwich composite panel usually consists in a symmetrical tri-material system. This tri-material system is composed of two face sheets (monolithic laminates) of thickness t_f and a core of thickness t_c. As fig. 1.2 shows, the core is located between the two face sheets. This geometrical layout reflects the structural

functions of the face sheets and of the core. In fact, the two face sheets carry the majority of the external bending loads since they are positioned far away from the neutral plane of the layup and because they are made of a stiffer material respect to the core. Instead, the core has two duties: first to withstand the out-of-plane shear loads and second to physically connect the two face sheets. Core and face sheets are adhesively bonded together. The overall bending stiffness can be obtained using the parallel axis theorem as follows:

$$(EI)_{eq} = 2E_f I_f + E_c I_c \qquad (1.1)$$

where E_f and E_c are the longitudinal Young moduli of the face sheets and of the core, and I_f and I_c are the second moment of inertia of the face sheets section and the core section. Fig. 1.2 shows how a sandwich composite can be regarded as an I-beam where the two face sheets constitute the two beam flanges and the core is equivalent to the web.
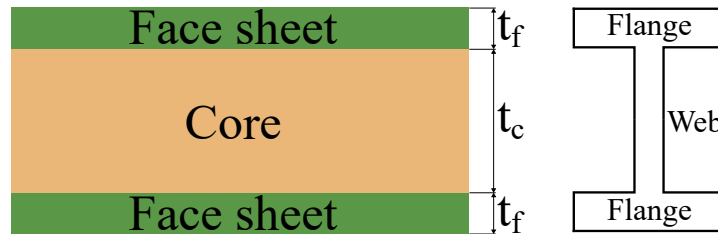
Figure 1.2. Representation of a sandwich structure and comparison with an I-beam.

The high values of bending and shear stiffness to weight ratios are what make sandwich composite standing out (from a structural mechanics point of view) respect monolithic laminates and metals. Core and face sheets material are chosen based on the application needs. The core is usually selected between those materials that have a low density ($\backsim 10 - 250 \ kg/m^3$) and lower values of linear elastic moduli respect to the one of the faces sheets. Moreover, the core should resit to buckling failure and it should has a good compressive and out-of-plane shear strength and stiffness. Instead, face sheets are materials with a higher longitudinal Young modulus (respect to the core) and high bending strength.

In general, the core is the weaker constituent of the sandwich structure. The material combinations that can be chosen for the face sheets and for the core are enormous. Glass fiber or carbon fiber monolithic laminates are usually used as face sheets. The core is usually chosen between: opened/closed cell polymeric or metal foams, balsa wood or honeycomb structures. The material choice is always based on the specific application. The savings on the structure weight are directly related to the economical advantages that sandwich materials can offer when a composite structure is made. Sandwich materials are chosen in cost sensitive applications, where they are even more in competition with monolithic construction as the aerospace and the marine sectors.

Sandwich constructions use light weight cores whose cost is comparatively lower than metals. Tab. 1.1 shows a study presented in [1] on the weight saving and the material cost saving potential using an expensive core and a low cost core, compared to using a monolithic laminate made of the same material of the sandwich face sheets. It can be seen that economical advantage of using a low cost core material is as big as the weight saving due to the low density of the core itself.

A simple example (taken from [1]) is provided here in order to further understand why sandwich composites are often used in cost sensitive structures. This example takes into consideration a beam subjected to a three point flexure load. Two cases are considered here: the beam is made of a monolithic laminate (first case) and the beam is made out of a sandwich composite. The comparison uses as comparing parameters the so-called material efficiency per weight $ME_W = E^{1/3}/\rho$ and the material efficiency per material cost $ME_{CM} = E^{1/3}/C_W\rho$ where C_W is the material cost per kilogram. Figs. 1.2 and 1.3 show a comparison between different monolithic material and different sandwich material options for a simple supported three point bending beam load case. The maximum allowable deflection w is set along with the span length l and the width b. Since w is set, the bending stiffness for the different material combination should remain constant. Therefore, the only parameter that can be changed is h leading to different weights and material costs.

	Laminate	Sandwich 1	Sandwich 2
Relative thickness	1	1.2	2.4
Relative bending stiffness	1	1	1
Relative weight	1	0.345	0.177
Relative material cost with expensive core	1	1.2	2.4
Relative material cost with low cost core	1	0.345	0.177

Table 1.1. Summary of a comparison between a laminate and a sandwich plate made in [1].

Table 1.2 illustrates ME_W and ME_{CM} for different types of monolithic laminates. It can be clearly seen that the most cost and weight efficient material configuration is the one using the GFRP woven, even if it has not the lowest beam height h. While, tab. 1.3 represents the performance of a sandwich combination compared with the best monolithic laminate configuration from the previous analysis step. Hence, the face sheets are chosen as GFRP woven laminates coupled with a low cost (e.g. paper honeycomb) core with a thickness ratio $t_f/h = 0.125$ and $t_f/h = 0.0125$ under the same loading conditions. It is obvious how the use of a composite sandwich brings to a more cost efficient solution. The sandwich configuration is 5.66 times less expensive than the GFRP monolithic laminate configuration, where the GFRP solution is the most cost effective between the others configurations between the laminates (see fig. 1.2).

Material	E $[GPa]$	ρ $[kg/dm^3]$	C_W $euro/kg$	ME_W	ME_{CM}
Steel	210	7.8	0.6	0.76	1.27
Aluminium	72	2.7	2.0	1.54	0.77
Polypropylene	1.2	0.9	1.0	1.18	1.18
GFRP	20	1.7	3.3	1.60	0.48

Table 1.2. Summary of a comparison study between different monolithic materials made in [1].

Material	t_f/h	E $[GPa]$	ρ $[kg/dm^3]$	C_W $euro/kg$	ME_W	ME_{CM}
Laminate	0.5	20	1.7	3.3	1.60	0.48
Sandwich 1	0.125	11.56	0.49	3.3	4.61	1.40
Sandwich 2	0.0125	1.46	0.125	3.3	9.08	2.75

Table 1.3. Summary of a comparison study between a monolithic laminate and a sandwich plate subjected to 3 point bending made in [1].

It is clear now, why composite sandwich materials are widely used in the industry to build structures in which the strength to weight ratio has to be optimized under a reasonable cost. More useful information for material selection can be found in [2–4]. The drawbacks of using composite sandwich is the high number of different failure modes that this kind of material systems exhibit if compared to e.g. metals. The damages that can be present in a sandwich structure are discussed in the next section.

1.2   Damage types in Sandwich Structures

The types of failure associated with composite sandwich materials must to be studied accurately, if structural components have to be robust throughout all their in-service period. A damage can be introduced either during the manufacturing process or it can initiate and propagate during the in-service period. The most common types of damages that a sandwich structure can encounter are [5–7]: face-core interface debonding, core indentation, core-shear failure, face wrinkling, shear crimping and buckling either of the face-sheets or of the core. In fig. 1.3 are reported some cases of component failures due to the presence of in-service or manufacturing damages.

(a)

(b)

(c)
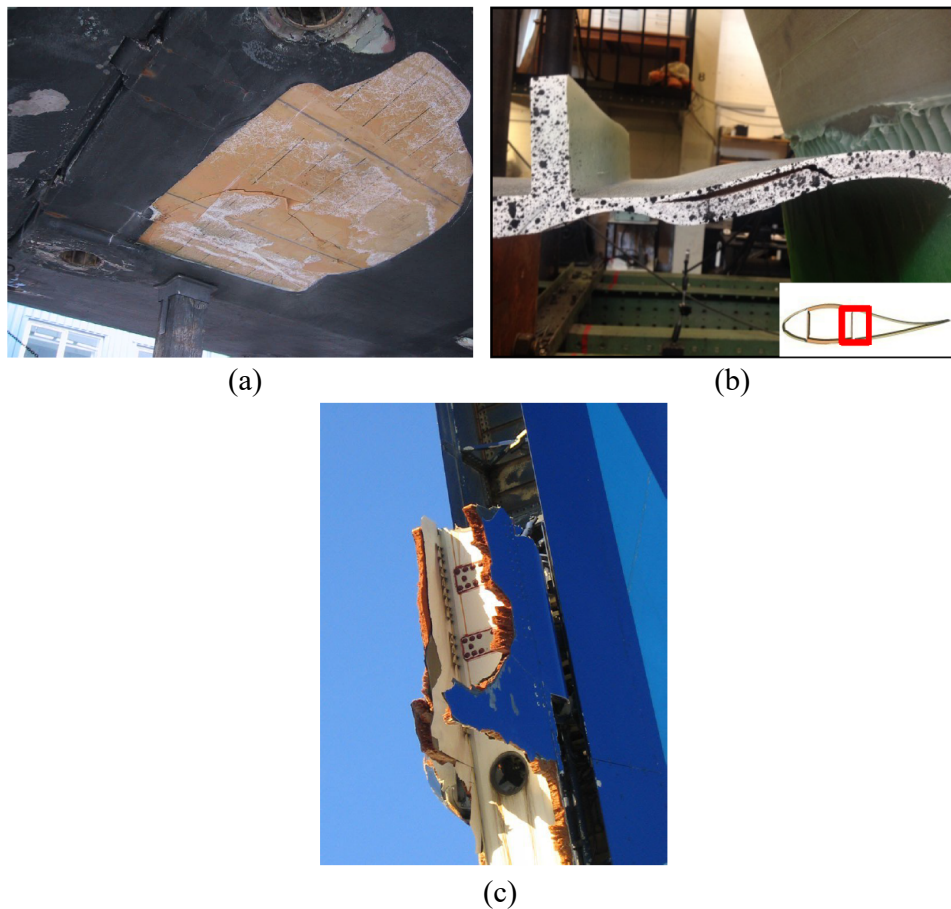
Figure 1.3.   Illustration of failures in sandwich structures due to propagation of damages. (a) Face/core debond on a ship-hull; (b) face/core debond and crack kinking in a wind turbine blade component; (c) failure of an airplane rudder made of honeycomb core.

The damage detection is not an easy task, because most of the times the damage is not visible from outside the structure. Usually, a damage lies beneath the surface of a component and therefore it is not easy to detect by visual inspection. Moreover, a component should be inspected without damaging it, using non-destructive damage detection techniques. A lot of efforts and work regarding non-destructive damage detection techniques can be found in the SANDI project [8] carried out by Det Norske Veritas in 2007.

The type of damage studied in this work is the debond between the face sheet and the core of a composite sandwich. A debond consits in a lack of adhesion between the

core and the the face sheet. Debonds can generally be present as manufacturing defects or they can develop and grow under the service period of the structural component. If adhesion between the face sheet and the core does not exist, the bending loads are no longer transmitted to the face sheet leading both to a degradation of the compliance of the component and a possible failure either of the face sheets or of the core. Therefore, a debond can be the cause of collapse of a structural component as reported in different studies for different types of structures e.g.: the structural failure of an airplane rudder [5], of a fuel tank in the aerospace sector [9] and of a wind turbine blade under cyclic loadings [10]. Hence, the face-core interface must be characterized in order to provide a reliable assessment of robustness of a damaged structural component.

The bonding strength of an interface can be quantified by measuring a physical parameter defined as fracture toughness. The fracture toughness is a material property of the interface itself and it is expressed in units of energy [J]. Studies on sandwich composite [11–13] observed that the fracture toughness depends on the local value of the mode-mixity between the different fracture modes at the debond tip. Several mode I/II experimental fracture characterizations tests have been developed like: the crack sandwich beam (CSB) [14], the double cantilever sandwich beam (DCB) [15], the tilted sandwich debond specimen (TSD) [16], the three point sandwich beam (TPSB) [17] and the DCB specimen subjected to uneven bending moment [18]. The mentioned studies offer a solid basis for fracture characterization testing technique for mode I/II damage propagation.

The need of tests for mode III fracture characterization comes from real-life engineering scenarios where a mixed mode I/II state is present along the debond front along with a non-negligible mode III component of the energy release rate. The study in [19] reports the case (taken from the marine sector) of a circular disbond in a plate subjected to compressive loads. The distribution of the energy release rate presents two peaks of mode III component along two specific positions of the circular crack. These two mode III peaks are 9 % of the mode I/II component and therefore mode III influences the propagation of the crack. Hence, the assessment of mode III fracture toughness is fundamental in order to accurately predict the crack propagation path. The presence of the mode-III energy release rate component is non-negligible in structural details that are really common in composite structures: lap joints subjected to in-plane loads. The eccentricity of external loads and the finite width of lap joints promote the presence of a mixed mode I-III energy release rate state at traction free edges of the joint as reported in [20–22]. Another work presented in [10] shows how shear loads (which induce a dominant mode III stress state along the debond front) can be detrimental for the structural integrity of a wind turbine blade component made of sandwich composite when a debond between the face and the core is present. Thus, several studies [23–26] have been carried out to measure the fracture toughness of monolithic composite laminates when the debond front is under out-of-plane loadings. All the experimental tests carried out in [23–26] are realized at coupon level, because they are meant to measure a material property. Fig. 1.4 shows the different scales at which a structural test can be performed. All the tests that will be presented are considered as coupon level tests.
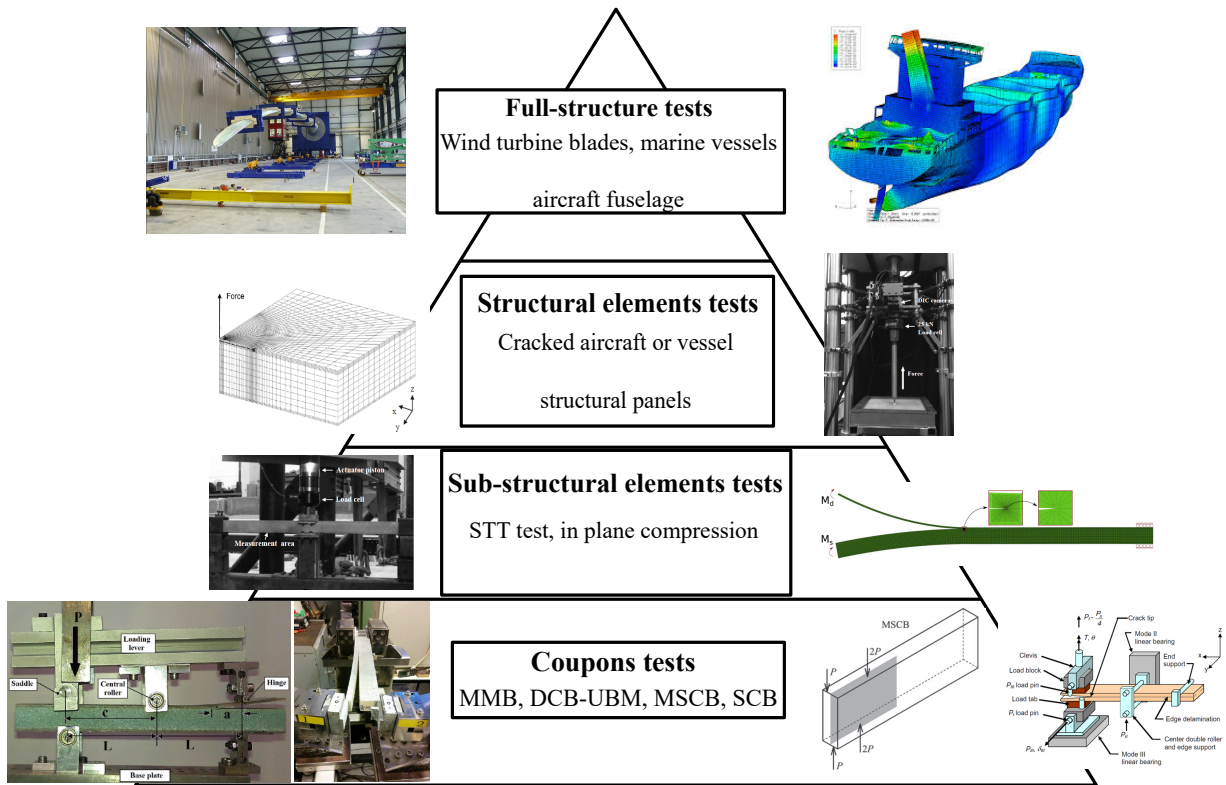
Figure 1.4. Different scales for structural experimental testing.

1.3 Research Aims and Achievements

The structural failure of composite sandwich structures (due to presence of damages) can be assessed and avoided if the guidelines presented in [27, 28] are followed. However, fracture mechanics based tools are necessary to study the most complex problems as the ones related to face/core debonds. Moreover, debond damages are not yet addressed in a complete and exhaustive manner in [27, 28]. The debond growth under the most general load scenario must be studied in order to ensure the safe usage of composite sandwich for future applications. A bottom-up approach (from coupon test specimens to tests on structure level, fig. 1.4) should be adopted in order to understand exhaustively the debond growth phenomenon. Additionally, it is of paramount importance that the analytical, numerical and experimental studies concur, in order to let the industry to assess accurately the remaining structural life of a damaged component.

The use of numerical simulations can assess the propagation of a debond present in a large composite sandwich structure as it can be the rotor of a wind turbine blade, a fuselage of an aircraft or a hull of a ship. However, the numerical tools need as an input the value of the fracture toughness of that specific interface. Hence, it is important to measure the fracture toughness through fracture mechanics test at coupon level (see fig. 1.4). Then, numerical simulations can be performed at sub-structural and structural scale levels using the fracture toughness values measured previously. Finally, the full damaged structure can be studied after having gained the confidence in handle the fracture mechanics approach at lower structural scale levels.

The work presented in this thesis focuses on the lowest group in the pyramid represented

in fig. 1.4. A successful analysis at the full-structure scale is possible only if accurate results are extracted from fracture mechanics tests at coupon level. Several standards are available [29–32] that use linear elastic fracture mechanics tools in order to characterize delamination surfaces of monolithic composite laminates under static and fatigue loads. However, little effort is done regarding the fracture characterization of delaminations and debonds subjected to out-of-plane shear forces in monolithic laminates and composite sandwiches. The term out-of-plane refers to forces that act in planes parallel respect the crack plane but orthogonally respect to the crack propagation direction. Out-of-plane loads generate a dominant anti-plane stress field along the debond front. Consequently, an anti-plane stress field is represented by the mode III opening of a crack in the Linear Fracture Mechanics theory.

In order to have a measurement of the the fracture toughness under the complete spectrum of mode mixities (between mode I-II-III) it is of enormous importance to develop an new experimental procedure. This procedure consists in the design of a novel test fixture capable of performing mode III dominated fracture tests to characterize delaminations and debonds in monolithic composite laminates and sandwich specimens. The design of the test rig and of the specimen are guided by an analytical and a numerical analyses. Therefore, the development of an analytical model, used as data reduction method for the experimental test, is carried out. The analytical model is bechmarked against a numerical model. Experimental tests on both monolithic laminates and foam-cored sandwich specimens are performed.

Two journals articles [P1] and [P2] and one conference paper are the result of the PhD work presented in this thesis.

1.4   Thesis Outline

This section provides a summary of the PhD thesis content. Firstly, the fracture mechanics of interfacial cracks in dissimilar anisotropic solids is presented. This theoretical tool is necessary in order to carry out the numerical analysis that study the displacement field close to the debond front. Secondly, a literature review, about the studies regarding delaminations and debonds subjected to anti-plane loads in sandwich structures, is provided. Thirdly, the analytical analysis that allows to describe the structural behaviour of the specimen is presented. Then, the numerical model is presented along with a comparison between the analytical and numerical results. Finally, the test rig is presented and the experimental results are listed in a final comparison with the analytical and FE results. A short summary of the chapters is presented below:

Chapter 2: The fracture mechanics solutions for interface crack in dissimilar anisotropic materials are presented. Moreover, an introduction to the Crack Surface Extrapolation (CSDE) method is briefly outlined.

Chapter 3: This chapter presents a background on the solutions for the anti-plane problem in the fracture mechanics of interfaces. Moreover, a literature review on presenting the test rigs already designed for anti-plane fracture characterization tests is carried out. Each tests rig and data reduction in presented in detail and the positive and negative aspects are highlighted.

Chapter 4: The analytical model for experimental data reduction method is presented.

The assumptions on the loads, geometry and material behaviour are explained and reported. Moreover, the numerical model is presented along with the implementation of the CSDE method to extract the energy release rate. A comparison between the analytical and numerical results is done in order to verify the goodness of the assumptions made to build the analytical model. Results from fracture characterization tests are presented for monolithic laminate and foam-core sandwich specimens.

Chapter 5: A novel test fixture for mode III fracture characterization is presented along with experimental results both for the monolithic laminate and the composite sandwich specimens. The data reduction method presented in Chapter 4 is applied to the experimental data in order to compute the critical values of the mode-III energy release rate in function of the applied loads. Considerations are illustrated and discussed about the non linear behaviour (observed in the experimental tests) of foam-cored sandwich specimens.

2. FRACTURE MECHANICS OF INTERFACE CRACKS

The specimen and test rig design is based on the distribution of the energy release rate G along the crack front in the delaminated monolithic laminate or sandwich specimen. In order to study the distribution of G along the crack front Linear Elastic Fracture Mechanics (LEFM) theory is used. The aim of this chapter is to introduce the concepts of LEFM for a crack embedded in a homogeneous and isotropic material and subsequently for an interfacial crack between two dissimilar orthotropic materials.

2.1 Linear Elastic Fracture Mechanics

Almost a century ago, Alan Griffith studied the rupture of brittle materials applying the first law of thermodynamics. The foundations of Linear Elastic Fracture Mechanics were laid by Griffith himself in his pioneering work [33]. Alan's griffith work was motivated to explain the discrepancy between the theoretical strength of a material and its effective strength. Griffith postulated that the bulk of all brittle materials contain several flaws in the form of microcraks that act as stress concentrators. This new idea along with his energetic approach started the application of Linear Elastic Fracture Mechanics to solve engineering problems.

Griffith's energy point of view observes that when a crack propagates in an elastic body, the energy involved in the fracture process must experience a transformation. In fact, Griffith [33] states that the unstable propagation of a crack is followed by a decrease in the strain energy of the system (when no work is done by external forces, e.g. in an elastic body with fixed boundary). The crack advances when the increment of release energy dW associated with a crack extension da overcomes the increment of surface energy dW_s necessary to create two new surfaces after the crack extension. In mathematical terms:

$$dW \geqslant dW_s \qquad (2.1)$$

where the equal sign in eq. (2.1) indicates the critical point for crack propagation. In more simple words, if the energy available in the elastic body exceeds the energy required to create new crack surfaces then the crack can extend. Now, the elastic potential can be introduced for a cracked body as:

$$\Pi = W_f - U \qquad (2.2)$$

where W_f is the work done by the external forces and U is the strain energy transferred into the elastic body due to the application of the external forces. As remarked in [34],

Irwin proposed that the energy-release rate can be used as the parameter that quantifies the energy available for crack propagation:

$$G = -\frac{d\Pi}{dA} \tag{2.3}$$

where A is the area on which incremental crack growth takes place. During a crack extension of da, the work done by the external forces dW_f equals the sum between the variation of the body strain energy dU and the increment of surface energy dW_s when an adiabatic transformation is considered:

$$dW_f = dU + dW_s. \tag{2.4}$$

The critical energy required to create an increment of the crack area is called fracture toughness G_c. Hence, crack propagation only occurs when the externally supplied energy equals the fracture toughness, therefore when $G \geqslant G_c$.
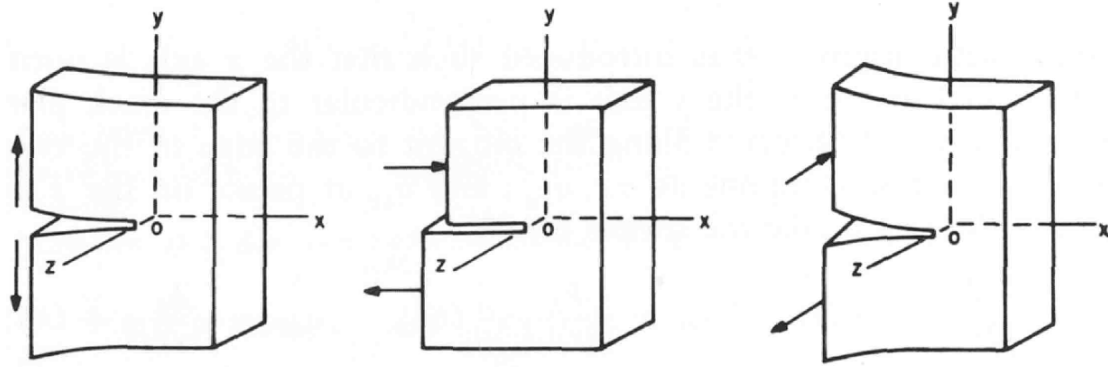
Figure 2.1. Illustration of the crack opening modes; from left to right: mode-I (opening), mode-II (in-plane shear) and mode-III (out-of-plane shear)

The all possible crack opening configurations can be obtained by the linear super-positions of three different opening modes depicted in fig. 2.1. Thus, the value for the energy release rate can be in principle decomposed in three different contributions that correspond to the three opening modes illustrated in fig. 2.1. The three energetic terms can be combined linearly between each other for a crack in a isotropic and homogeneous body:

$$G = G_I + G_{II} + G_{III}. \tag{2.5}$$

Mode-I and II are coupled and 2.5 does not hold (see next section) if the crack is located at an interface between two dissimilar materials. The stress field in close proximity of the crack tip can be described by the stress intensity factors as reported by Irwin in [34] for a homogeneous and isotropic body. The local stress field for a crack embedded in a isotropic, homogeneous and elastic media can be written in polar coordinates as:

$$\sigma_{ij} = \frac{K_I}{\sqrt{2\pi r}}\sigma_{ij}^I(\theta) + \frac{K_{II}}{\sqrt{2\pi r}}\sigma_{ij}^{II}(\theta) + \frac{K_{III}}{\sqrt{2\pi r}}\sigma_{ij}^{III}(\theta) + T(r,\theta)\delta_{i1}\delta_{1j} \tag{2.6}$$

where K_I, K_{II} and K_{III} are the stress intensity factors; $\sigma_{ij}^I(\theta)$, $\sigma_{ij}^{II}(\theta)$ and $\sigma_{ij}^{III}(\theta)$ are functions of the polar coordinate θ; $T(r,\theta)$ is the so call T-stress function that represents

the non-singular stress field far away from the crack tip; δ_{ij} is the Kronecker's delta. The solution reported in eq. (2.6) is valid for plane strain/plane stress and pure anti-plane conditions. If mode-I and mode-II are present at the same time at the crack tip a new parameter, called mode-mixity ψ, can be defined. The mode-mixity defines a relation between mode-I and mode-II stress intisity factors as:

$$\psi = \arctan\left(\frac{K_{II}}{K_I}\right). \tag{2.7}$$

Irwin introduced a relationship between the stress intensity factors and the energy release rate for a crack in a homogeneous and isotropic elastic body:

$$G = \frac{K_I^2 + K_{II}^2}{E^*} + \frac{K_{III}^2}{2\mu} \tag{2.8}$$

where E^* is the young modulus of the material for plane stress or plane strain conditions and μ is shear modulus. E^* can be expressed for the two different conditions as:

$$E^* = E \quad \textit{plane stress} \tag{2.9a}$$

$$E^* = \frac{E}{1 - \nu^2} \quad \textit{plane strain} \tag{2.9b}$$

The stress field solutions eq. (2.6) are often used when cracks in isotropic and homogeneous materials are studied. Although, a complex analytical solution exists for a crack lying at an interface between dissimilar linear elastic materials. In this case, the local stress field is characterized by a complex stress intensity factor and a real stress intensity factor. Due to the complex nature of K and its non intuitive physical meaning, the stress approach is abandoned to study interface cracks as debonds and delaminations. An energetic approach, that uses the energy release rate G and the mode-mixity ψ, is used when cracks in dissimilar elastic media are studied. The fracture mechanics of interface crack is presented in the next section.

2.2 Interface Fracture Mechanics

Composite sandwich materials are employed in very different sectors, from the micro-electronics to the aerospace sector. Layered materials consist in bonding materials, having different mechanical properties, together. This process allows for the presence of interfaces between different layers of materials. Thus, the mismatch in the elastic properties between interfaces generate complex stress and strain fields in the proximity of the interface. The linear elastic solutions to interface cracks are provided by Suo and Beom in [35, 36].

Cracks in homogeneous media tend to propagate always in mode-I conditions regardless the initial orientation of the crack respect to the load direction. This happens because mode-I is the more favourable condition for crack propagation from an energetic point of view. Since the crack can kink freely in an homogeneous elastic body, it always aligns itself along a plane of maximum principal stress. The behaviour for interface crack is different. In fact, an interfacial crack is contained between two layers of different stiffness

and different toughness. The mismatch in stiffness is given either by the different fibre orientation of two consecutive plies in monolithic laminates, or by the fact that two dissimilar materials are bonded between each others. Thus, an interface crack is not free to kink and reach the plane of maximum principle stress because it is constrained to propagate along the bonding interface between plies or between the face and the core in a sandwich. As a matter of fact, the toughness of the interface is usually lower respect the one of the facesheet and the core. Accordingly, the crack propagates at the interface where mixed-mode conditions are present at the crack tip. A final remark is made regarding the notation used to express the stress intensity factors: roman numbers are used to indicate the stress intensity factors relative to crack problem in homogeneous media, instead latin numbers are employed for interface cracks.

The local stress and displacement fields (of an interface crack between two orthotropic materials) are derived in [35] for a state of plane stress or plane strain. These fields are defined by a complex stress intensity factor K and a real stress intensity factor K_3. The displacement and stress fields are defined in the xz-plane along the direction defined by $\theta = 0$ (see fig. 2.2):

$$\sqrt{\frac{H_{11}}{H_{22}}}\delta_x + i\delta_z = \frac{2H_{11}K|r|^{\frac{1}{2}+i\epsilon}}{\sqrt{2\pi}(1+2i\epsilon)\cosh(\pi\epsilon)} \tag{2.10}$$

$$\sqrt{\frac{H_{22}}{H_{11}}}\sigma_{xx} + i\sigma_{xz} = \frac{K|r|^{i\epsilon}}{\sqrt{2\pi r}} \tag{2.11}$$

where δ_x and δ_z are the displacements in the x and z directions of the points lying on the crack flanks for $\theta = \pm\pi$ (see fig. 2.2). Instead, the stresses σ_{xx} and σ_{xz} are defined as the stresses present along the interface along the direction $\theta = 0$. The anti-plane stress and displacements fields are characterized by a real stress intensity factor as following along the direction $\theta = 0$ for σ_{xy} and $\theta = \pm\pi$ for δ_y:

$$\sigma_{xy}(r) = \frac{K_3}{\sqrt{2\pi r}} \tag{2.12}$$

$$\delta_y(r) = \sqrt{\frac{2r}{\pi}}(B_1 + B_2)K_3 \tag{2.13}$$

where subscripts 1 and 2 refer to the two different materials that join at the interface. The bi-material constants H_{11} and H_{22} are defined in [35]:

$$H_{11} = (2n\lambda^{\frac{1}{4}}\sqrt{S_{11}S_{22}})_1 + (2n\lambda^{\frac{1}{4}}\sqrt{S_{11}S_{22}})_2 \tag{2.14a}$$

$$H_{22} = (2n\lambda^{-\frac{1}{4}}\sqrt{S_{11}S_{22}})_1 + (2n\lambda^{-\frac{1}{4}}\sqrt{S_{11}S_{22}})_2 \tag{2.14b}$$

where S_{ij} are the material compliances introduced in [35]. S_{ij} are computed differently if the problem is treated as plane stress or plane strain. B_1 and B_2 are defined as:

$$B_1 = \left(\sqrt{S_{44}S_{55} - S_{45}^2} \right)_1 \tag{2.15a}$$

$$B_2 = \left(\sqrt{S_{44}S_{55} - S_{45}^2} \right)_2. \tag{2.15b}$$

The parameters λ and n are defined in [35] as:

$$\lambda = \frac{S_{11}}{S_{22}} \tag{2.16a}$$

$$n = \sqrt{0.5(1 + \rho)} \quad where \quad \rho = \frac{2S_{12} + S_{66}}{2\sqrt{S_{11}S_{22}}}. \tag{2.16b}$$

The oscillatory index ϵ is given by:

$$\epsilon = \frac{1}{2\pi} \ln \left(\frac{1 - \beta}{1 + \beta} \right) \tag{2.17}$$

where β is the Dundurs [37] bi-material parameter defined in [35] as:

$$\beta = \frac{[\sqrt{S_{11}S_{22}} + S_{12}]_2 - [\sqrt{S_{11}S_{22}} - S_{12}]_1}{\sqrt{H_{11}H_{22}}}. \tag{2.18}$$

Figure 2.2. Interface crack-tip geometry in sandwich composite.

K is a complex stress intensity factor that can be written as $K = K_1 + iK_2$. For bi-material interfaces with $\epsilon = 0$, K_1 and K_2 assume the same meaning of K_I and K_{II} stress intensity factors for cracks in homogeneous media. The mode-I and mode-II energy relase rate terms exists and they can be summed to give the total energy release rate as $G = G_I + G_{II} + G_{III}$. Moreover, it can be written that $K = K_I + iK_{II} = Ke^{i\psi}$ where ψ is defined as in eq. 2.20.

On the other hand, the presence of the oscillatory index ($\epsilon \neq 0$) implies that the ratio of normal and in-plane shear stress components $\sigma_{xz}/\sigma_{xx} = \Im(Kx^{i\epsilon})/\Re(Kx^{i\epsilon})$ depends on the coordinate z along the $\theta = 0$ direction. As a consequence, the energy release rate for

the single in-plane modes G_I and G_{II} cannot be defined. G is given in function of the stress intensity factors K and K_3 by:

$$G = \frac{H_{11}|K|^2}{4\cosh^2(\pi\epsilon)} + \frac{1}{4}(B_1 + B_2)K_3^2. \tag{2.19}$$

The mode-mixity ψ can be defined for an interface crack as:

$$\psi = \arctan\left(\frac{\Im(Kr^{i\epsilon})}{\Re(Kr^{i\epsilon})}\right). \tag{2.20}$$

It is clear from eq. (2.20) that ψ is not uniquely defined because it depends on the distance r along the $\theta = 0$ direction. In order to define a unique value of ψ is useful to select a certain distance h in order to have a constant value of ψ that can be employed as reference in a analysis. Usually, h is set equal to the facesheet thickness of the composite sandwich as in [38], but it can be chosen arbitrarily. The mode-mixity ψ evaluated at $r = h$ is the following:

$$\hat{\psi} = \arctan\left(\frac{\Im(Kh^{i\epsilon})}{\Re(Kh^{i\epsilon})}\right). \tag{2.21}$$

The energy release rate can be expressed as functions of the local displacement field behind the crack tip. The substitution of eqs. (2.10) and (2.13) into eq. (2.19) and (2.20) gives:

$$G = \frac{\pi(1 + 4\epsilon^2)}{8H_{11}|r|}\left(\frac{H_{11}}{H_{22}}\delta_x^2 + \delta_z^2\right) + \frac{\pi\delta_y^2}{8|r|(B_1 + B_2)}. \tag{2.22}$$

$$\psi = \arctan\left(\sqrt{\frac{H_{22}}{H_{11}}}\frac{\delta_z}{\delta_x}\right) - \epsilon\ln\left(\frac{|r|}{h}\right) + \arctan(2\epsilon) \tag{2.23}$$

As suggested in [35], a fracture criterion for interface cracks in bi-material systems can be defined as:

$$G = G_c(\hat{\psi}, \phi) \tag{2.24}$$

where G is the energy release rate defined in eq. (2.19), G_c is the fracture toughness of the interface, $\hat{\psi}$ is the mode-mixity defined in eq. (2.20) and ϕ is an additional phase angle in the stress intensity factor space (see fig. 2.3) as [39]:

$$\phi = \arccos\left(\frac{K_3}{\sqrt{|K|^2 + K_3^2}}\right) \tag{2.25}$$

remembering that $|K| = |Kh^{i\epsilon}|$. Hence, the interfacial toughness G_c depends in general on the two phase angles $\hat{\psi}$ and ϕ in the space defined by the orthogonal axis in fig. 2.3. A toughness surface is needed in order to fully characterize the fracture resistance of a surface.
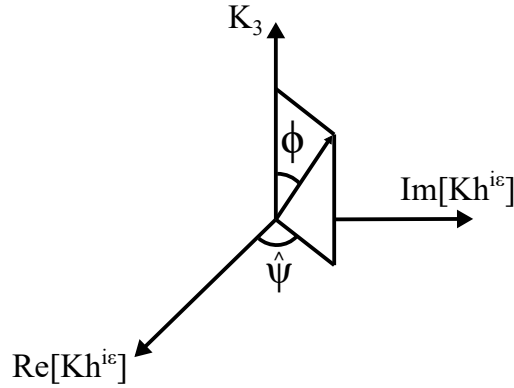
Figure 2.3. Phases space for interface cracks.

2.3 CSDE Method

It is possible to obtain the energy release rate if the displacement field behind the crack tip is known eq. (2.22). A FE model of a debonded composite sandwich, subjected to external loads, can be build and solved. The FE solution is capable to provide the local displacement field behind the crack tip with good accuracy, if a fine structured mesh is used in the numerical model. The numerical solution gives δ_x, δ_y and δ_z for each node lying on the crack flanks behind the crack tip (see fig. 2.2). Then, δ_x, δ_y and δ_z can be substituted in eqs. (2.22, 2.23 and 2.25) to compute G, ψ and ϕ.

The stress field associated with the in-plane crack opening modes (I-II) shows an oscillatory character due to the presence of the oscillatory index ϵ. Instead, the stress field related to the out-of-plane sliding mode (mode III) does not present any oscillatory feature and it is not coupled with the in-plane stress field as found in [35]. Therefore, it is possible to compute separately the mode III component G_{III} (second term on the right-hand side of eq. 2.22). Then, it possible to find G_{I-II} (first term on the right-hand side of eq. 2.22). A numerical method that uses the local displacement field behind the crack tip is the Crack Surface Displacement (CSD) method developed in [40–42]. The main issue is the presence of a zone, close to the crack tip, where the stress and displacement fields oscillate due to the presence of the index ϵ. In fact, the numerical error can be consistent in this oscillation region and the assessment of the stress intensity factors become inaccurate. A numerical method which circumvents the oscillation zone in computing G and the phase angles is developed in [43]. This method is called Crack Surface Extrapolation (CSDE). The CSDE method extracts the displacement jumps between the nodes lying on the crack flanks in the K-dominant zone (see fig. 2.4). Then, the CSDE extracts the jumps δ_x, δ_y and δ_z for each nodal pair and it calculates G using equation 2.21. Thus, the trend of the energy release rate can be plotted against the z-coordinate along the $\theta = 0$ direction. Finally, the method fits with a straight line the values of G vs. z and it extrapolates the value of the energy release rate to the crack tip. The extrapolation allows to shoot-over the oscillation zone, avoiding any possible numerical error coming from the strong oscillations provided by the displacement field. The CSDE method is implemented in the commercial FE software Abaqus® as a Python script.
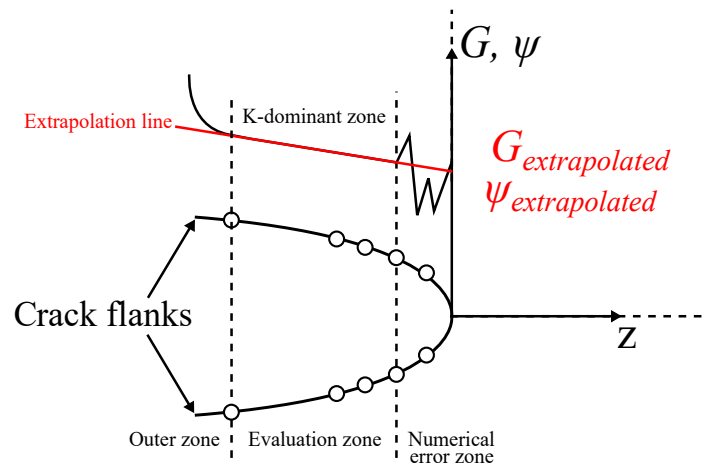
Figure 2.4. Schematic illustration of the CSDE method.

3. MIXED MODE FRACTURE OF CRACKS

An introduction to the mixed-mode fracture problem for cracks in metals and interface cracks between dissimilar orthotropic media is presented. This chapter provides a summary of the literature available regarding mixed-mode fracture characterization testing in metals and explains the difficulties of obtaining a dominant and homogeneous mode-III stress field along the crack front in a beam-like specimen that has traction free-edges. The intrinsic 3D nature of the problem is briefly presented. Afterwards, an additional literature review is presented about the more matured and used test rigs that perform out-of-plane fracture characterization tests for monolithic composite laminates. The chapter is concluded showing which test rig, among the others, has inspired the novel test fixture that will be presented in chapter 3. Different parts of the text and pictures are taken and adapted from [P1] and [P2]. All the text parts taken from [P1] and [P2] are reported in quotes "...".

3.1 Pure Anti-plane mode in Fracture Mechanics

Chapter one explains what is the definition of mode-III crack opening mode. This opening mode is characterized by the presence of an anti-plane shear stress field at the crack front. As it is depicted in fig. 3.1, an anti-plane field is characterized only by out-of-plane displacements along the z-direction. All the in-plane displacements are equal to zero.
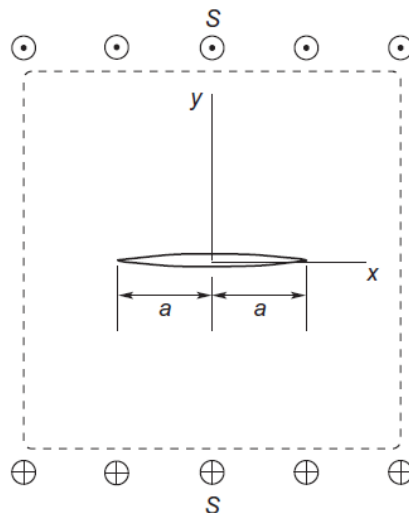
Figure 3.1. Crack in an infinite plate subjected to anti-plane shear, picture courtesy from [44].

Paragraph taken and adapted from [P1]. "An anti-plane stress/displacement field is the third kind of elastic problem that is usually solved in linear elasticity along with

plane-stress and plane-strain configurations. A closed form solution of an anti-plane stress/displacement local field is provided by Suo in [35] for and interface crack between two dissimilar anisotropic media. Likewise plane strain and plane stress states, the anti-plane state requires that the local stress/displacement field repeats itself in a self-similar manner on all the planes orthogonal to the z-direction (see fig. 3.1). Hence, it is necessary the presence of a continuous crack front in order to satisfy the pure anti-plane conditions. Traction-free edges, present on every beam-like specimen for fracture characterization, are a feature that breaks the continuity of the crack front. In fact, the stress/displacement field has to change abruptly to satisfy the traction-free boundary conditions. This zone of transition can be considered as a boundary layer. The characteristics of this boundary layer are studied in analytical and numerical studies by Benthem, Dhondt, Sih and Fenner [45–48]. The singularity of the stress field changes when a traction-free edge is approached as studied analytically in [45] and numerically by Nakamura in [49, 50]. The equations found by Suo in [35] does not describe the local stress/displacement fields present in the aforementioned boundary layer, where neither plane strain nor plane stress nor anti-plane field exist. Therefore, the analytical closed-form solutions presented in [35] cannot be used at the specimen free-edges."

   Paragraph taken and adapted from [P1]. "Additional complexity is added to the problem by the fact that mode-II and mode-III fields are coupled at the specimen free edges. Several studies [51–58] showed how, when a crack edge meets a traction-free surface, a coupling is present between in-plane shear deformations and out-of-plane shear deformations. This phenomenon can be detected and is analysed in [51–58] using FE model as it can be seen in fig. 3.2.

Typical deformations for mode II
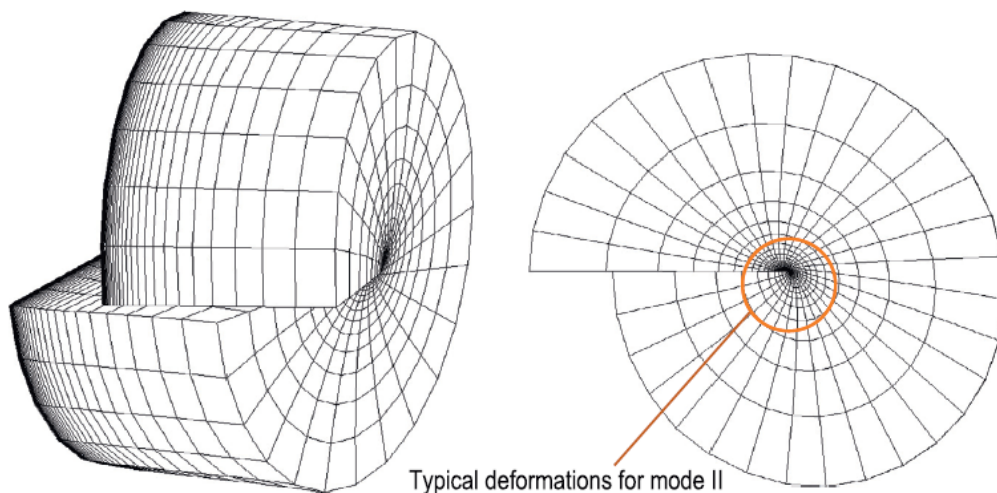
Figure 3.2. Coupling between in-plane shear and out-of-plane shear deformations at the crack front intersection with a traction-free edge. (Picture courtesy from [58])

The discontinuity of the crack front and its intersection with a traction-free surface leads to a 3D local stress field in the boundary layer. This fact implies that the local values of the energy release rate along the crack front are not constant. The energy release rate shows a peculiar local trend when the boundary layer in the vicinity of the traction-free edge is approached. These results have been presented in [54, 55], where a pure anti-plane stress field is applied on the boundary of a cracked disc (see fig. 3.2). The disc is made of

a linear elastic and homogeneous material. The local value of the out-of-plane stress τ_{yz} (fig. 3.1) decreases from the center of the disc to the traction-free edge. It becomes equal to zero at the free-edge to satisfy local equilibrium condition at the free surface. Instead, the local value of the in-plane shear stress τ_{yx} increase from zero to a finite value where the crack front meets the free edge in order to satisfy local equilibrium of stresses. Since the local stresses τ_{yz} and τ_{yx} are proportional to the correspondent stress intensity factors, and the energy release rate is proportional to the square of the stress intensity factors, then the local value of G is not constant along the crack front (see fig. 3.3).
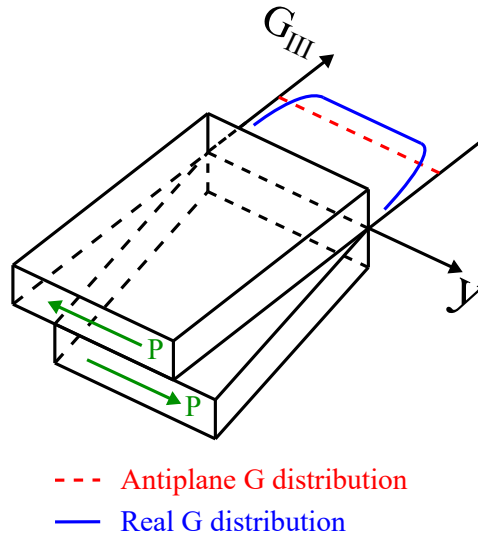
Figure 3.3. Qualitative representation of the local energy release rate values in a specimen that presents traction-free edges and subjected to out-of-plane loadings. Taken from [P1].

The phenomena described above are emphasized in the case of an interface crack where the elastic mismatch intensifies the coupling between in-plane and out-of-plane shear stresses, respect to the case of a crack in a homogeneous material. Hence, it is not possible to have an homogeneous distribution of the energy release rate in a cracked bi-material beam-like specimen subjected to out-of-plane shear loadings. Moreover, the stress state in the boundary layer in the vicinity of the traction-free edge is always mixed-mode II-III. If the crack starts its propagation in the region close to the traction free edges, the fracture toughness related to that propagation corresponds always to a certain mode-mixity between mode-II and mode-III, even if the macroscopic external loading consists in pure out-of-plane shear forces."

The next section presents and compares the existing test rigs presented in the literature for mode-III fracture characterization. All of them show the problem of obtaining a homogeneous distribution of the energy release rate without having a coupling between mode-II and mode-III close to the specimen traction-free edges.

3.2 Literature review of Mode-III fracture characterization test rigs

It is relevant to go through the literature regarding mixed-mode fracture propagation in metals, before jumping to the fracture experimental tests available for composite materials. Several experimental tests for fracture characterization under mixed I-III and II-III mode have been developed for metallic materials. A comprehensive review of these tests is given

in [59]. Mixed mode I-III tests are covered by a modified compact tension specimen with a slanted notch and a compact tilted-tension specimen with a straight pre-crack presented in [60]. The fixture presented in [60] is able to cover all the mode-mixities between pure mode I and pure mode III. Mixed modes II-III are explored by the test apparatus presented in [61] that consists in a pre-cracked beam subjexted to bending loads. All mode mixities between mode II and mode III can be explored changing the tilting angle on the mentioned pre-cracked beam. For mixed mode I-II-III stress states, there are mainly three fracture test configurations: the compact tension-shear-rotation test (CTSR) [62], all fracture mode test (AFM) [63] and the compact tension-shear-torsion test (CTST) [64]. All these three test fixtures present two main issues: the CTSR test rig has low level capacity making it not suitable for fracture characterization of metals (such as steel and titanium) and all the test fixtures showed some difficulties in monitoring of crack growth extension and paths. More studies and research are necessary in order to investigate deeply the field of mixed-mode fracture of metals. In fact, a standardised fracture characterization test for metals subjected to the most general case (mixed mode I-II-III) does not exist up to now. Composite materials exhibit different and additional problems when it comes to fracture characterization testing under mixed mode conditions. A summary of the more matured test rigs for fracture characterization under pure mode III loads is presented in the next paragraph.

Paragraph taken and adapted from [P1] and [P2]. "Different experimental methods exist to measure the value of the interface fracture toughness G_c under out-of-plane shear stress conditions in monolithic laminates. These include: the edge crack torsion test (ECT) [23], the modified split cantilever beam (MSCB) test [24] and the shear torsion bending (STB) [25] test, see fig. 3.4. The ECT test consists of a delaminated plate subjected to a twisting moment which results in a distribution of out-of-plane shear stresses along the debonded front. Instead, the MSCB test includes cracked specimen with a beam-like geometry. In this test, two transverse forces are applied on the delaminated arms in order to produce out-of-plane stresses along the crack front. The issue with ECT and MSCB tests is the lack of local uniformity in the stress field along the crack front. This non-uniformity of the local stress field at the crack tip is caused by the presence of the load-free lateral edges of the specimen. The load-free lateral edges cause the out-of-plane shear stresses to change abruptly from the central part of the crack front to the crack edges where they should go to zero for the static equilibrium. This phenomenon is causing the presence of undesired mode-II stress components in a zone where the crack front is intersecting the lateral specimen free-edges as observed in [26]. Hence, the fracture toughness measured using these specimens is associated with a certain mode-mixity between mode II and III. Similarly to the MSCB test, the STB test [25] includes a pre-delaminated specimen with a beam-like geometry. In this case, the specimen is loaded using two stiff load blocks attached at the end of the two delaminated arms, which can slide preventing rotations of the arms. These loading conditions, along with two longitudinal side notches (in the intact part of the specimen) favor a uniform distribution of out-of-plane shear stresses along the crack front and therefore more uniform mode III conditions at the crack front compared with the ECT and MSCB tests. Therefore, the STB test [25] is chosen as the reference test in order to develop the new data reduction method presented in this work. The STB test rig is also capable to apply mode-I and mode-II loads, but only the mode-III configuration is analysed here.

(a) ECT specimen.

(b) MSCB specimen.
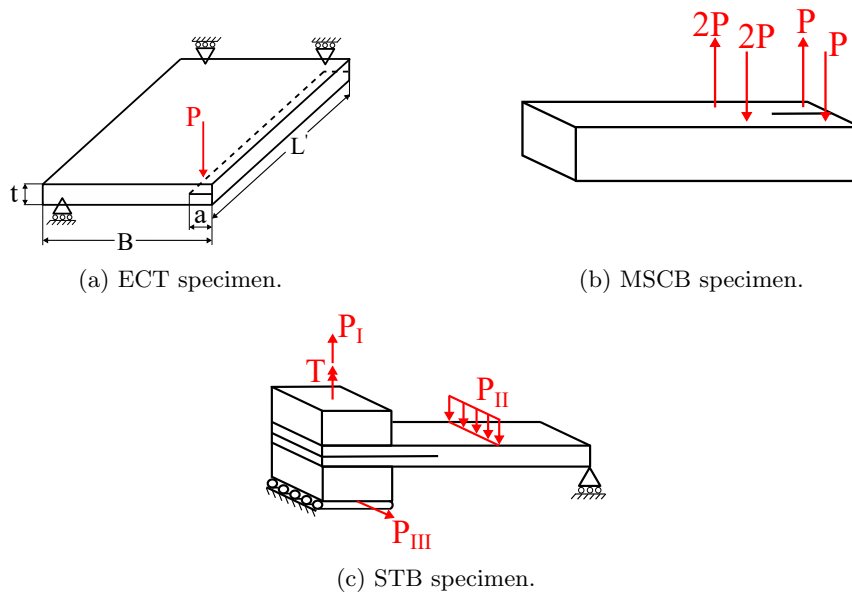
(c) STB specimen.

Figure 3.4. Test rigs designed to perform fracture characterization tests under out-of-plane shear loadings. Taken from [P1].

Although, all beam-like specimens (including the STB) show characteristic features during crack propagation under out-of-plane shear. Experiments reported in the literature [65–67] show a large scatter in fracture toughness measurements because of the change in the the coupled mode II/III stress field when the crack advances. Furthermore, recent studies on carbon fiber unidirectional laminates [65–67] show that the delamination crack advance is preceded by the formation of intra-laminar cracks. These intra-laminar cracks grow out of the main delamination plane in the matrix. The propagation of intra-laminar cracks is controlled by the fiber orientation in the laminae adjacent to the delamination and the presence of this energy dissipating mechanism is responsible for an R-curve behaviour and the apparent fracture toughness measured in the tests performed in [65–67]." The data reduction method presented in [25] is applicable only to monolithic laminates, does not take into account the intra-laminar cracks and has been derived for a specific specimen geometry and crack length. The equation in [25] presents some global coefficients, which are calibrated numerically. These coefficients globally account for effects related to crack root-tip rotations, shear deformations and stress decay in the intact and traction-free part of the specimen.

In the next chapter, a novel test rig along with a data reduction method developed in [68] for sandwich fracture characterization is presented. The test fixture is inspired by the STB test rig for monolithic composites already developed by Davidson et al. in [25]. The novelties introduced in this PhD thesis (respect to the work done in the cited literature and in [25] are the following:

1. Build an equation that expresses the mode-III energy release rate in function of the external loads applied to the specimen, using only linear elastic fracture mechanics theory and without the need of defining coefficients that are extracted from a numerical model (as it is done in [25]). This analytical derivation has been possible in the case related to the monolithic laminate specimen. The expression of the energy

release rate for the sandwich composite specimen needs only two constants that are numerically defined.

2. Build a novel test rig that is capable to perform mode-III fracture characterization tests of composite sandwich specimens having PVC foam cores. The novel test rig is inspired to the test fixture presented in [25] which is able to perform experimental tests uniquely on monolithic laminates.

4. DATA REDUCTION METHOD FOR MODE III FRACTURE CHARACTERIZATION

The data reduction method for fracture characterization of sandwich and monolithic laminate specimens subjected to out-of-plane shear loads is first presented in this chapter. Secondly, the schematics of the test fixture and experimental results, derived from a first pilot testing campaign, are shown both for monolithic laminates and composite sandwich specimens. The text and pictures regarding the semi-analytical data reduction method are taken and adapted from [P1] and [P2]. All the text parts taken and adapted from [P1] and [P2] are reported in quotes "...".

4.1 Data reduction method for energy release rate extraction

Paragraph taken and and adapted from [P1]. "The new data reduction method presented in this work is inspired to the work in [24] and responds to the need for reducing measured force and moment data to energy release rate using a novel test rig presented in [68] (inspired to STB [25]). The analytical model presented in this work uses linear elastic fracture mechanics and assumes that the delamination crack propagates along its original plane and that no other damage mechanisms are present in the specimen. Thus, the possible presence of intra-laminar cracks is not taken into account by the current model. The assumptions will require experimental validation. In the novel test rig, an out-of-plane shear load is applied to a pre-debonded sandwich specimen in order to propagate the debond, as shown in fig. 4.1. An expression of the energy release rate that takes into account the geometry, the specimen material system and the load set applied is required to size correctly the specimen and to compute the fracture toughness G_c from experimental results. A closed-form derivation of the energy release rate for a sandwich specimen is presented. Then, the solution for composite sandwich is particularized for a monolithic laminate."

Paragraph taken and and adapted from [P1]. "The specimen with its load tabs is presented with the main geometrical parameters in fig. 4.1. Two different specimen widths are considered as it is shown in fig. 4.1: b is the width of the delaminated part of the specimen and W is the width of the intact interface ahead of the crack front, where two longitudinal cuts have been introduced. W is the geometrical parameter, which defines the fracture surface where the crack propagates. The presence of two different widths is due to the introduction of two longitudinal cuts (see fig. 4.1) that mitigate the free edge effects described in chapter 3. The introduction of these longitudinal cuts is a technique already adopted in [25] for monolithic laminates.
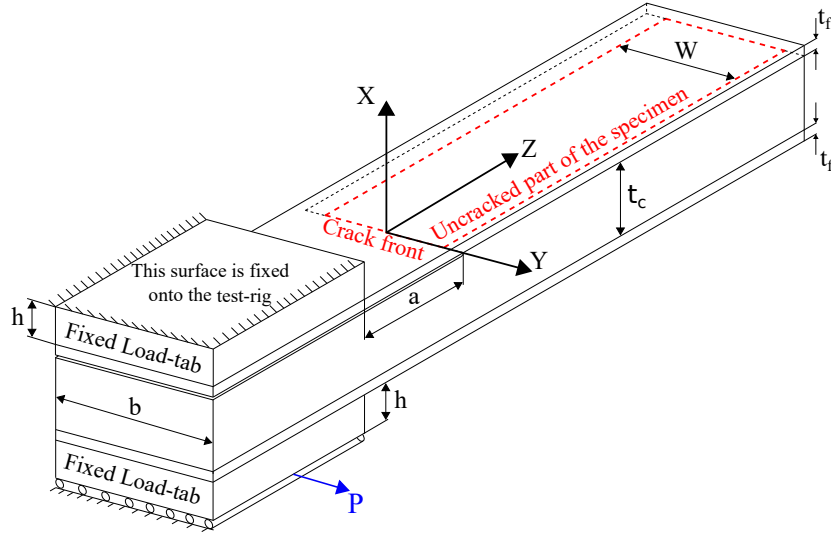
Figure 4.1. Representation of the specimen with its geometrical parameters and the applied load
P. Taken from [P1].

The two face sheets have the same thickness t_f and the core thickness is t_c. The crack
length a is the distance between the end of the load tab and the crack tip. h is the height
of each load-tab. The geometrical values considered in this work are summarized in tab.
4.1.

	t_f	t_c	a	b	W	L	L_{tab}	h
Laminate	2	-	40	30	26	160	60	10
Sandwich	2	20	40	40	24	160	60	10

Table 4.1. Main geometrical parameters, all lenghts are expressed in mm. Taken from [P1].

Moreover, the index d is used to indicate the upper delaminated face sheet and the index
s is utilized to denote all the parameters related to the lower substrate (made of the core
and lower face sheet)."

Paragraph taken and and adapted from [P1] and [P2]. "Two types of specimens are
studied: a glass fiber monolithic laminate and a foam-cored sandwich. The laminate
and face sheets of the sandwich specimen are modelled as linear elastic, homogeneous
and orthotropic materials whose equivalent elastic properties are reported in tab. 4.2.
The core is modelled as linear elastic, homogeneous and orthotropic material. The case
studied uses the properties in tab. 4.3 that are representative of a PVC foam considered
as isotropic. The upper delaminated arm consists of a beam having a homogeneous cross-
section, and the lower arm has an in-homogeneous cross-section composed of two different
materials: the core and the face sheet. The $X - Y - Z$ axes are coincident with the
principal material directions (3, 1, 2) for both face sheets and core (see fig. 4.2). Each
XY-plane is a plane of elastic symmetry, so that torsional moments (acting along the
Z-axis) are not coupled with bending moments acting along X-Y axes. Consequently,
orthotropic face sheets that comply with the aforementioned requirements can be either
unidirectional or cross-ply (see [69]). The properties in tabs. 4.2-4.3 describe a quasi-
isotropic (in its plane) monolithic laminate and sandwich face-sheets having a lay-up of
reinforced glass fiber cloths infused with epoxy resin. Instead, the core consists in a open-
cell PVC foam core of class H100 manufactured by Diab®. The laminate considered has

the following lay-up $[(0/45/90/-45)_4||(0/45/90/-45)_4]$, where the symbol $||$ designates the location of the teflon insert. Instead, the lay-up sequence of each sandwich face-sheet is $[(0/45/90/-45)_4]$. Thus, the delaminated arms of the monolithic laminate and the face-sheets of the sandwich specimen are balanced but not symmetric laminates. The twist-bending coupling terms are non-zero for a lamina having a $(0/45/90/-45)_n$ lay-up. Nevertheless, the twist-bending coupling terms of the ABD matrix (D_{16} and D_{26}) become quite small when the number of plies is ≥ 16."
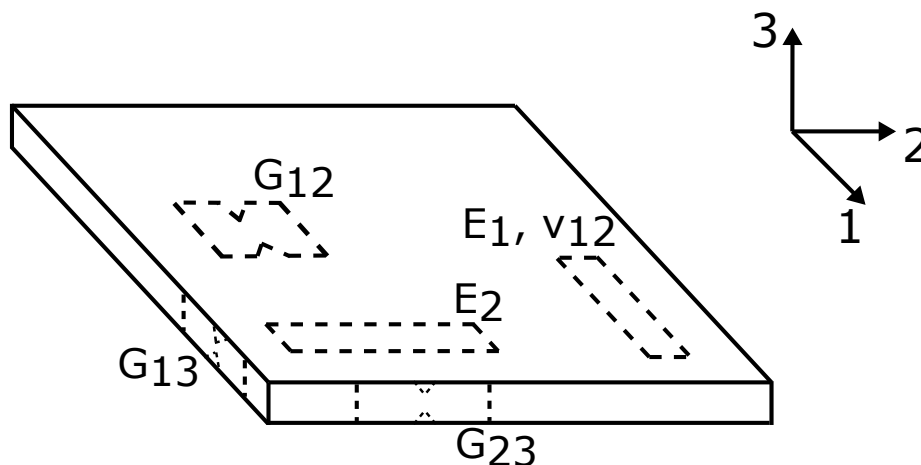
Figure 4.2. Illustration of the plate laminate and specimens that are cut out for material testing. The principal material directions (3, 1, 2) coincides with the (X,Y,Z axes).

Paragraph taken and adapted from [P1] and [P2]. "Two laminate plates were manufactured in order to measure the material properties reported in tab. 4.2. A 3 mm thick laminate was manufactured in order to produce specimens for measuring in-plane elastic properties such as E_{ZZ}, E_{YY}, ν_{YZ} and G_{YZ}. Instead, a thicker plate was manufactured in order to meausure the out-of-plane elastic moduli E_{XX}, ν_{XY}, ν_{XZ}, G_{XZ} and G_{XY}. Five specimens were tested in order to measure the value of each elastic modulus and a total of 35 specimens were tested. The material properties of the laminate and sandwich face sheets are measured from mechanical tests following ASTM standards [70–72]. Tensile tests to measure E_{ZZ}, E_{YY} and ν_{YZ} were conducted according to [70]. A sketch of how the specimens were cut out from the two aforementioned laminate plates is reported in fig. 4.2. The longitudinal and transverse strains in the specimens for the the characterization of tensile properties [70] (see fig. 4.3) were measured using DIC technique. A speckle pattern was prepared on each specimen and two virtual extensometers were set in order to measure the longitudinal strain ϵ_{11} and the transverse strain ϵ_{22}."

Paragraph taken and adapted from [P2]. "The V-Notched Rail Shear Method [71] was employed to measure the in-plane elastic shear modulus G_{YZ}. Similarly to the characterization of the in-plane tensile properties, two virtual extensometers (through the use of DIC) were set to measure the strains in the principle directions $\epsilon_{45°}$ as shown in fig. 4.4. Instead, the elastic shear moduli G_{XZ} are evaluated using Iosipescu shear test [72]. The value that refers to G_{XY} is set equal to G_{XZ} because of the fiber orienation in the laminate lay-up."

Paragraph taken and adapted from [P2]. "No ASTM standards are available for measurement of E_{XX}, ν_{XY} and ν_{XZ} for a FRP laminate. Nevertheless, a test method suggested in [73] was adopted to measure E_{XX}, ν_{XY} and ν_{XZ}. Test specimen having dimensions of
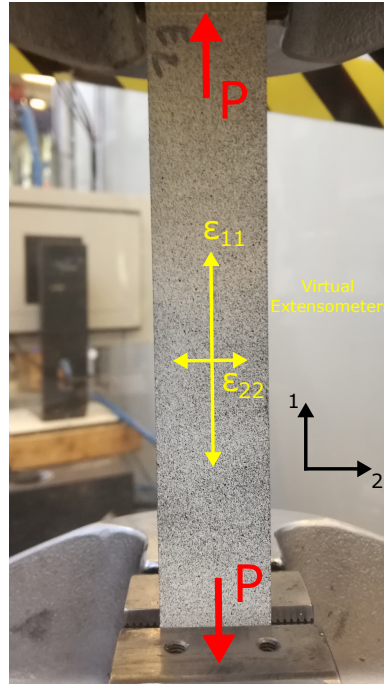
Figure 4.3. Tensile material characterization test for measuring in-plane elastic moduli E_{ZZ}, E_{YY} and ν_{YZ} of the monolithic laminate.

19x19x19 mm were inserted between two compressive platens. Digital image correlation (DIC) Aramis® system was used to monitor the strains on the specimen sides. Values for ν_{XY} and ν_{XZ} should correspond to the same number since the lay-up of the laminate. The difference between ν_{XY} and ν_{XZ} (in table 4.2) could result from inaccuracies in the measurement of the transverse strains on the 19x19x19 mm material block. Material properties for the PVC foam core were taken from the manufacturer catalogue [74] and the load tabs are made of C40 structural steel."

	E_{YY}	E_{ZZ}	G_{XY}	G_{XZ}	G_{YZ}	ν_{XY}	ν_{XZ}	ν_{YZ}
Elastic moduli (average) [GPa]	19.8	19.8	2.9	2.9	7.5	0.43	0.37	0.32
Nr. Specimens	5	5	5	5	-	5	5	5
CV [%]	3.3	5.0	7.8	7.8	1.7	13.5	10.1	1.3

Table 4.2. Laminate material properties measured experimentally with their coefficient of variation, see fig. 4.1 for axes directions. X direction is through the laminate thickness, instead Y and Z are in the laminate plane. Taken from [P2].

Material	Elastic Moduli [GPa]						Poisson ratios		
	E_{XX}	E_{YY}	E_{ZZ}	G_{XY}	G_{XZ}	G_{YZ}	ν_{XY}	ν_{XZ}	ν_{YZ}
Core H80	0.095	0.095	0.095	0.035	0.035	0.035	0.4	0.4	0.4
Core H45	0.055	0.055	0.055	0.015	0.015	0.015	0.4	0.4	0.4
Load-Tabs	200	200	200	77	77	77	0.3	0.3	0.3

Table 4.3. Core and load tab material properties. Taken from [P2].

Paragraph taken and adapted from [P1] "The following notation is used in all the following equations: E_f and E_c denote the longitudinal elastic moduli E_{ZZ} of the face
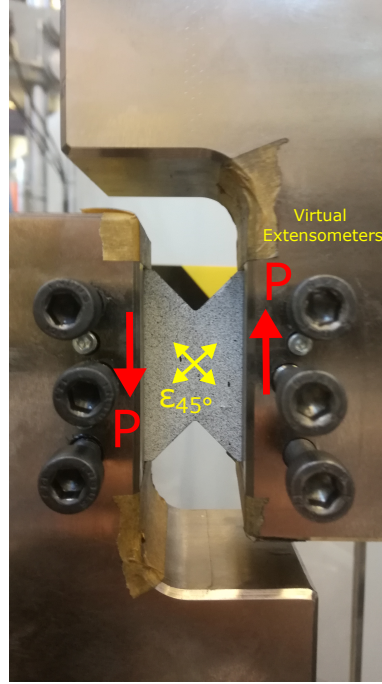
Figure 4.4. Shear material characterization test for measuring the in-plane shear modulus G_{YZ} of the monolithic laminate.

sheets and core, while G_f and G_c refer to the elastic shear moduli of face and core in the YZ-plane. Fig. 4.5 shows loads and reaction forces on the load tabs and loads transferred to each debonded arm of the sandwich composite. The lower-tab surface can only translate in the Y-direction, while points on the upper-tab surface are fixed. The load tabs prevent rotations and torsional warping of the arm cross section located at $Z = -a$. The intact part of the specimen is traction free and it follows rigidly the displacements/rotations of the debonded arms. The only external load is the load P and it is applied on the lower load tab. A reaction force P^R arises in the upper load-tab, parallel to the Y-axis, which is equal and opposite to P in order to satisfy equilibrium. Two different reaction moments M_Z^{Rd} and M_Z^{Rs} set in parallel with the Z-axis on the surface of each load tab, since rotations around the Z-axis are not permitted. Moreover, reaction moments around the X-axis (M_X^R) arise on each load tab, since rotations of the specimen around the X-axis are locked."

Paragraph taken and adapted from [P1] "The loads are transferred from the load tabs to each cross-section shear center in the specimen. As shown in fig. 4.5 (b), the loads consist of two out-of-plane shear forces $V_Y = P$ equal and opposite in each debonded arm, two moments M_Z^d and M_Z^s acting on the upper and lower delaminated arms at $Z = -a$ and a moment $M_X(Z = -a)$ acting on both debonded arms. Where the two delaminated arms join, at the crack front (see fig. 4.6), internal moments and forces must constitute an auto-equilibrated system since the intact part of the specimen is traction-free. The value of the two internal moments $M_X(Z = 0)$ have opposite directions and same magnitude. The two shear forces $V_Y = P$ generate a resultant moment in the Z-direction which equilibrate the sum of the two moments $M_Z^d(Z = 0) + M_Z^s(Z = 0)$."

Paragraph taken and adapted from [P1] " The shear center of the upper debonded
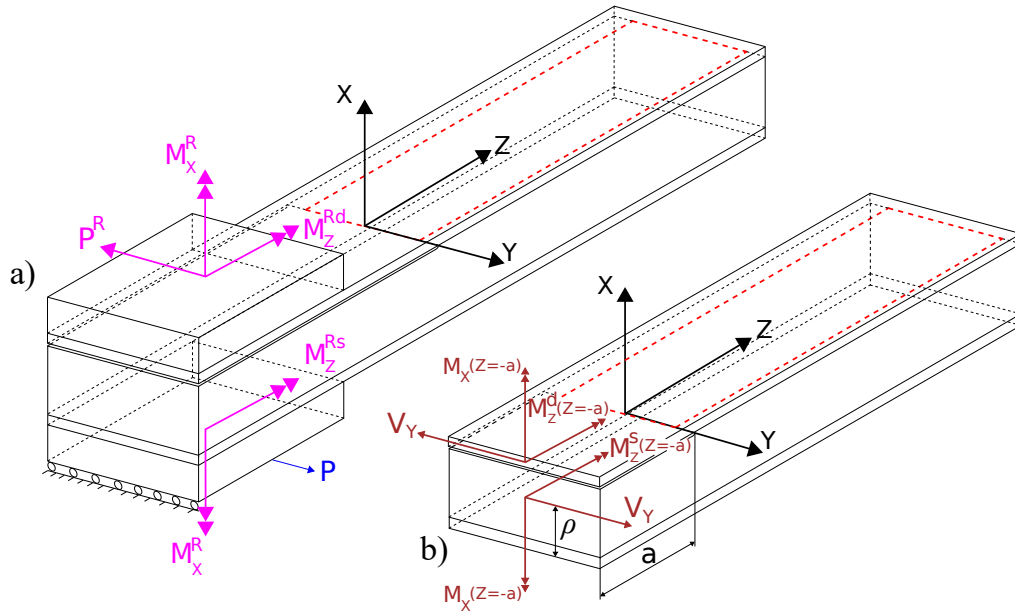
Figure 4.5. (a) Specimen with load tabs and reaction loads, (b) loads acting at the shear center of each debonded arm. Taken from [P1].

arm is the geometrical centroid of the face sheet cross section. The lower debonded arm presents a rectangular cross-section composed by two materials having different elastic properties. Classical laminate theory (CLT) is used to find the shear center position (see fig. 4.7) for the lower debonded arm:"

$$\rho = \frac{t_f + t_c}{2} - \frac{t_c t_f (G_f - G_c)}{2(G_c t_c + G_f t_f)}. \tag{4.1}$$
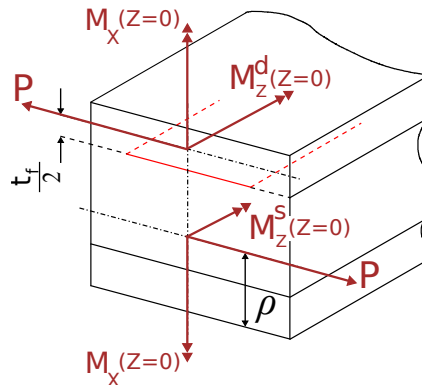
Figure 4.6. Close view of the auto-equilibrated internal force set at crack front ($Z = 0$), where the two debonded arms join. Taken from [P1].
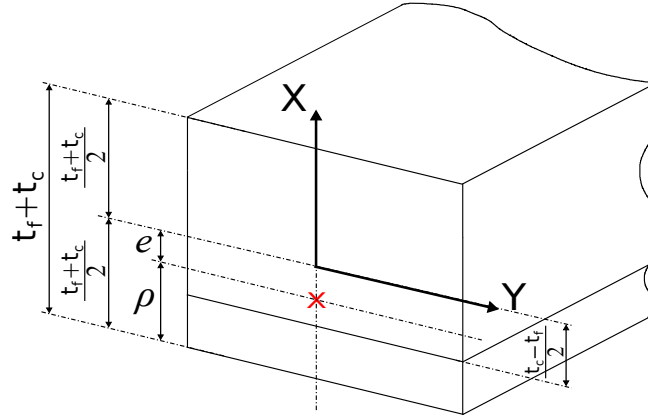
✕ Bi-material beam shear center

Figure 4.7. Scheme used to find the shear center of the bi-material cross-section. Taken from [P1].

4.1.1 Energy release equation for the sandwich configuration

Paragraph taken and adapted from [P1] "The energy release rate, for the uniform propagation of the crack front, is calculated from the total potential energy Π of the system:

$$\Pi = U_{tot} - L_{ext} \tag{4.2}$$

where $U_{tot} = U_d + U_s$. The energy release rate is defined here as the variation of the total potential energy due to a unit crack area extension, which implies a uniform extension of the crack front:

$$G = -\frac{1}{W}\frac{d\Pi}{da} \tag{4.3}$$

where W is the specimen width linked to the cracked surface area (see fig. 4.1). As a result, a closed form expression for the energy release rate for a debonded sandwich specimen can be found as function of the applied load P:

$$\begin{cases} G_{SAN} = G_d + G_s \\ G_d = \frac{P^2}{2WG_fA_f\kappa_d} + \frac{P^2a^2}{8WE_fI_f}\frac{(ak_r^d + 2E_fI_f)^2}{(ak_r^d + E_fI_f)^2} + \frac{(M_z^d(z=a))^2}{2WD_d}\frac{(1-e^{2ac_d})^2}{(1+e^{2ac_d})^2} \\ G_s = \frac{P^2}{2W(GA)_s} + \frac{P^2a^2}{8W(EI)_s}\frac{(ak_r^s + 2(EI)_s)^2}{(ak_r^s + (EI)_s)^2} + \frac{(M_z^s(z=a))^2}{2WD_s}\frac{(1-e^{2ac_s})^2}{(1+e^{2ac_s})^2}. \end{cases} \tag{4.4}$$

All the geometrical and material parameters appearing in eq. 4.4 are introduced and defined in [P1]."

4.1.2 Energy release rate equation for the monolithic laminate configuration

Paragraph taken and adapted from [P1] "The energy release rate expression for a monolithic laminate can be derived following the same procedure described in the previous paragraph, in function of the load P:"

$$G_{LAM} = \frac{P^2}{WG_fA_f\kappa_d} + \frac{P^2a^2}{4WE_fI_f}\frac{(ak_r + 2E_fI_f)^2}{(ak_r + E_fI_f)^2} + \frac{(M_z(z=a))^2}{WD}\frac{(1-e^{2ac})^2}{(1+e^{2ac})^2}. \tag{4.5}$$

4.1.3   Numerical Model

Paragraphs taken and adapted from [P1]. "A high-fidelity 3D FE based fracture mechanical model is formulated in order to verify the accuracy of the analytical solution. The FE mesh is presented in fig. 4.8.

A global model and a submodel have been created. The global model represents the whole specimen with boundary conditions applied as in fig. 4.1. The submodel includes only a material region surrounding the crack tip. Accordingly, the global model has been run first utilizing the sub-modelling technique [75]. Then, the displacements found as results of the global model are applied to the sub-model on its boundaries.

The global model is employed in order to extract the numerical specimen compliance $C_{FE} = \Delta/P$, where Δ is the displacement corresponding to the applied load P. The variation of C_{FE} respect to a is used to calculate a global value for the energy release rate using the compliance method. Instead, the submodel is used to extract locally the energy release rate along the crack front. Both the global model and submodel are created and solved using the FE commercial software Abaqus® 2018. Brick elements are used with quadratic shape functions (element C3D20) for both the global model and submodel.
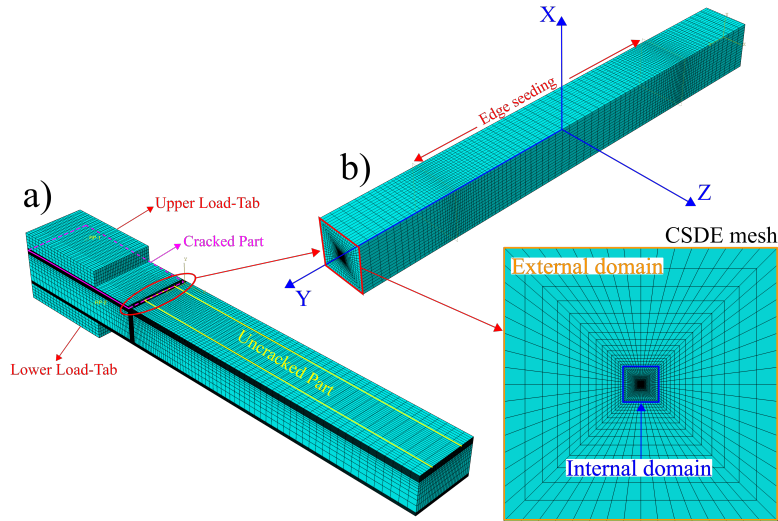
Figure 4.8. (a) FE global model and (b) submodel. Taken from [P1].

The compliance C_{FE} is extracted for different values of crack lengths. The energy release rate is thus defined through global structure parameters like P and C_{FE} as:

$$G_{FE} = \frac{P^2}{2W}\frac{\partial C_{FE}}{\partial a}. \tag{4.6}$$

The local distribution of the energy release rate along the crack front is also extracted and compared with G_{FE} and the analytical values G_{SAN} and G_{LAM}, eqs. (4.4, 4.5) . The method used to extract the local energy release rate is the Crack Surface Extrapolation (CSDE) method and it is presented in [76]. The CSDE method extracts the displacement jumps behind the crack front from the FE model (from the nodes lying on the crack flanks in the inner rig) and inserts them into the equations that relate the local displacement

field behind the crack front to the local stress intensity factors and energy release rate components [35].

Moreover, the FE model is used to perform parametric analyses to study the influence of the geometry on the local distribution of the energy release rate. The geometrical parameters, that have been investigated, are: the width b varying the ratio b/t_f and the crack length a varying the ratio a/t_f (fixing all the other geometrical parameters in both cases, see tab. 4.1)."

4.2 Results and Discussion

Paragraphs taken and adapted from [P1] "The aim of building the FE model is triple: in the first place, the FE analysis verifies if a true anti-plane stress state is achieved locally along the crack front, secondly the FE model is useful to check the percentage of mode-III component in the energy release rate distribution at the crack front and thirdly the numerical model is necessary to validate the assumptions made in the analytical model.

The steady-state (crack length independent) solution of the energy release rate for antiplane conditions is:

$$G_{antiplane} = \frac{\tau_{zy}^2 b t_f}{W G_f} \tag{4.7}$$

where $\tau_{zy} = P/bt_f$.

The results for the parametric study varying the ratio b/t_f for $a/t_f = 10$ are presented in the figure below (all the other geometrical parameter used can be found in tab. 4.1).
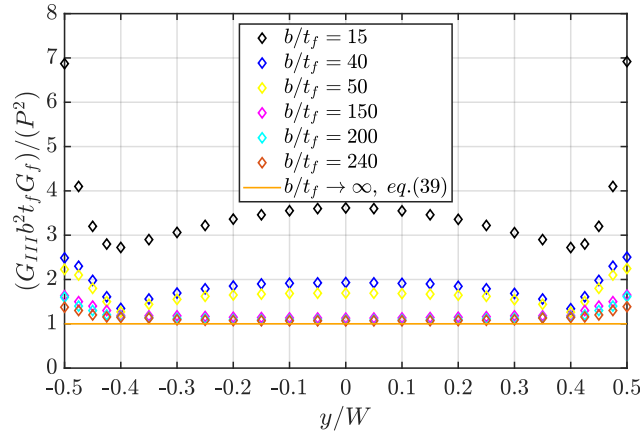
Figure 4.9. Local distribution of the mode-III component of the energy release rate along the crack front for different values of b/t_f and a fixed $a/t_f = 10$. Monolithic laminate. CSDE method. Taken from [P1].

The graph in fig. 4.9 reports the dimensionless mode-III component G_{III} of the energy release rate versus the dimensionless y-coordinate, that runs along the crack front. The local G_{III} distribution becomes progressively more constant on increasing b/t_f and approaches the limit anti-plane distribution for very large b/t_f, above 200. Since the width

b of the specimen cannot be very large because of the load capability limit of the test rig presented in [68], a value of $b/t_f = 15$ is used to show the results in the dedicated section.

The finite element analyses are used to define the geometries where the mode-III component of the energy release rate dominates over the other components. This is shown in figure 4.10a, where the variations of the ratio G_{III}/G_{Tot} are presented for $b/t_f = 15$. Here, G_{Tot} is the total value of the energy release rate at different locations on the crack front. The mode-III component of the energy release rate is always dominant in the central part of the crack front for all values of the crack length a/t_f. The mode-III component percentage decreases when a free edge is approached. When the crack length a/t_f increases, the edge effects intensify. As a matter of fact, the ratio G_{III}/G_{Tot} decreases substantially from $G_{III}/G_{Tot} = 0.9$ for $a/t_f = 15$ to $G_{III}/G_{Tot} = 0.47$ for $a/t_f = 35$. The geometry with $a/t_f = 15$ displays the widest portion of the crack front (from $y/W = 0.1$ to $y/W = 0.9$) that has a ratio $G_{III}/G_{Tot} \geq 0.9$. Fig. 4.10b illustrates the G_{III}/G_{Tot} variations for a sandwich composite specimen having $b/t_f = 20$. As expected the geometrical parameter b/t_f has a strong influence on the G_{III}/G_{Tot} distribution. The larger specimen width used for the sandwich, respect to the laminate case, promotes higher values of G_{III} for all crack lengths. The ratio G_{III}/G_{Tot} is as high as ≥ 0.8, at the crack corners, even for values of $a/t_f = 50$.
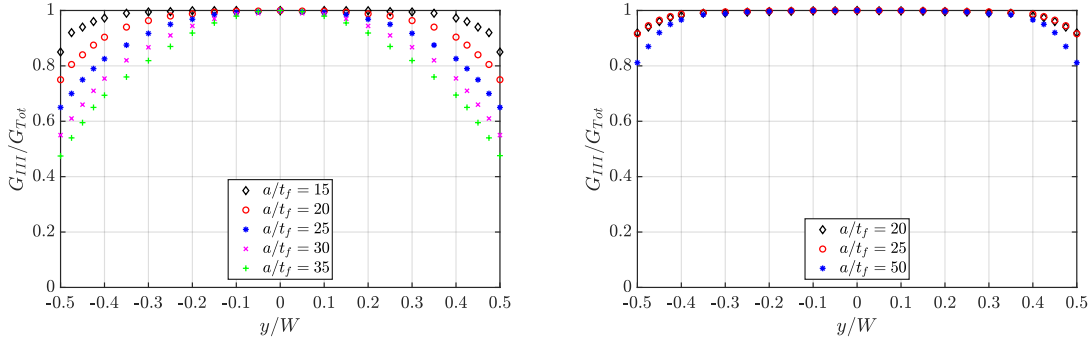
(a) Monolithic Laminate.   (b) Foam-cored Sandwich.

Figure 4.10. Percentage of the mode-III component of the local energy release rate, along the crack front for different values of a/t_f. $b/t_f = 15$ for the monolithic laminate and $b/t_f = 20$ for the sandwich specimen. Taken from [P1].

The analytical values of the energy release rate G_{SAN} and G_{LAM} (eqs. (4.4, 4.5)) are compared with the numerical values G_{FE} on varying the normalized crack length a/t_f in fig. 4.11 and using the parameters values reported in tab. 4.4. The relative difference between the analytical and the FE results is reported in tab. 4.5 for three crack lengths.

	b/t_f	κ_i	$D_i \, [Nmm^2]$	$(E\Gamma)_i \, [Nmm^4]$
$i = d$	20	$5/6$	$2.80 \cdot 10^5$	$2.96 \cdot 10^7$
$i = s$	20	$4.5 \cdot 10^{-2}$	$7.91 \cdot 10^6$	$2.96 \cdot 10^7$

Table 4.4. Values of the parameters used to plot eqs. (4.4) in fig. 4.11b. Taken from [P1].

Tab. 4.5 shows that for increasing values of the normalized crack length, the relative difference between the analytical and numerical energy release rate decreases.

The analytical and numerical values of the energy release rate are compared with the
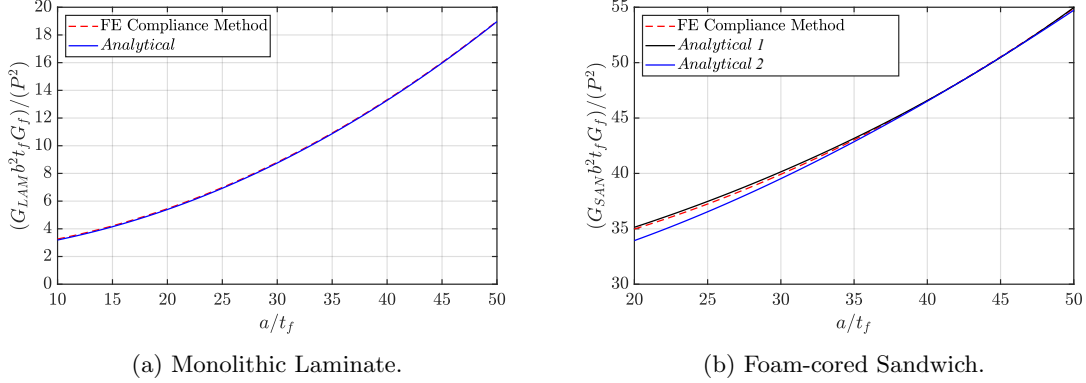
(a) Monolithic Laminate.

(b) Foam-cored Sandwich.

Figure 4.11. Comparison between the analytical, eqs. (4.4, 4.5) and the numerical dimensionless energy release rate vs. normalized crack length. $b/t_f = 15$ for the monolithic laminate and $b/t_f = 20$ for the sandwich specimen. Taken and adapted from [P1].

distribution of the local G along the crack front in figs. (4.12a)-(4.12b). The values of G_{FE} calculated with eq. (4.6), G_{SAN} and G_{LAM} match the local values of G_{CSDE} at the center of the specimen where $y/W = 0.5$. The relative differences between G_{LAM} and G_{SAN} and the local value of the energy release rate at $y/W = 0.5$ are 1.5% and 11.1%. Moreover, the local distribution of G_{tot} is more uniformly distributed in the laminate. A complex and oscillating stress field is present locally at the crack tip due to the presence of a bi-material interface in the sandwich specimen [35]. This could explain the reduced accuracy of the analytical model when applied to the sandwich case.

i	t_f [mm]	a/t_f	b/t_f	W/t_f	$(G_i - G_{FE})/G_i$ [%]
	2	10	15	13	2.23
Laminate	2	25	15	13	0.83
	2	40	15	13	0.33
	2	20	20	12	3.07
Sandwich	2	25	20	12	1.91
	2	30	20	12	1.00

Table 4.5. Comparisons between the analytical and numerical results $i = S, L$. The values of energy release rate for the sandwich G_S are taken from eq. 4.4 using $(k_r^i)_{avg}$. Taken from [P1].

The energy release rate peaks which are visible in figs. 4.12a-4.12b at coordinates $y/W = 0$ and $y/W = 1$, are due to the discontinuity of the crack front. The crack front intersects the longitudinal cuts (see fig. 4.1) at $y/W = 0$ and $y/W = 1$. In this region, the computation of the energy release rate is not accurate using the CSDE method, which is based on the solutions for plane and anti-plane conditions. The local displacement field at the crack front is described by other solutions near the free edges of the specimen, as it is explained in [77] and [78]. The value of W (see tab. 4.1) has been chosen in order to maximize the uniformity of the distribution of the local G_{Tot}.

It is important for specimen design and sizing to understand how the different deformation mechanisms (shear, bending and torsion) contribute to the total energy release rate G_{LAM} and G_{SAN}. Figs. 4.13a-4.13b represent the different terms appearing in eqs. (4.4) and (4.5) for a ratio $b/t_f = 15$ for the monolithic laminate and $b/t_f = 20$ for the sandwich specimen. The plot in fig. 4.13a shows that for very short crack lengths $a/t_f < 12$ the
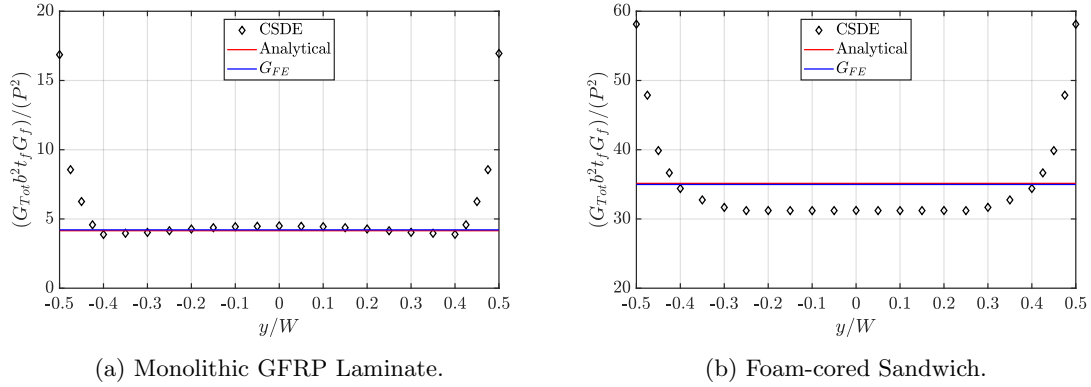
(a) Monolithic GFRP Laminate.   (b) Foam-cored Sandwich.

Figure 4.12. Comparison between distributions of G computed analytically, numerically with compliance method and numerically through the CSDE. The y coordinate is running along the crack front, where $y = 0.5$ corresponds to the specimen center. The analytical values of G_{tot} eqs. (4.4, 4.5) are plotted using the data from tabs. (4.1-4.4). The data are plotted for $a/tf = 15$ and $b/tf = 15$ for the monolithic laminate, $a/tf = 20$ and $b/tf = 20$ for the sandwich specimen. Taken from [P1].

shear deformation contribution dominates over those of bending and torsion, this is when the anti-plane conditions dominate. On the other hand, for long crack lengths $a/t_f > 20$ the bending deformation term prevails. However, there are intermediate crack lengths values $12 < a/t_f < 20$ for which all deformation contributions (shear, torsion and bending) are relevant. Fig. 4.13b displays a different trend for the composite sandwich case. The dominant energetic term is the torsional term in the range of crack lenghts considered for the sandwich $a/t_f < 50$. For $a/t_f > 50$, the energetic term representing the bending deformations varies quadratically with a/t_f (as for the monolithic laminate case) and it is always greater than the shear term.
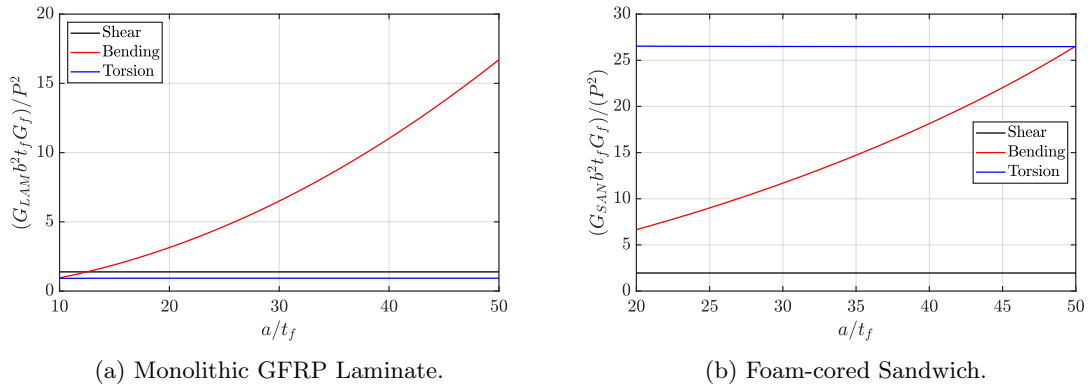
(a) Monolithic GFRP Laminate.   (b) Foam-cored Sandwich.

Figure 4.13. The contributions from shear, bending and torsion to G are shown when the defect length varies. The different contribution from eqs. (4.4, 4.5) are plotted using the data from tabs. (4.1-4.4). The data are plotted for $b/t_f = 15$ for the monolithic laminate and $b/t_f = 20$ for the sandwich specimen. Taken from [P1].

The torsional contribution to G remains constant (over the range of a/t_f studied) and equal to the uniform torsion solution of the problem both for the monolithic laminate and sandwich."

5.   TEST RIG AND EXPERIMENTAL PILOT TESTING

This chapter presents the experimental set up for the test rig and the results of the fracture characterization tests for monolithic laminates and foam-cored sandwhich specimens. The text and pictures are taken and adapted from [P2]. All the text parts taken and adapted from [P2] are reported in quotes "...".

5.1   Test rig presentation

Paragraphs are taken and adapted from [P2] "The test fixture is installed in a MTS 858 axial-torsional servo-hydraulic test machine operated with a MTS FlexTest 100 controller and the MTS TestSuite software package (fig. 5.1). Two servo-hydraulic actuators are present: one horizontal and one vertical. The horizontal actuator is clamped to a T-slot table in the test machine, and has a maximum capacity of 5 kN. It allows the application of the external load P (fig. 5.2) onto the cracked specimen. The vertical main actuator in the test machine, is an axial-torsional actuator with an axial capacity of 25 kN and torsional capacity of 250 Nm.

Two load cells are present in the text fixture: one is mounted on the horizontal actuator and has a capacity of 5 kN (fig. 5.2) and a second one is installed on the vertical actuator and has an axial capacity of 10 kN and torsional capacity of 200 Nm (fig. 5.1). The shearing load P is applied through compressive contact between the horizontal actuator and the load-block which is allowed to slide on a rail with linear bearings. However, the load-block is rigidly connected to the lower load-tab of the specimen, and this allows the load P to be transmitted through the specimen to the upper-load tab (fig. 5.2). An extensometer (MTS model 634.31F-25, with a 25 mm gauge length) is used to measure the relative sliding δ of the two load-tabs along the load application direction (fig. 5.2). The extensometer is linked to the two load tabs employing two steel connectors (fig. 5.2). In addition, a steel beam is clamped to the test machine lateral columns to prevent horizontal deformations to be applied to the vertical axial-torsional actuator, due to the presence of the horizontal side load P (fig. 5.2). The vertical actuator slides through a bearing positioned in a hole positioned at the middle of the steel beam.
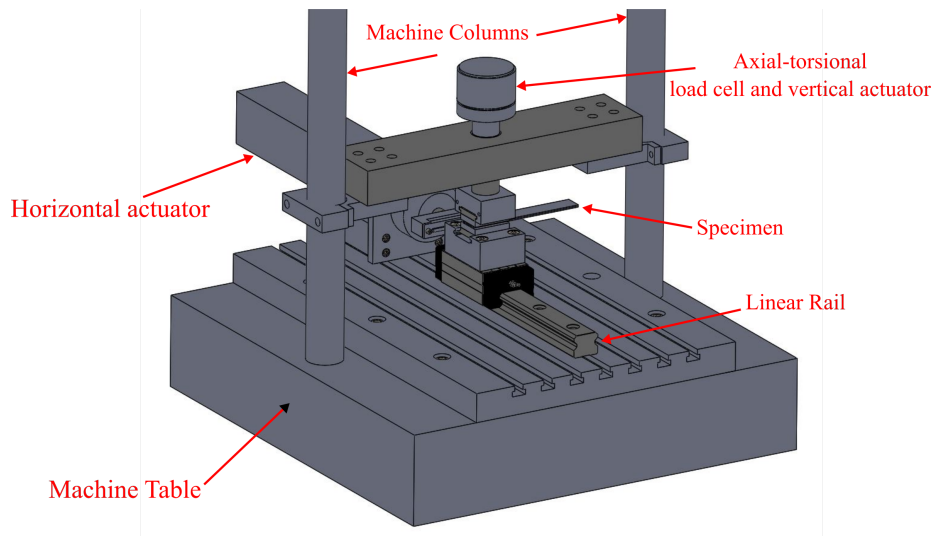
Figure 5.1. Overview of the test rig. Taken from [P2].
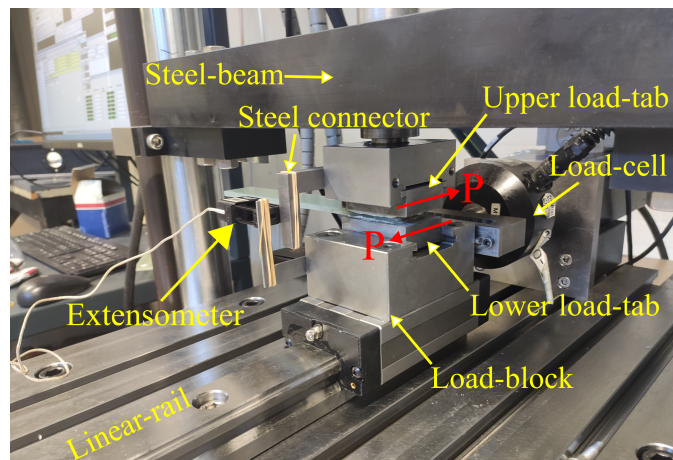
Figure 5.2. Test rig. Taken from [P2].

The upper load-tab is connected rigidly to the vertical actuator. Therefore, displacements and rotations of the surface of the upper load-tab are fully fixed. Instead, the lower load tab is capable of translating along the Y-axis (see fig. 5.3a). Thus, when the load P is applied along the Y-direction a reaction force P^R and two reaction moments M_X^R and M_Y^R act on the upper load tab (see fig. 5.3a). Fig. 5.3b shows the force and moment loads reported at the sections shear center of the two delaminated beams located at the crack front."
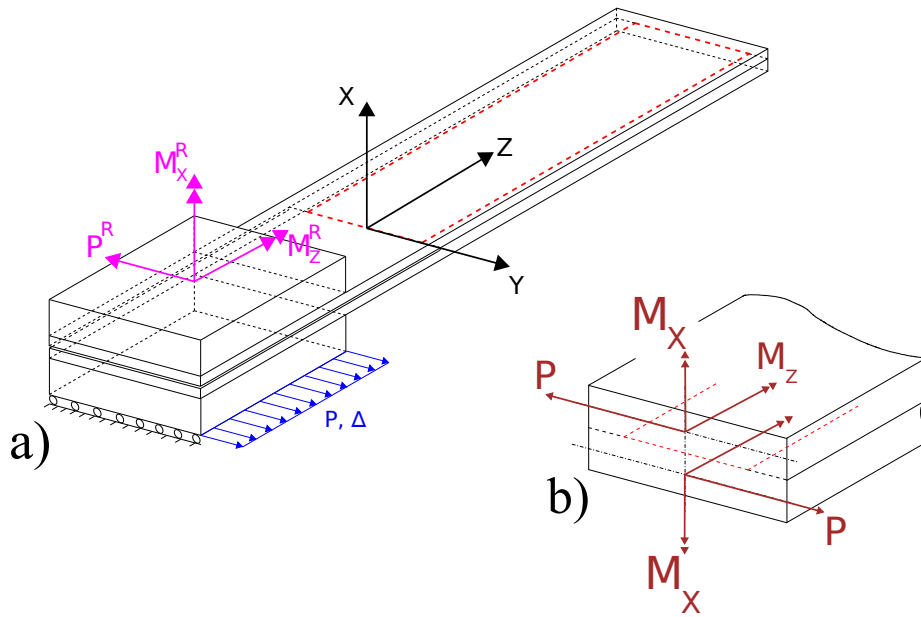
Figure 5.3. Illustration of the boundary conditions and load components applied to the specimen (monolithic laminate reported in the figure). a) The specimen with the external load applied to the lower load-tab (in blue) and the reaction force and moments on the upper load tab (purple) and b) the internal set of forces and moments acting at the crack front. Taken from [P2].

5.2   Specimens and fabrication

Paragraphs are taken and adapted from [P2] "Two monolithic laminate and composite sandwich plates were manufactured from which specimens were sourced (fig. 5.5). Both plates were manufactured using a vacuum infusion process (VIP), and the quality of the manufacturing process was verified by measuring the fibre volume fraction of the monolithic laminate plate according to [79] (see fig. 5.4).
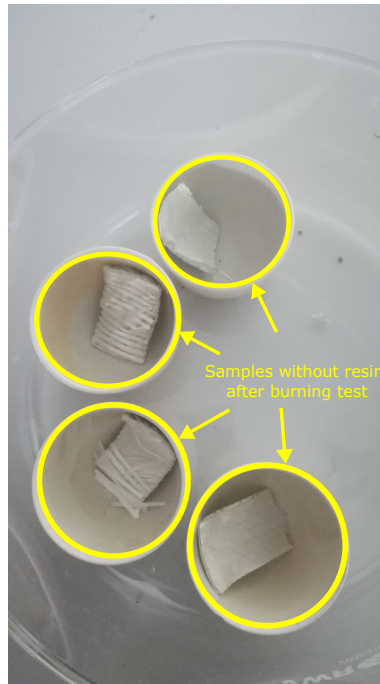
Figure 5.4. Illustration of cut-out samples from face sheet laminate after oven treatment.

An average fiber volume fraction of 49.6% was measured. A 350 x 500 mm plate was manufactured for the monolithic laminate specimens (fig. 5.5a), and a 300 x 400 mm plate for the composite sandwich specimens (fig. 5.5b). Figure 5.5a shows the location of Teflon$^{\circledR}$ inserts (grey parts) to facilitate a delamination between two plies or debond between the face sheet and core. The inserts consisted of 13 μm thick Teflon$^{\circledR}$ film. The plates were cured at room temperature for 2 weeks. The purple lines in fig. 5.5 indicate the lines along which cuts were made, using water-jet technology, to partition the specimens. The dimensions reported in fig. 3 should be consider as nominal without design tolerances. The nominal geometric dimensions of the monolithic laminate and the composite sandwich specimens are reported in tab. 5.1. The specific geometrical parameters of the individual specimens varied only slightly (+/- 0.5 mm) with respect to the nominal values in tab. 5.1.

The monolithic laminate plate consisted of 8 quadriaxial plies of Devold$^{\circledR}$ glass fiber crimp woven fabric infused with the Pro-Set$^{\circledR}$ INF-114 epoxy resin. The composite sandwich face sheets were made of the same glass fiber fabric and epoxy resin used for the monolithic laminate. The lay-up sequence for the monolithic laminate is $[(0/45/90/-45)_4||(0/45/90/-45)_4]$ where the symbol $||$ designates the Teflon$^{\circledR}$ insert. The composite sandwich specimens have the following lay-up configuration $[(0/45/90/-45)_4/Core/(0/45/90/-45)_4]$.
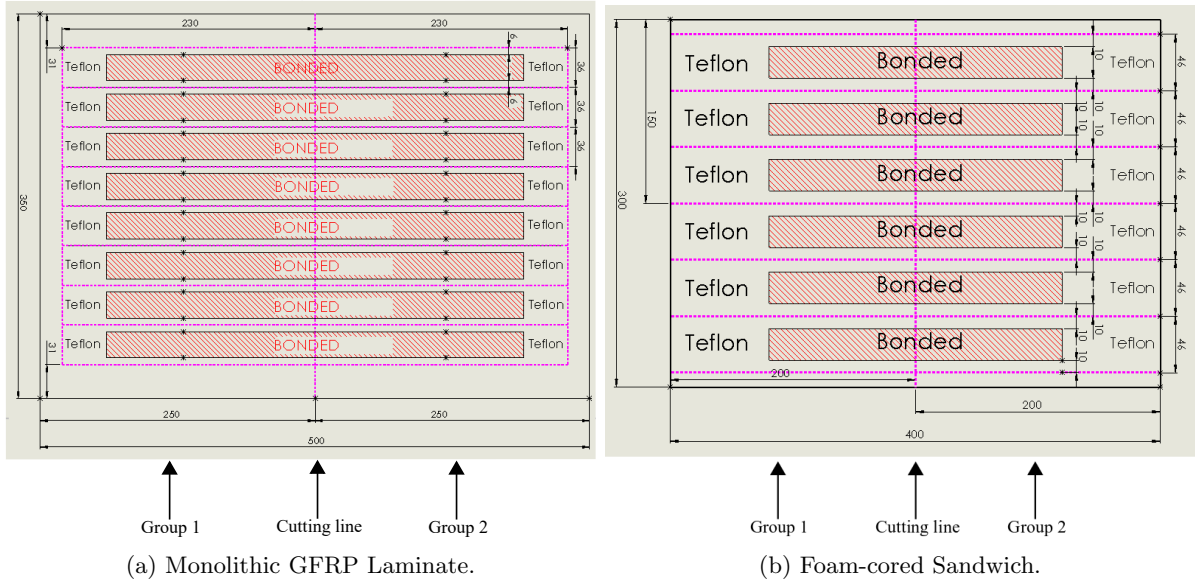
(a) Monolithic GFRP Laminate. (b) Foam-cored Sandwich.

Figure 5.5. Plate layout used for monolithic laminate and sandwich specimens. Taken and adapted from [P2].

	Geometry [mm]					
	t_f	t_c	a	b	W	L
Laminate	2	-	30	36	24	230
Sandwich	2	20	40	46	26	200

Table 5.1. Nominal geometrical parameters of the monolithic laminate and composite sandwich specimens. The parameters reported in the table symbolize the following geometrical dimensions: t_f is the semi-laminate and face-sheet thickness of the sandwich specimens, t_c is the core thickness, a is the crack length, b is the total specimen width, W is the width of the un-cracked specimen part, L is the specimen length. Taken from [P2].

The core is made of the open-cell H-series PVC foam manufactured by Diab® having a density of 80 $[kg/m^3]$. Additional sandwich specimens, also with a PVC H-series foam core but with a density of 45 $[kg/m^3]$ and a lay-up sequence $[(0/45/90/-45)_4/Core/(0/45/90/-45)_4]$, were also tested. The mechanical properties of the monilithic laminate, sandwich face sheets and core are already reported in tabs. 4.2-4.3 in section 4.1."

5.3 Test procedure

Paragraphs are taken and adapted from [P2] "A compliance calibration of the text fixture was carried out inserting a stiff steel block between the upper and lower load tabs. The compliance of the rig was then subtracted from the total compliance measured for each performed test. All tests were carried out quasi-statically in displacement control at a loading rate of 0.5 mm/min. The horizontal applied force P and fixture displacement δ were recorded throughout each test at a frequency of 3 Hz."

5.4 Data reduction method

Paragraphs are taken and adapted from [P2] "A representative force-displacement curve obtained for the monolithic laminate specimens is shown in fig. 5.7 as the red curve. The
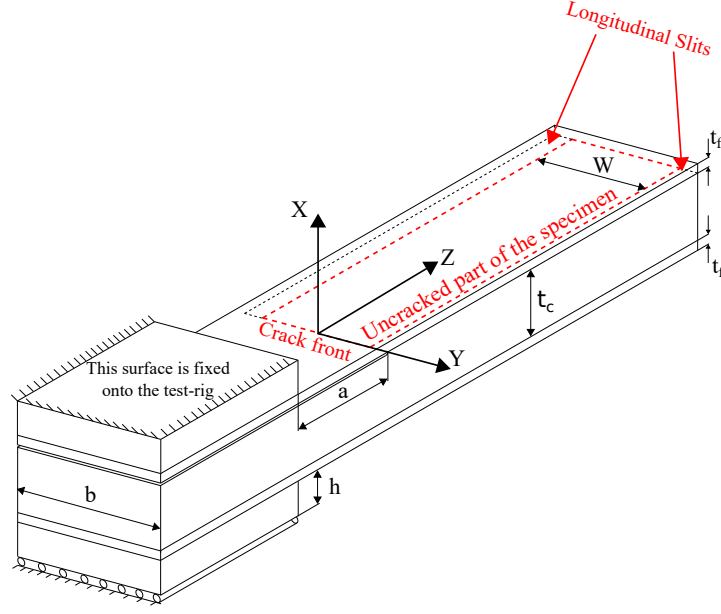
Figure 5.6. Sandwich specimen with the geometrical dimensions reported in tab. 5.1. Taken from [P2].

four load levels taken into consideration are:

- P_{Onset} The load at which the onset crack propagation can visually be observed during the experimental tests;

- P_{NL} The load value at which the load vs. displacement curve starts to deviate from linearity

- $P_{5\%}$ The load point where the compliance has increased by 5%;

- P_{MAX} is the maximum load recorder during the tests.

The initial slope of the experimental curve used to calculate the compliance was calculated for a load in the range of $250 - 500\ N$, and P_{NL} is calculated following the procedure outlined in [P2].

The critical value for energy release rate is then calculated substituting P_{Onset}, P_{NL}, $P_{5\%}$ and P_{MAX} to P into the expression for G found for the monolithic laminates in [P1]:

$$G_{LAM} = \frac{P^2}{WG_fA_f\kappa_d} + \frac{P^2a^2}{4WE_fI_f}\frac{(ak_r + 2E_fI_f)^2}{(ak_r + E_fI_f)^2} + \frac{(M_z(z=a))^2}{WD}\frac{(1-e^{2ac})^2}{(1+e^{2ac})^2}. \qquad (5.1)$$

and the composite sandwich specimens:

$$\begin{cases} G_{SAN} = G_d + G_s \\ G_d = \frac{P^2}{2WG_fA_f\kappa_d} + \frac{P^2a^2}{8WE_fI_f}\frac{(ak_r^d+2E_fI_f)^2}{(ak_r^d+E_fI_f)^2} + \frac{(M_z^d(z=a))^2}{2WD_d}\frac{(1-e^{2ac_d})^2}{(1+e^{2ac_d})^2} \\ G_s = \frac{P^2}{2W(GA)_s} + \frac{P^2a^2}{8W(EI)_s}\frac{(ak_r^s+2(EI)_s)^2}{(ak_r^s+(EI)_s)^2} + \frac{(M_z^s(z=a))^2}{2WD_s}\frac{(1-e^{2ac_s})^2}{(1+e^{2ac_s})^2}. \end{cases} \qquad (5.2)$$
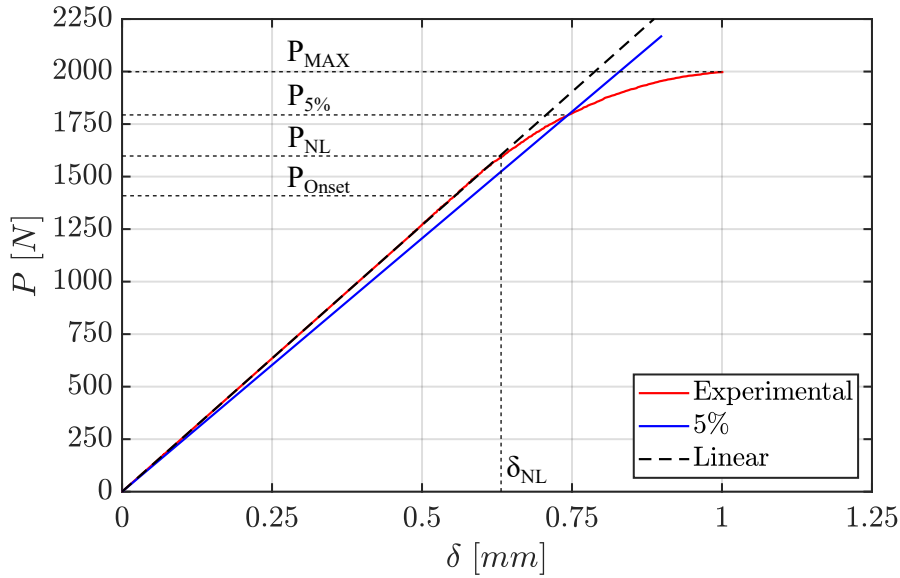
Figure 5.7. Force vs. displacement curve for a monolithic laminate specimen subjected to out-of-plane shear loads. The picture shows the different loads used to compute the critical value of the energy release rate for crack propagation. Taken from [P2].

Both expressions have been derived and presented in [P1].

The crack propagation was monitored from the top of the specimen both for the monolithic laminates and for the sandwich specimens. The transparency of the glass fibre laminate and sandwich face sheets allows visual monitoring of crack advance. It was not possible to detect the crack propagation from the side of the specimens (as it is usually done for other fracture tests such as in [80]), because the crack front is embedded in the specimen, and the crack edges are not visible from the specimen sides.

The crack propagation increment Δa is measured along the specimen width as it is shown in fig. 5.8. The parameter Δa is measured as the average distance (between the distances Δa_1, Δa_2, $\Delta a_n...\Delta a_{n+1}$) since the crack front shows for all the tested specimens a curved crack front as it is shown in fig. 5.8."
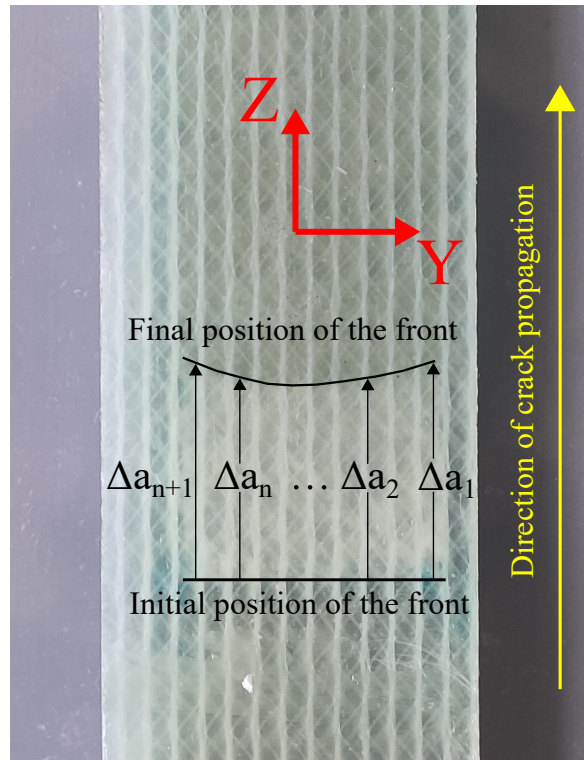
Figure 5.8. Top view of a cracked monolithic laminate specimen. The total crack length is computed as the average of the through-the-width distances between the Teflon® insert and the final position of the crack front. Taken from [P2].

5.5 Results and discussion

5.5.1 Experimental tests and results for the monolithic laminate specimens

Paragraphs are taken and adapted from [P2] "The monolithic laminate specimens, represented in fig. 5.5a, have been tested with a single crack propagation run per specimen. All specimens had the same initial crack length $a_0 = 30 \ mm$. After each propagation of the crack front, the specimen is unloaded and the crack propagation length $\Delta a = a_f - a_0$ (where a_f is the crack length after propagation) is measured. Seven monolithic laminate specimens were tested.

Figure 5.9 illustrates the load vs. displacement curves for the seven monolithic laminates specimens tested. The plots report the point where the onset of crack propagation is observed through a visual inspection of the specimen. The crack propagation length for each specimen is different because the specimens were unloaded at different propagation lengths.

All curves presented in fig. 5.9 exhibit a linear trend in the first loading phase until around 1300-1800 $[N]$. A stable crack propagation was observed for all specimen tested. The laminate is quasi-isotropic in the laminate plane (YZ plane in fig. 5.8). This multidirectional lay-up has been chosen in order to inhibit the propagation of intra-laminar cracks as it is suggested in [65]. Hence, the primary damage mode should be the advance of the original crack front. Moreover, it was visually observed that the crack propagated on the plane of the pre-implanted Teflon® insert without macroscopic kinking into other laminae as it was noticed in [65]."

(e) S   Specimen 6
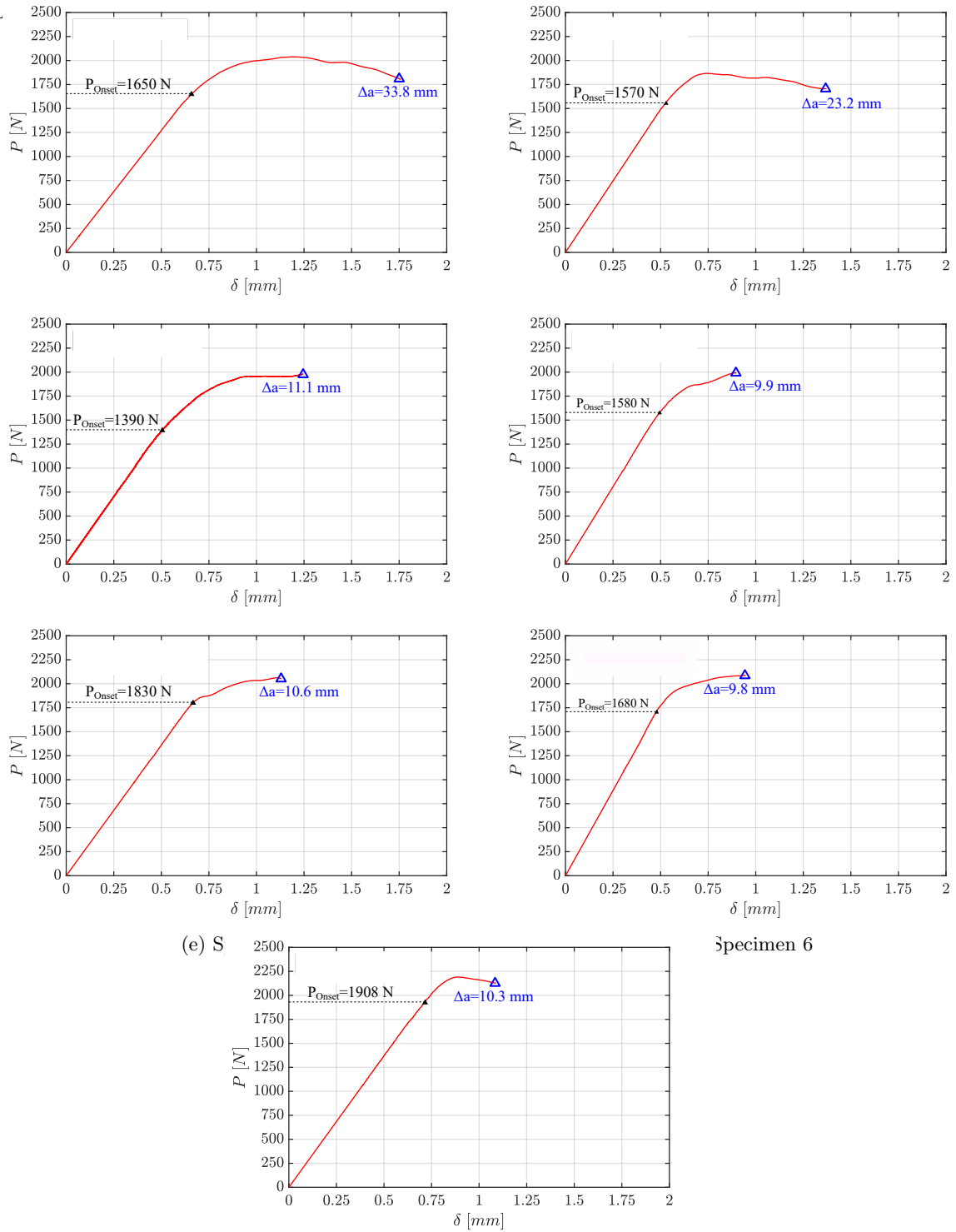
(g) Specimen 7

Figure 5.9. Experimental load vs displacement curve plots of the monolithic laminates specimens tested. P_{Onset} and the final crack propagation length $\Delta a = a_f - a_0$ are reported in each plot. The initial crack length is set $a_0 = 30mm$ for all the specimens. Taken from [P2].

Paragraph are taken and adapted from [P2] "The critical load points P_{NL}, $P_{5\%}$, P_{MAX} and P_{Onset} are reported in tab. 5.2. All the three critical loads P_{NL}, $P_{5\%}$ and P_{MAX} have a coefficient of variation which is lower than 10%. P_{MAX} has the lowest coefficient of variation (CV). $P_{5\%}$ has the highest CV. Usually, P_{NL} marks the deviation from linearity

in the load vs displacement curve and therefore P_{NL} is the load level at which damage (i.e. crack advance) starts to initiate in the specimen. In fact, the onset of crack propagation (from visual inspection) was observed at a load level equal to P_{Onset} and the relative difference between P_{Onset} and P_{NL} is lower than 4%."

Specimen	$P_{5\%}$ [N]	P_{max} [N]	P_{NL} [N]	P_{Onset} [N]	$(P_{Onset} - P_{NL})/P_{NL}$ [%]
1	1790	2038	1623	1650	1.6
2	1730	1865	1558	1570	0.8
3	1550	1979	1347	1390	3.2
4	1710	1992	1556	1580	1.5
5	1865	2061	1811	1830	1.1
6	1915	2086	1652	1680	1.7
7	2150	2191	1840	1908	3.7
Average [N]	1816	2030	1627	1658	-
Std [N]	174.8	93.6	154.9	159.6	-
CV [%]	9.6	4.6	9.5	9.6	-

Table 5.2. P_{NL}, $P_{5\%}$, P_{MAX}, P_{Onset} and the relative difference between P_{Onset} and P_{NL} are computed for each monolithic laminate specimen along with their average, standard deviation (Std) and coefficient of variation (CV). The initial value for the crack length is $a_0 = 30\ mm$ for all the specimens, see figs. 5.7 and 5.9. Taken from [P2].

Specimen	$G_c^{5\%}$	G_c^{max}	G_c^{NL}	G_c^{Onset}	$(G_c^{Onset} - G_c^{NL})/G_c^{NL}$
-		[J/m^2]			[%]
1	483	626	397	410	3.3
2	447	519	362	368	1.6
3	518	844	391	416	6.4
4	463	629	384	396	3.2
5	620	757	584	596	2.0
6	615	730	458	473	3.4
7	766	796	561	603	7.5
Average [J/m^2]	559	700	448	446	-
Std [J/m^2]	115	114	90	96	-
CV [%]	20.5	16.2	20.1	20.7	-

Table 5.3. The critical values of the energy release rate $G_c^{5\%}$ G_c^{max}, G_c^{NL}, G_c^{Onset} by inserting $P_{5\%}$, P_{MAX}, P_{NL}, P_{Onset} (tab. 5.2) into eq. 5.1 are reported. Taken from [P2].

Paragraphs are taken and adapted from [P2] "Table 5.3 reports the critical values for the energy release rate computed by inserting $P_{5\%}$, P_{MAX}, P_{NL}, P_{Onset} into eq. 5.1. The critical energy release rate that shows the highest average value is G_c^{max} (700 [J/m^2]) followed by $G_c^{5\%}$ (559 [J/m^2]) and G_c^{NL} (448 [J/m^2]). G_c^{max} has the lowest coefficient of variation of 16.2 %, and $G_c^{5\%}$ has the highest CV equal to 20.5 %. G_c^{Onset} is also reported and its maximum relative difference with respect to G_c^{NL} is 7.5 %. G_c^{Onset} corresponds to the delamination initiation from the insert and therefore it cannot be affected by non-linear effects, such as fiber bridging.

The high scatter (high coefficient of variance) in the values for the critical energy release rates G_c^{max} shows how the length of crack propagation Δa has an effect on the value of the

critical energy release rate. Moreover, it is not possible to clearly identify which load value should be used (among $P_{5\%}$, P_{MAX}, P_{NL}, P_{Onset}) in order to define the fracture toughness as a critical value for the energy release rate due to the large scatter in the results. However, a larger data set from more tested specimens may improve the statistical decision making, so that several or all load values identify the same load level. Furthermore, the effect of the micro-mechanical shape of the Teflon-dominated initial crack front may have an influence on the onset of crack propagation."

5.5.2   Experimental tests and results for sandwich composite specimens

Paragraphs are taken and adapted from [P2] "The same experimental procedure employed for the monolithic laminate specimens has been used for the composite sandwich specimens. An initial crack length of $a_0 = 40\ mm$ was used for all specimens tested. Eight specimens with a Divinycell® H80 core and two H45 specimens were tested. The specimens having the H80 core were installed in order to pre-crack because often in PVC foam cores with an artificial Teflon®-filmed debond, the artificial Teflon® insert forms a crack which is usually composed of partially resin filled core cells. This will create an artificial tough region at the crack front, which acts like a barrier for initiation of crack propagation. In order to break this tough region and to perform pre-cracking (see fig. 5.12), pre-cracking was performed by applying: a sinusoidal cyclic load with an amplitude of 10-15 % of the static mode-I propagation load, and with a load ratio $R = 0.1$ and a frequency of 3 Hz, until a propagation of $2 \pm 0.5\ mm$ was observed. The amplitude was however increased up to 35 % of the static propagation load when crack growth was not observed. This increase in amplitude was applied to 6 specimens out of 8 (having the H80 core) in order to pre-crack. The length of the new crack after propagation was measured with the method illustrated in fig. 5.8.

The experimental load vs displacement curves showed a strong non-linear behaviour as shown in fig. 5.10. A representative experimental curve (calculated as the average of the experimental curves corresponding to the specimens having the H80 core) is shown in figure fig. 5.11. Moreover, a macroscopic crack propagation was not visible throughout the loading phase during the experiment. Hence, the data reduction method developed in section 4.1 cannot be used to extract a critical value for the energy release rate. In fact, the two main assumptions required to apply eq. 5.2 are not satisfied: the specimen response is neither linear nor onset of crack propagation can be observed during the experiments. Therefore, the non-linear behaviour in fig. 5.11 must be considered as a consequence of a damage mechanism in the specimen which dissipates energy when the load P is applied. Two different hypotheses were proposed in order to justify the non-linear behaviour showed in fig. 5.11: (i) either a large-scale damage process zone is present at the crack front (see fig. 5.12) or (ii) the foam core behaves in a non-linear manner under the shear and torsional load applied , which is the case when H-series foam core material is subjected to high shear strain magnitudes [81]. In order to verify these two hypotheses, two investigations were carried out."
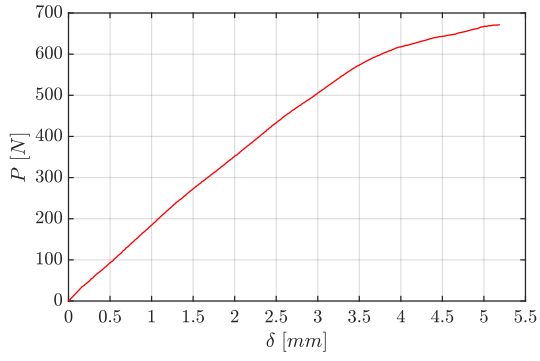
(a) Specimen 1
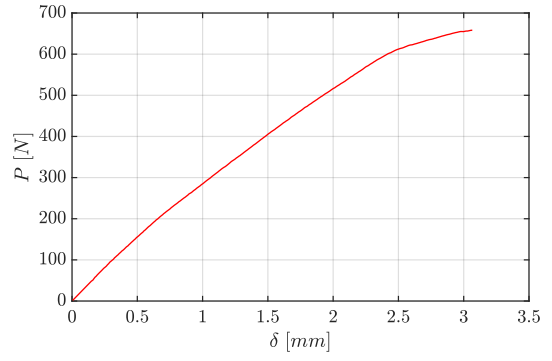
(b) Specimen 2
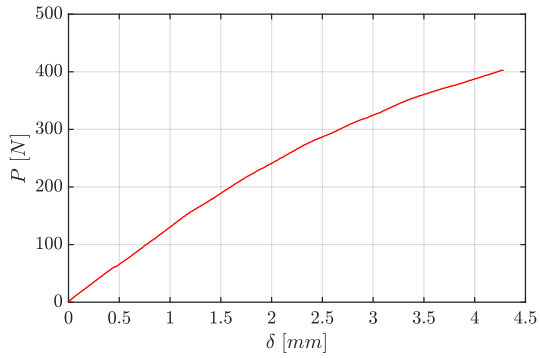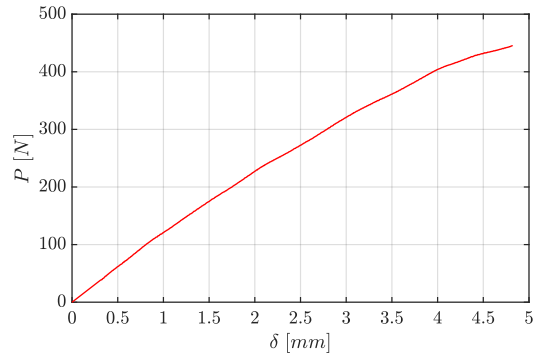
Figures (a) and (b) refers to H80 foam core

(c) Specimen 3

(d) Specimen 4

Figures (c) and (d) refers to H80 foam core
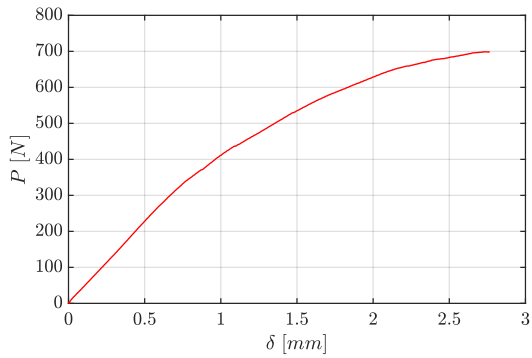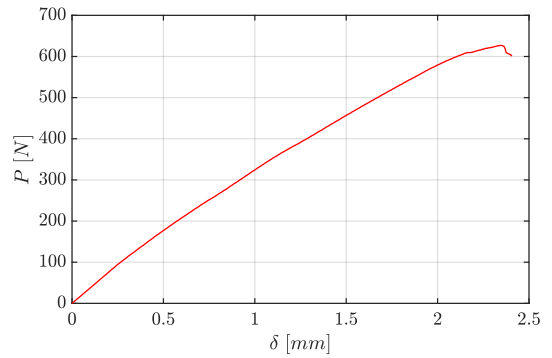
(e) Specimen 5

(f) Specimen 6

Figures (e) and (f) refers to H80 foam core
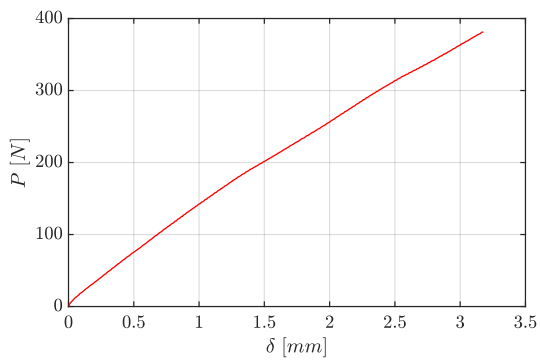
(g) Specimen 7
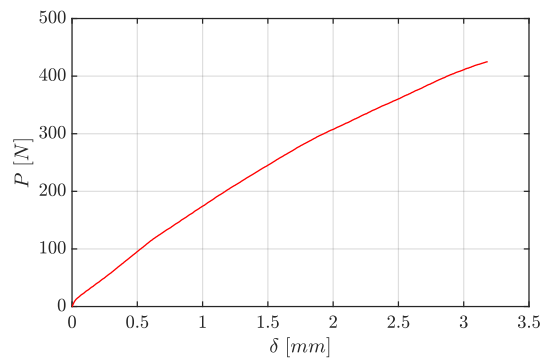
(h) Specimen 8

Figures (g) and (h) refers to H80 foam core
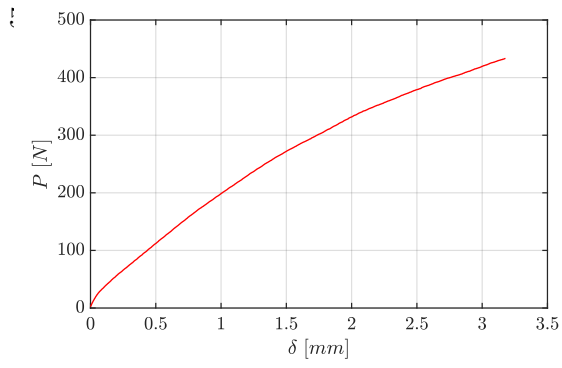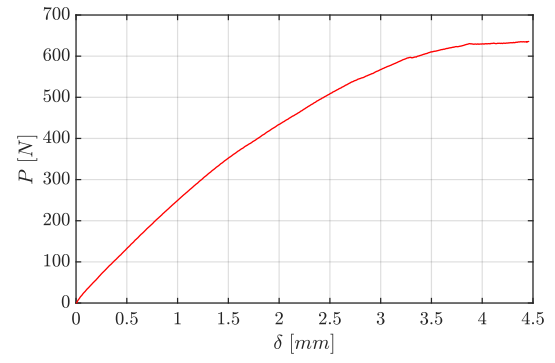
(i) Specimen 9 (j) Specimen 10

Figure 5.10. Experimental load vs displacement curve plots of the sandwich specimens tested. Figures (a)-(i) corresponds to specimens having H80 core, instead figure (j) corresponds to H45 foam core. Taken from [P2].
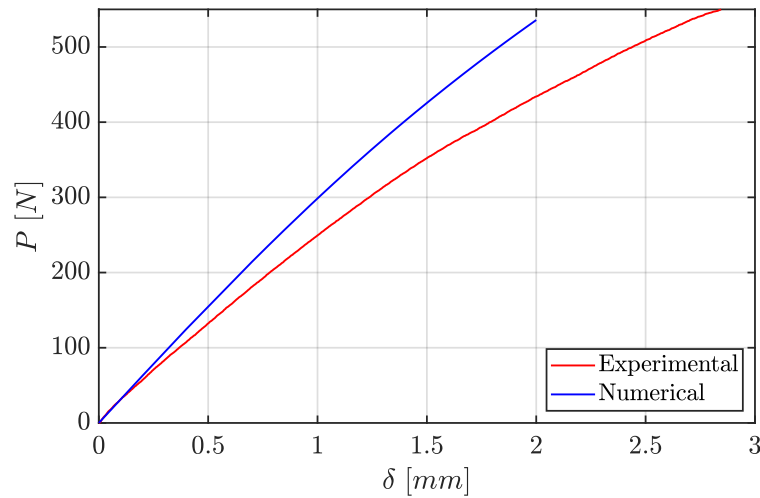
Figure 5.11. Experimental and numerical force vs. displacement curves for a composite sandwich specimen having quasi-isotropic face sheets and a Divinycell® H80 core ($[(0/45/90/-45)_4/Core/(0/45/90/-45)_4]$) subjected to out-of-plane shear loads. The initial crack length is set $a_0 = 40mm$. Taken from [P2].
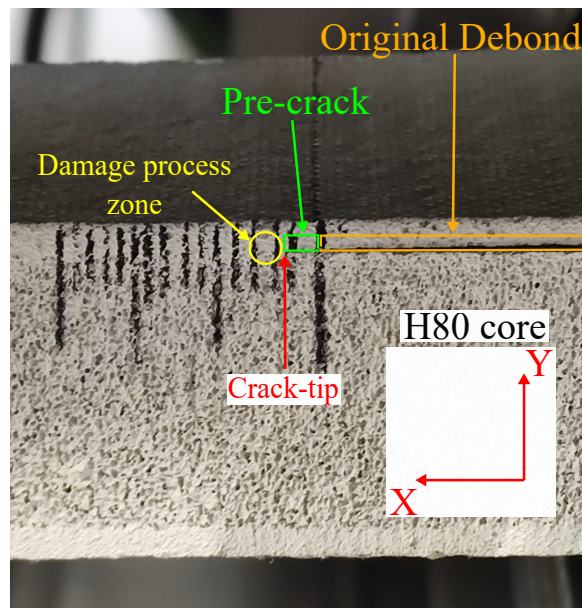
Figure 5.12. Crack front detail of a cracked H80 sandwich specimen.

Paragraphs are taken and adapted from [P2] "PVC foams can exhibit a non-linear relationship between stresses and strains in shear loading, as reported in [81]. Therefore, the same FE model described and documented in [P1] has been modified in order to adopt non-linear material behaviour of the foam core in shear with no damage modeling. The shear stress/strain curve, taken from [82], is converted into a tensile stress/strain curve following the procedure outlined in [82] for the H80 PVC foam used in the experimental setup. The methodology proposed in [82] assumes a von-Mises based criterion to model the yielding response of a closed cell foam. The load vs. displacement curve computed from the FE model is presented in fig. 5.11 along with the experimental curve. Fig. 5.11 shows

that the numerical results also predict a non-linear response of the specimen subjected to the same load levels applied during the fracture characterization testing. The experimental curve (see fig. 5.11) deviates significantly from the numerical results for loads P higher than 35 [N]. Hence, the contribution to the total non-linear experimental behaviour (fig. 5.11) could be a combination of a non-linear material behaviour of the foam itself as well as the presence of large-scale damage at the crack front region.

All foam cored sandwich specimens were investigated by destructive inspection after load application, in order to investigate whether damage was visible at or near the crack front. Each specimen was cut along the plane represented in fig. 5.13a. The distance d (along the Y-axis, see 5.13a) between the plane of cutting and the crack plane was 2 mm. Fig. 5.13b illustrate that multiple cracks are present just below the face-sheet/core interface embedded in the core. The presence of these cracks in the core could be associated to either the kinking of the initial debond front into the core, or to a damage mechanism similar to the one observed and described for monolithic laminates in [65]. In the latter case, the intra-laminar cracks observed in [65] can be related to the core-cracks observed herein. Further studies are necessary to investigate the cause of the initiation of these embedded core-cracks appearing under pure mode III loading, as mode III crack mechanisms in foam cored sandwich specimens are not currently reported in the open literature."
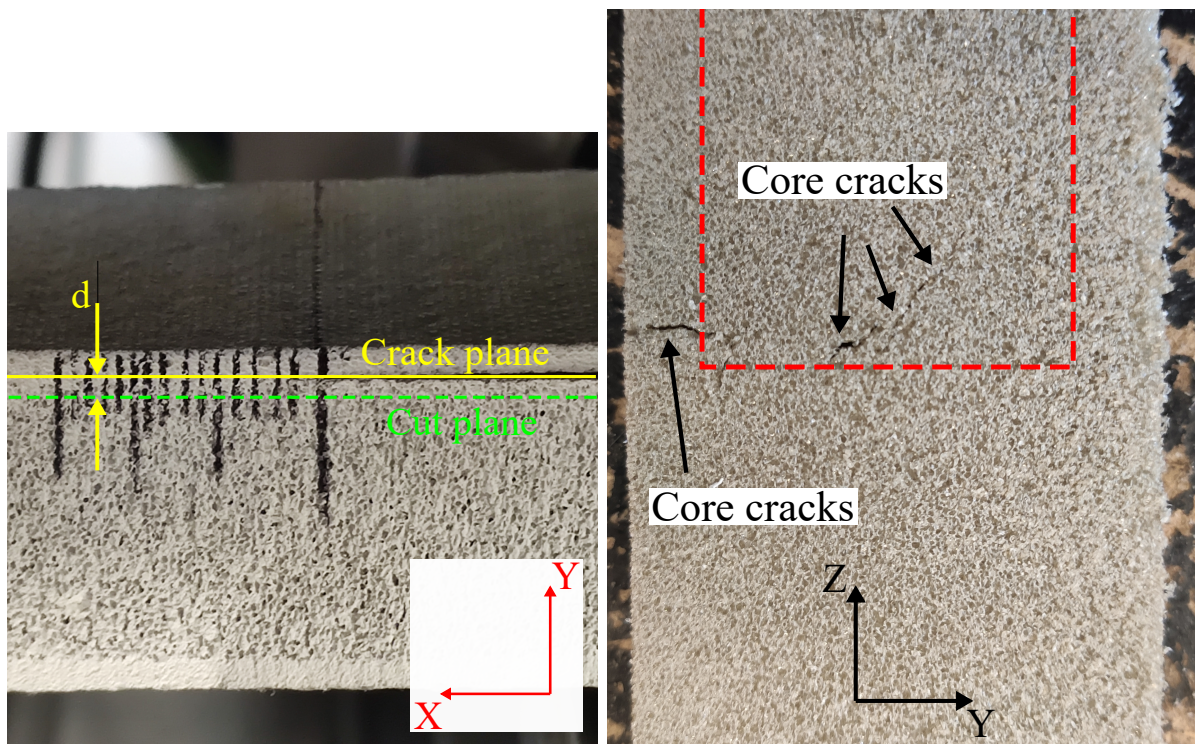
(a) Cutting Plane.

(b) Core cracks.

Figure 5.13. The plane of cut and core cracks are shown. Taken from [P2].

The sandwich specimens with a H45 core were additionally tested in order to understand if a specimen with a more brittle core, compared to the H80 core, was showing a less non-linear behaviour.
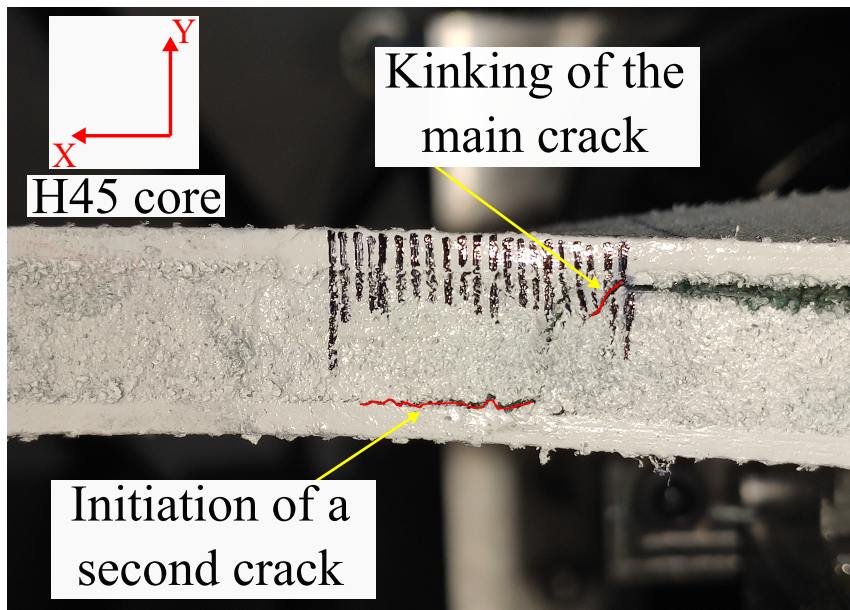
Figure 5.14. Crack front detail of a cracked H45 sandwich specimen. Taken from [P2].

Fig. 5.14 illustrates one of the tests done on the H45 cored specimens. The picture is representative of the crack propagation behaviour of all the specimens having an H45 core. The crack kinks into the core and initiation of secondary cracks is present between the core and the lower face sheet. The low shear strength value (0.56 MPa) of the H45 cores makes this kind of mode III fracture characterization test not suitable for sandwich specimens."

6.   Conclusions and future work

The main scope of this PhD project was to build a novel test rig and develop a data reduction method capable to analyse interface cracks problems in composite structures subjected to out-of-plane shear loads. The materials taken into consideration were the ones most employed in the marine sector as quasi-isotropic glass fiber monolithic laminates and PVC foam-cored sandwiches having quasi-isotropic glass fiber face-sheets.

Out-of-plane shear loadings induce a dominant mode-III stress state along the crack front. The crack problem was analysed using the linear elastic fracture mechanics theory in order to develop an analytical model able to predict the value of the energy release rate G during the experimental test. The specimen geometry was chosen accordingly to previous studies carried out in the literature as in [25].

Analytical expressions for G are derived for cracked composite sandwich and monolithic laminate specimens loaded in the shear-torsion-bending (STB) test rig configuration [25]. The analytical model is derived using first order shear deformation theory and Vlasov theory for non-uniform torsion of elastic beams and accounting for the effects of the near front deformations. The expressions of G can be used in connection with data reduction for the fracture test specimen presented in [68]. The analytical equations for G take into account the influence of all the geometrical/material parameters of the specimen. An expression for G was derived before in [25] for monolithic laminates. The main difference is that the equation derived here is fully analytical for monolithic laminates and requires, for a sandwich, just one parameter that can be determined experimentally or numerically. Moreover, the equations for G are expressed in function of the crack length instead the one presented in [25] can be used only for one value of a.

The analytical expressions of G are particularized for the presented material combinations. A comparison between the analytical model and a high-fidelity FE based fracture mechanics model is performed. The energy release rate is extracted from the numerical model globally using a compliance-based method and locally employing a displacement-based method. The biggest mismatch between analytical and numerical results is present in the sandwich specimen case, probably because local effects close to the crack front have a relevant influence on the local G distribution. These local effects are confined to a region surrounding the crack front and the beam theory, that has been used, is not capable to describe them accurately. Moreover, the analytical model predicts an unstable crack growth if the fracture test presented in [68] is carried out in load control both for the monolithic laminate and for the foam-cored sandwich case. The analysis also confirms how it is not possible to achieve a pure anti-plane stress state (even in the central region of the crack front), because of the finite value of the specimen width b. Although, it is feasible to have a dominant mode-III component of the energy release rate in a rather big zone along the crack front using the specimen geometry selected for the fracture characterization test.

A pilot experimental campaign was carried out using monolithic laminate and foam-cored sandwich specimens. The experimental tests were carried out over 7 monolithic laminates (having a quasi-isotropic lay-up) and eight sandwich specimens. The monolithic laminate showed a linear behaviour until onset of crack propagation and the crack propagates along the initial delamination plane. Hence, the analytical model developed was used to extract the critical value of G at different selected experimental loads. The foam-cored specimens showed a strong non-linear behaviour in the load vs displacements plots and no crack propagation was visible during the experiments. It was found out that both the non-linear material behaviour (under shear loads) of the PVC foam and the presence of core-cracks were probably the causes of the specimen non-linear response. Thus, the assumptions underlying the analytical model are violated in the case of the sandwich specimen and consequently the application of the data reduction method cannot be directly done for the the PVC foam cored specimens.

The following proposals/recommendations can be made for future work, based on the results presented in Paper [P1] and in the pilot experimental campaign [P2]:

1) The beam geometry should be abandoned in favour of wider specimens, as the numerical analyses showed in [P1]. In fact, the distribution of G along the crack front becomes more uniform if the width of the specimen increases and the stress state is closer to the pure anti-plane problem as shown in [P1];

2) The coupling between mode II and III at the traction-free specimens edges could be avoided only changing the specimen geometry. A geometry that do not present any crack front discontinuity should be used. A cylindrical specimen subjected to torsion could be probably used in order to avoid the presence of free edge effects;

3) The core strength must be higher than the toughness of the interface, i.e. the core do not have to show any damage or non-linear behaviour under shear loads before the onset of crack initiation. Therefore, it is suggested the employment of foam cores having higher density like Divinycell$^\text{®}$ H200, H250 or metallic foams;

4) A digital image correlation (DIC) analysis of both the test fixture and the specimen would lead to a deeper and consolidated understanding on how overall mechanics of the problem studied;

5) The addition of rigid steel plates to the face sheets of the sandwich specimen would increase the torsional stiffness of foam cored beam. In this way, the application of the out of plane shear load P would be promoted and the rigid rotation of the unloaded part of the specimen would be avoided;

6) The implementation of a new device is necessary to track more efficiently the crack length during propagation. Moreover, materials having non-transparent face sheets (as in the case of carbon fiber face sheets) an ultrasonic scanning device should be coupled to the text fixture in order to monitor the crack propagation.

REFERENCES

[1] I. Verpoest P. Jochen. Sandwich Materials Selection Charts. *Journal of Sandwich Structures and Materials*, pages 407–421, Septembe 1 2006. doi: https://doi.org/10.1177/1099636206065521.

[2] J.L. Gibson M.F. Ashby. Cellular solids-structure and properties. *Cambridge University Press*, 1997.

[3] M.F. Ashby. Designing hybrid materials. *Acta Metall. Mater.*, 51:5801–5821, 2003.

[4] M.F. Ashby. Materials and process selection in mechanicsl design. *Butterworth Heinemann*, 1999.

[5] T.S.B of Canada. Loss of rudder, airbus 310-308, air transat flight 961. *TSB*, 1(1):–, 2005.

[6] G.A. Kardomateas L.A. Carlsson. Structural and failure mechanics of sandwich composite. *Springer Science & Business Media*, 1(1):10–20, 2011.

[7] D. Zenckert. An investigation to sandwich construction. *Chamaleon Press*, 1995.

[8] B. Hayman. Inspection and repair of sandwich structures in naval ships. *Det Norske Veritas technical report*, 1(1):1–302, March 2007. doi: -.

[9] E.H. Glaessagen, J.R. Reeder, D.W Sleight, J.T. Wang, I.S. Raju, and C.E. Harris. Debonding failure of sandwich-composite cryogenic fuel tank with internal core pressure. *Journal of spacecraft and rockets*, 32(4):613–627, 2005.

[10] U. Vantini. Investigating effects of pure shear defirmation in wind turbine blade sub-structure. *Master's Thesis, Politecnico di Milano*, 1(1):–, 2014.

[11] YS. Chai KM. Leichti. Asymmetric shielding in interfacial fracture under in-plane shear. *Journal of Applied Mechanics*, pages 295–304, 1992.

[12] AG. Evans HC. Cao. An experimental study of the fracture resistance of bimaterial interfaces. *Mechanics of Materials*, pages 295–304, 2018.

[13] C. Berggreen. Damage Tolerance of Debonded Sandwich Structures. 2004.

[14] L. A. Carlsson L. S. Sendlein S. L. Merry . Characterization of Face Sheet/Core Shear Fracture of Composite Sandwich Beams. *Journal of Composite Materials*, 25 (25):101–116, 1991. ISSN 1530793X. doi: 10.1177/002199839102500105.

[15] F. Aviles LA. Carlsson. Analyses of the sandwich DCB specimens for debond characterization. *Engineering Fracture Mechanics*, pages 153–168, 2008.

[16] X. Li LA. Carlsson. Fracture Mechanics analysis of the tilted sandwich debond (TSD) specimen. *Journal of Composite Materials*, pages 2145–2168, 2001.

[17] W.J. Cantwell J. Ratcliffe. Center notched flexure sandwich geometry for characterizing skin-core adhesion in thin-skinned sandwich structures. *Journal of reinforced plastics and composites*, pages 945–970, 2001.

[18] TK. Jacobsen BF. Sørensen, K. Jørgense and RC. Østergaard. DCB specimen loaded with uneven bending moments. *International Journal of Fracture*, pages 163–176, 2006.

[19] R. Moslemian. Residual strength and fatigue lifetime of debond damaged sandwich structures. *PhD Thesis*, pages 77–80, 2011.

[20] C.C. Poe E.H. Glaessgen, I.S. Raju. Delamination and stitched failure in stitched composite joints. *In Conference Proceedings: 40th AIAA/ASME/ASCE/AHS/ASC Structures, Structural Dynamics and Materials Conference and Exhibit*, 2017.

[21] G. Lu F. Zhu. A Review of Blast and Impact of Metallic and Sandwich Structures. *Electronic Journal of Structural Engineering*, 2017.

[22] R. Palaninathan K. Senthil, A. Arockiarajan. Experimental determination of fracture toughness for adhesively bonded composite joints. *Engineering Fracture Mechanics*, pages 24–42, 2015. doi: http://dx.doi.org/10.1016/j.engfracmech.2015.11.015.

[23] S.M. Lee. An edge crack torsion method for mode III delamination fracture testing. *Journal of composites technology and research*, 15(3):193–201, 1993. ISSN 0884-6804. doi: 10.1520/CTR10369J.

[24] A. Szekrenyes. Improved analysis of the modified split-cantilever beam for mode-iii fracture. *Int J Mech Sci*, 51(9-10):682–693, 2009. doi: https://doi.org/10.1016/j.ijmecsci.2009.07.005.

[25] B.D. Davidson and F.O. Sediles. Mixed-mode I-II-III delamination toughness determination via a shear-torsion-bending test. *Composites Part A: Applied Science and Manufacturing*, 2011. ISSN 1359835X. doi: 10.1016/j.compositesa.2011.01.018.

[26] J. Ratcliffe. Characterization of the edge crack torsion test for mode iii fracture toughness measurement of laminated composites. *NASA-TM*, 1(213269), 2004.

[27] D. Zenckert. The handbook of sandwich costruction. *EMAS Chamaleon Press Ltd.*, 1997.

[28] CMH-17. Composite materials handbook volume 6. *Structural Sandwich Composites*, 6:–, 2013.

[29] ASTM International. ASTM D5528-13 Standard Test Method for Mode I Interlaminar Fracture Toughness of Unidirectional FIber-reinforced Polymer Matrix Composites. *ASTM*, 2013.

[30] ASTM International. ASTM D6115-97 Standard Test Method for Mode IFatigue Delamination Growth Onset of Unidirectional Fiber-Reinforced Polymer Matrix Composites. *ASTM*, 2011.

[31] ASTM International. ASTM D6671/D6671M-13e1 Standard Test Method for Mixed Mode I-Mode II Interlaminar Fracture Toughness of Unidirectional Fiber Reiforced Polymer Matrix Composites. *ASTM*, 2013.

[32] ASTM International. ASTM D7905/D7905M-14 Standard Test Method for Determination of the Mode II Interlaminar Fracture Toughness of Unidirectional Fiber Reiforced Polymer Matrix Composites. *ASTM*, 2014.

[33] A.A. Griffith. The phenomenon of rapture and flow in solids. *Philosophical transactions of the royal society of london. Series A, containing papers of a mathematical or physical character*, pages 163–198, 1921.

[34] J. Kies G. Irwin. Fracturing and fracture dynamics. *Welding Journal*, pages 95–100, 1952.

[35] Z. Suo. Singularities, Interfaces and Cracks in Dissimilar Anisotropic Media. *Proceedings of the Royal Society of London*, pages 331–358, 1990.

[36] S.N. Alturi H.G. Beom. Dependence of stress on elastic constants in an anisotropic bimaterial under plane deformation; and the interfacial crack. *Computational Mechanics*, pages 106–113, 1995.

[37] J. Dundurs. Edge-bonded dissimilar orthogonal elastic wedge. *J Appl Mech*, pages 650–652, 1969.

[38] C. Berggreen L. Barbieri, R. Massabó. The effects of shear and near tip defomations on interface fracture of symmetric sandwich beams. *Engineerign Fracture mechanics*, pages 298–321, 2018. doi: https://doi.org/10.1016/j.engfracmech.2018.06.039.

[39] T. Nakamura. Three-Dimensional Stress Fields of Elastic Interface Cracks. *Journal of Applied Mechanics*, pages 939–946, 1991.

[40] S. Charalambides P. Matos, R. McMeeking and M.Drory. A method for calculating stress intensities in bimaterial fracture. *International Journal of Fracture*, pages 235–254, 1989.

[41] R. Smelser. Evaluation of stress intensity factors for bimaterial bodies using numerical crack flank displacement data. *International Journal of Fracture*, pages 135–143, 1989.

[42] W. Zhang P. Charalambides. An energy method for calculating the stress intensities in orthotropic bimaterial fracture. *International Journal of Fracture*, pages 135–143, 1989.

[43] B. C. Simonsen C. Berggreen. *Non-uniform compressive strength of debonded sandwich panels - II. Fracture mechanics investigation*, volume 7. 2005. ISBN 1099636205. doi: 10.1177/1099636205054790.

[44] C.T. Sun. Fracture Mechanics. *Elsevier*, pages 1–366, 2011.

[45] J. P. Benthem. State of stress at the vertex of a quarter-infinite crack in a half-space. *International Journal of Solids and Structures*, 13(5):479–492, 1977. ISSN 00207683. doi: 10.1016/0020-7683(77)90042-7. URL http://dx.doi.org/10.1016/0020-7683(77)90042-7.

[46] G. Dhondt. Analysis of the boundary layer at the free surface of a half circular crack. *Engineering Fracture Mechanics*, 60(3):273–290, 1998. ISSN 00137944. doi: 10.1016/S0013-7944(98)00026-5.

[47] G. C. Sih R. J. Hartranft. An approximate three-dimensional theory of plates with application to crack problems. *International Journal of Engineering Science*, 8(8): 711–729, 1970. ISSN 00207225. doi: 10.1016/0020-7225(70)90054-6.

[48] D. N. Fenner and M. J. Abdul Mihsein. Crack front elastic stress state for three-dimensional crack problems. *International Journal of Fracture*, 25(2):121–131, 1984. ISSN 03769429. doi: 10.1007/BF01141555.

[49] T. Nakamura and D. M. Parks. Antisymmetrical 3-D stress field near the crack front of a thin elastic plate. *International Journal of Solids and Structures*, 25 (12):1411–1426, 1989. ISSN 00207683. doi: 10.1016/0020-7683(89)90109-1. URL http://dx.doi.org/10.1016/0020-7683(89)90109-1.

[50] T Nakamura. Elastic Interface Cracks. 58(December), 1991.

[51] P. Pook. A 50-year retrospective review of three-dimensional effects at cracks and sharp notches. *Fatigue and Fracture of Engineering Materials and Structures*, 36(8): 699–723, 2013. ISSN 8756758X. doi: 10.1111/ffe.12074.

[52] A. Campagnolo P. Pook, F. Berto and P. Lazzarin. Coupled fracture mode of a cracked disc under anti-plane loading. *Engineering Fracture Mechanics*, 128(C):22–36, 2014. ISSN 00137944. doi: 10.1016/j.engfracmech.2014.07.001.

[53] A. Campagnolo P. Pook, F. Berto and P. Lazzarin. Coupled fracture mode of a cracked disc under anti-plane loading. *Engineering Fracture Mechanics*, 128 (C):22–36, 2014. ISSN 00137944. doi: 10.1016/j.engfracmech.2014.07.001. URL http://dx.doi.org/10.1016/j.engfracmech.2014.12.021.

[54] P. Lazzarin A. Campagnolo, F. Berto. The effects of different boundary conditions on three-dimensional cracked discs under anti-plane loading. *European Journal of Mechanics, A/Solids*, 50:76–86, 2015. ISSN 09977538. doi: 10.1016/j.euromechsol.2014.11.001. URL http://dx.doi.org/10.1016/j.euromechsol.2014.11.001.

[55] F. Berto A. Campagnolo and L. P. Pook. Three-dimensional effects on cracked discs and plates under nominal Mode III loading. *Frattura ed Integrita Strutturale*, 9(34): 190–199, 2015. ISSN 19718993. doi: 10.3221/IGF-ESIS.34.20.

[56] F. Berto A. Kotousov, P. Lazzarin and S. Harding. Effect of the thickness on elastic deformation and quasi-brittle fracture of plate components. *Engineering Fracture Mechanics*, 77(11):1665–1681, 2010. ISSN 00137944. doi: 10.1016/j.engfracmech.2010.04.008. URL http://dx.doi.org/10.1016/j.engfracmech.2010.04.008.

[57] P. Lazzarin A. Kotousov, F. Berto and F. Pegorin. Three dimensional finite element mixed fracture mode under anti-plane loading of a crack. *Theoretical and Applied Fracture Mechanics*, 62(1):26–33, 2012. ISSN 01678442. doi: 10.1016/j.tafmec.2013.01.003. URL http://dx.doi.org/10.1016/j.tafmec.2013.01.003.

[58] F. Berto A. Kotousov, P. Lazzarin and L.P. Pook. Three-dimensional stress states at crack tip induced by shear and anti-plane loading. *Engineering Fracture Mechanics*, 108:65–74, 2013. ISSN 00137944. doi: 10.1016/j.engfracmech.2013.04.010. URL http://dx.doi.org/10.1016/j.engfracmech.2013.04.010.

[59] W. Wang Y. Wang, B. Zhang, and CQ. Li. A review on mixed mode fracture of metals. *Engineering Fracture Mechanics*, pages 1–2, 2020. doi: https://doi.org/10.1016/j.engfracmech.2020.107126.

[60] B. Saboori M.R. Ayatollahi. A new fixture for fracture tests under mixed mode I-III loading. *European Journal of Mechanics-A/Solids*, pages 67–76, 2015. doi: https://doi.org/10.1016/j.euromechsol.2014.09.012.

[61] B. Saboori M.R. Ayatollahi. A novel test configuration designed for investigating mixed mode II/III fracture. *Engineering Fracture Mechanics*, pages 248–258, 2018. doi: https://doi.org/10.1016/j.engfracmech.2018.04.048.

[62] A. Eberlein H.A. Richard. Experiments on cracks under spatial loading. *ICF132013*, 2013.

[63] M. Kuna H.A. Richard. Theoretical and experimental study of superimposed fracture modes I, II and III. *Engineering Fracture Mechanics*, pages 949–960, 1990. doi: https://doi.org/10.1016/0013-7944(90)90124-Y.

[64] Y. Mutoh J. Chang, J. Xu. A general mixed-mode brittle fracture criterion for cracked materials. *Engineering Fracture Mechanics*, pages 1249–1263, 2006. doi: https://doi.org/10.1016/j.engfracmech.2005.12.011.

[65] B.D. Davidson M.W. Czbaj, J.G. Ratcliffe. Observation of intralaminar cracking in the edge crack torsion specimen. *Engineering Fracture Mechanics*, pages 120–124, 2014.

[66] B.D. Davidson A.L. Horner, M.W. Czabaj and J.G. Ratcliffe. Three-dimensional crack surface evolution in mode III delamination toughness tests. *Engineering Fracture Mechanics*, pages 313–325, 2015.

[67] B.D. Davidson A.L. Horner. Fracture surface evolution and apparent delamination toughness in split composite beam specimens subjected to mixed mode I-III loading. *Composites Part A: Applied Science and Manufacturing*, pages 92–102, 2015.

[68] P. Sabbadin, C. Berggreen, and B.N. Legarth. Development of a mode i/ii/iii test fixture for composite laminates and sandwich face/core fracture characterization. *Proceedings of 12th International Conference on Sandwich Structures*, 1(1):35–37, 2018. doi: -.

[69] R.M. Jones. Mechanics of composite materials. *Taylor and Francis*, 1999.

[70] ASTM. Standard Test Method for Tensile Properties of Polymer Matrix Composite Materials. *D3039/D3039M-17*, pages 1–13, .

[71] ASTM. Standard Test Method for Shear Properties of Composite Materials by V-Notched Rail Shear Method. *D7078/D7078M-12*, pages 1–15, .

[72] ASTM. Standard test Method for Shear Properties of Composite Materials by the V-Notched Beam Method. *D5379/D5379M-12*, pages 1–14, .

[73] R. Pipes D. Adams, L. Carlsson. Experimental Characterization of Advance Composite Materials. *CRC Press*, pages 87–96, 2003.

[74] Diab. Divinycell H technical data sheet. pages 1–2, 2018.

[75] Dassault Systems. Abaqus online manual. 2018.

[76] C. Berggreen. Damage tolerance of debonded sandwich structures. *PhD Thesis*, pages 7–21, 2004.

[77] J.P. Benthem. State of stress at the vertex of a quarter-infinite crack in a half-space. *Int. J. Solids Structures*, 13(-):479–492, 1977. doi: -.

[78] Z. Bazant and L.F Estenssoro. Surface singularity and crack propagation. *Int. J. Solids Structures*, 15(-):405–426, 1979. doi: -.

[79] ASTM. Standard Test Method for Ignition Loss of Cured Reinforced Resins. *D2584-18*, pages 1–3, .

[80] ASTM. Mixed Mode I-Mode II Interlaminar Fracture Toughness of Unidirectional Fiber Reinforced Polymer Matrix Composites. *D6671/D6671M-06*, pages 1–13, .

[81] Kim Branner. Capacity and Lifetime of Foam Core Sandwich Structures. pages 65–68, 1995.

[82] A. Arnesen Y. Rothschild, A.T. Echtermeyer. Modelling of the non-linear material behaviour of cellular sandwich foam core. pages 111–118, 1993.

7. APPENDIX A

Appended Publications

[P1] An improved analysis of a STB specimen for fracture characterization of laminates and foam-cored sandwich composites under mode III loads. *Published June 2020, Engineering Fracture Mechanics.*

[P2] A novel test fixture for mode III fracture characterization of monolithic laminates and composite sandwich specimens. *Submitted to Journal of Composite Materials.*

[C1] Development of a Data Reduction Method for Composite Fracture Characterization Under Mode III Loadings. *Published in Springer Nature, AIMETA 2019 LNME proceedings.*

[P1]
An improved analysis of a STB specimen for fracture characterization of laminates and foam-cored sandwich composites under mode III loads.

8. Paper 1
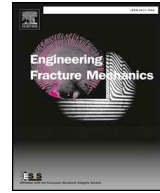
An improved analysis of a STB specimen for fracture characterization of laminates and foam-cored sandwich composites under mode III loads

Pietro Sabbadin[a], R. Massabó[b], C. Berggreen[c],*

[a] Department of Mechanical Engineering, Technical University of Denmark, Niels Koppels Alle, Building 404, Kgs. Lyngby, Denmark
[b] Department of Civil, Chemical and Environmental Engineering, University of Genova, Genova, Italy
[c] Department of Mechanical Engineering, Technical University of Denmark, Denmark

A B S T R A C T

This work presents the development of an improved data reduction method for the shear-torsion-bending (STB) test designed for monolithic laminates. The analytical derivation extends the applicability of the STB rig to composite sandwich specimens subjected to an out-of-plane shear loading. The data reduction method consists of an analytical model that expresses the global energy release rate in terms of applied loads, specimen geometry and material properties. The mathematical derivation of the energy release rate relies on first order shear deformation theory, Vlasov theory for non-uniform torsion of beams and near tip effects are also taken into consideration by the analytical model. Face sheets and core are modelled as homogeneous, linear elastic and orthotropic materials. The analytical expression is verified using the energy release rate extracted from a high-fidelity 3D FE based fracture mechanics model of the specimen. A compliance based method is used to generate global predictions, while local predictions are extracted using a displacement-based mode separation method. Local predictions are used to discuss accuracy and limitations of the approximate analytical model.

1. Introduction

Laminates and sandwich composites are used to build many structural components in naval vessels. Sandwich composites are often used for lightweight structural applications because of their superior stiffness/weight and strength/weight ratios compared to metallic materials such as steel.

The types of failure associated with composite sandwich materials have to be understood accurately, if structural components have to be robust throughout their in-service life-time. The most common types of damages a sandwich structure can encounter are [1–3]: face-core interface debonding, core indentation, core-shear failure, face wrinkling and dimpling, shear crimping and general buckling. The functionality and load-carrying capacity of a structural component can be severely compromised by one of the aforementioned damages.

Face-core interface debonding is the damage considered in the analyses carried out in this work. The term *debond* addresses a lack of adhesion between one of the face sheets and core. Debonding may result in in-service collapses such as: the structural failure of an airplane rudder [3], of a fuel tank in the aerospace sector [4] and of wind turbine blades under cyclic loadings [5]. Therefore, the

Nomenclature

Latin Symbols

a	crack length
b	specimen width
E_f	Young modulus of the face sheet in the Z-direction
E_c	Young modulus of the core in the Z-direction
G_f	elastic shear modulus of the face sheet in the ZY-plane
G_c	elastic shear modulus of the core in the ZY-plane
G	energy release rate
h	height of the load tabs
k_r^d	stiffness of the rotational spring placed at the right-hand side of the upper delaminated arm
k_r^s	stiffness of the rotational spring placed at the right-hand side of the lower delaminated arm
k_t^d	stiffness of the linear spring placed at the right-hand side of the upper delaminated arm
k_t^s	stiffness of the linear spring placed at the right-hand side of the lower delaminated arm
L	total specimen length
M_Z^{Rd}	reaction moment acting on the upper load tab in the Z-direction
M_Z^{Rs}	reaction moment acting on the lower load tab in the Z-direction
M_Z^d	moment acting on the upper delaminated arm (delaminated part) along the Z-axis
M_Z^s	moment acting on the lower delaminated arm (substrate part) along the Z-axis
$M_X(X)$	moment acting on the upper and lower delaminated arms along the X-axis
$M_x^d(z)$	moment acting along the x-axis on the upper delaminated arm at coordinate z
$M_x^s(z)$	moment acting along the x-axis on the lower delaminated arm at coordinate z
$M_z^i(z)$	moment along the z-axis acting on a delaminated arm at coordinate z
P	external load

P^R	reaction force acting on the upper load tab in the Y-direction
t_f	face sheet thickness
t_c	core thickness
$u_y^d(z)$	displacement of the shear center axis along the y-direction of the upper delaminated arm at co-ordinate z
$u_y^s(z)$	displacement of the shear center axis along the y-direction of the lower delaminated arm at co-ordinate z
$V_y^d(z)$	shear force acting along the y-axis on the upper delaminated arm at coordinate z
$V_y^s(z)$	shear force acting along the y-axis on the lower delaminated arm at coordinate z
W	width of the bonded part of the specimen
X, Y, Z	axes labels of coordinate reference system for the specimen
x, y, z	axes labels of coordinate reference system for the structural model

Greek Symbols

κ_d	shear correction factor for the upper beam
κ_s	shear correction factor for the lower beam
$\varphi_d(z)$	rotation of the section of the upper delaminated arm around the x-axis at the coordinate z
$\varphi_s(z)$	rotation of the section of the lower delaminated arm around the x-axis at the coordinate z
θ_z^i	angle of twist along the z-axis of a beam section
$(E\Gamma)_i$	warping stiffness of a delaminated arm sections

Indexes

c, f	indices to indicate the face sheet and the core
d, s	indices for delaminated (upper beam) and sub-strate (lower beam)
LAM, SAN	indices referring either to the monolithic lami-nate or the sandwich

face-core interface must be characterized in order to provide a reliable assessment of the damage tolerance and robustness of a structural component.

The energy required to separate a unit area of the face sheet from the core is called fracture toughness and is the physical quantity used to assess the bonding strength of an interface. Several studies on sandwich composites (see review in [6]) observed that the fracture toughness depends on the local value of the mode-mixity between the different fracture modes at the debond tip. In particular, the work presented in [5] shows how out-of-plane shear loads, which induce a dominant mode III stress state along the

(a) ECT specimen.   (b) MSCB specimen.   (c) STB specimen.
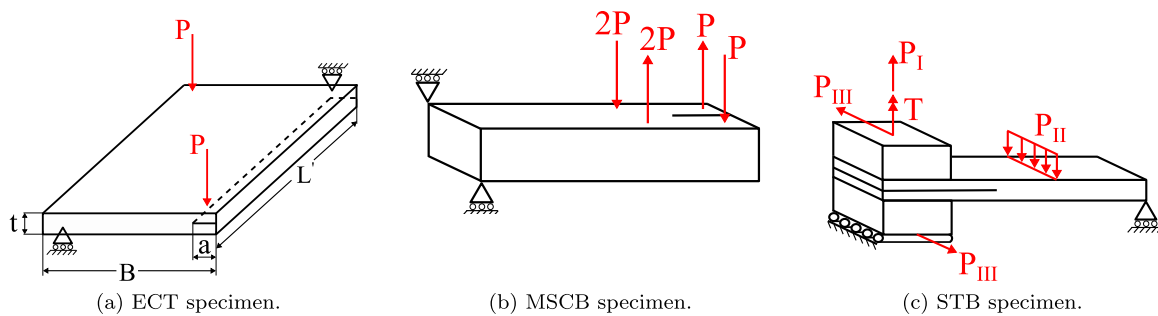
Fig. 1. Test rigs designed to perform fracture characterization tests under out-of-plane shear loadings.

debond front between the face and the core, can be detrimental for the structural integrity of a wind turbine blade component made of sandwich composites. Furthermore, several studies [7–14] have been carried out to measure the fracture toughness of monolithic composite laminates, when the debond front is under out-of-plane shear. The term out-of-plane refers to Mode III (out of plane shear or tearing) crack sliding displacements which occur over most of the crack front in the specimens.

Different experimental methods (see Fig. 1) have been developed to measure the value of the interface fracture toughness G_c under out-of-plane shear stress conditions in monolithic laminates. The experimental results include: the edge crack torsion test (ECT) [7], the modified split cantilever beam (MSCB) test [8] and the shear torsion bending (STB) [9] test. The ECT test consists of a delaminated plate subjected to a twisting moment, which results in a distribution of out-of-plane shear stresses along the debonded front. The MSCB test is on a cracked specimen with a beam-like geometry. In this test, two transverse forces are applied on the delaminated arms in order to produce out-of-plane stresses along the crack front. Similarly to the MSCB test, the STB test [9] includes a pre-delaminated specimen with a beam-like geometry. The issue with ECT, MSCB and STB tests is the lack of uniformity in the stress field along the crack front, which differs from the anti-plane field. One of the causes of the non-uniformity in the local stress field is the presence of stress-free lateral edges in the specimen.

An anti-plane stress/displacement field is the third type of elastic problem which is usually solved in 3D linear elasticity along with the plane-stress and plane-strain problems. A closed-form solution of the anti-plane stress/displacement local field for an interface crack between two dissimilar anisotropic media is provided by Suo in [15]. Likewise plane strain and plane stress states, the anti-plane state requires that the local stress/displacement field repeats itself in a self-similar manner on all the planes orthogonal to the out-of-plane direction. Hence, the presence of a continuous crack front is necessary in order to satisfy pure anti-plane conditions. Traction-free edges, which are present in every beam-like specimen for fracture characterization, are a feature that breaks the continuity of the crack front. The stress/displacement field changes abruptly to satisfy the traction-free boundary conditions. This zone of transition can be considered as a boundary layer. The characteristics of this boundary layer have been studied in analytical and numerical studies by Benthem, Dhondt, Sih and Fenner [16–19]. The singularity of the stress field changes when a traction-free edge is approached as studied analytically in [16] and numerically by Nakamura in [20,21]. The equations derived by Suo in [15] do not describe the local stress/displacement fields present in the aforementioned boundary layer, where neither plane strain nor plane stress or anti-plane conditions exist. Therefore, the analytical closed-form solutions presented in [15] cannot be used at the specimen free-edges.

Additional complexity is added to the problem by the fact that mode-II and mode-III fields are coupled at the specimen free edges. Several studies [22–29] show how, when a crack edge meets a traction-free surface, a coupling arises between in-plane shear deformations and out-of-plane shear deformations. This phenomenon can be detected and has been analysed in [22–29] using FE model.

The discontinuity of the crack front and its intersection with a traction-free surface leads to a 3D local stress field in the boundary layer. This fact implies that the local values of the energy release rate along the crack front are not constant. The energy release rate shows a peculiar local trend when the boundary layer in the vicinity of the traction-free edge is approached. These results have been presented in [25,26], where a pure anti-plane stress field is applied on the boundary of a cracked disc. The disc is made of a linear elastic and homogeneous material. The local value of the out-of-plane stresses decreases from the centre of the disc to the traction-free edge and then vanishes at the free-edge to satisfy equilibrium condition at the free surface. Instead, the local value of the in-plane shear stresses increases from zero to a finite value where the crack front meets the free edge. Since the local stresses are proportional to stress intensity factors, and the energy release rate is proportional to the square of the stress intensity factors, then the local value of G is not constant along the crack front (see Fig. 2).

- - - Anti-plane G distribution
—— Real G distribution
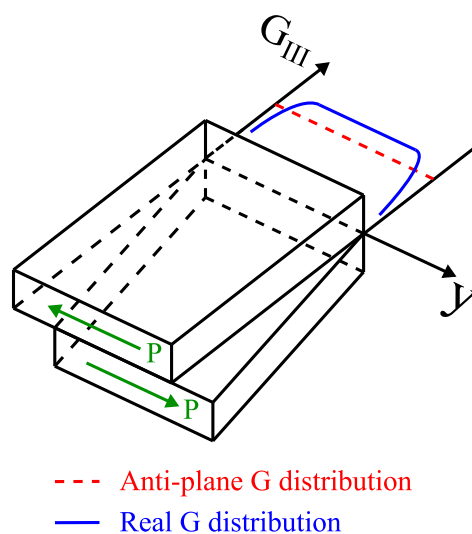
Fig. 2. Qualitative representation of the local energy release rate values in a specimen that presents traction-free edges and subjected to out-of-plane loadings.

The phenomena described above are emphasized in the case of an interface crack where the elastic mismatch intensifies the coupling between in-plane and out-of-plane shear stresses, with respect to the case of a crack in a homogeneous material. Hence, a homogeneous distribution of the energy release rate in a cracked bi-material beam-like specimen subjected to out-of-plane shear loadings is not admissible. Moreover, the stress state in the boundary layer in the vicinity of the traction-free edge is always mixed-mode II-III. If the crack starts to propagate in the region close to the traction free edges, the fracture toughness related to that propagation corresponds to a certain mode-mixity between mode-II and mode-III, even if the macroscopic external loading consists in pure out-of-plane shear forces.

Hence, the fracture toughness measured using beam-like specimens is always associated with a certain mode-mixity between mode II and III. In the Shear-Torsion-Bending test [9], the specimen is loaded using two stiff load blocks attached at the end of the two delaminated arms, which can slide preventing rotations of the arms. These loading conditions (along with two longitudinal side notches ahead of the crack front) favor the most uniform distribution of out-of-plane shear stresses along the crack front and therefore more uniform mode III conditions compared with the ECT and MSCB tests. For this reason, the STB test [9] is chosen as the reference test in order to develop the new data reduction method presented in this work. The STB test rig is also capable to apply mode-I and mode-II loads, but only the mode-III configuration is analysed here. Data reduction methods for mode I-II-III have been presented and discussed in [9] and accurate 2D solutions can be defined for mode-I and II using the derivations in [30,31].

Recent experimental studies [32–34] on unidirectional laminates subjected to mode III conditions show that the delamination crack advance is preceded by the formation of intra-laminar cracks. These intra-laminar cracks grow out of the main delamination plane in the matrix. The propagation of intra-laminar cracks is controlled by the fiber orientation in the laminae adjacent to the delamination and the presence of this energy dissipating mechanism is responsible for an R-curve behaviour and the apparent fracture toughness measured in the tests performed in [32–34].

The data reduction method for mode-III loading developed in [9] is applicable only to monolithic laminates, does not take into account the intra-laminar cracks and has been derived for a specific specimen geometry and a fixed crack length. The equation of the energy release rate in [9] presents some global coefficients, which are calibrated numerically. These coefficients globally account for effects related to crack near tip deformations, shear deformations and stress decay in the intact and traction-free part of the specimen.

The new data reduction method presented in this work is inspired to the work in [8] and responds to the need for reducing measured force and moment data to energy release rate using a novel test rig presented in [35] (inspired to STB [9]). The analytical model presented in this work uses linear elastic fracture mechanics and assumes that the delamination crack propagates along its original plane and that no other damage mechanisms are present in the specimen. Thus, the possible presence of intra-laminar cracks is not taken into account by the current model. The assumptions will require experimental validation. In the novel test rig, an out-of-plane shear load is applied to a pre-debonded sandwich specimen in order to propagate the debond, as shown in Fig. 3. The parameters measured during the test, using an axial–torsional load cell are: the applied total force P and the reaction moments $M_X^R(Z = -a)$ about the *x*-axis on the load tabs (see Fig. 4b). An expression of the energy release rate that takes into account the geometry, the specimen material system and the load set applied is required to size correctly the specimen and to compute the fracture toughness G_c from experimental results. In this paper, a closed-form derivation of the energy release rate for a sandwich specimen is presented. Then, the solution for composite sandwich is particularized for a monolithic laminate.
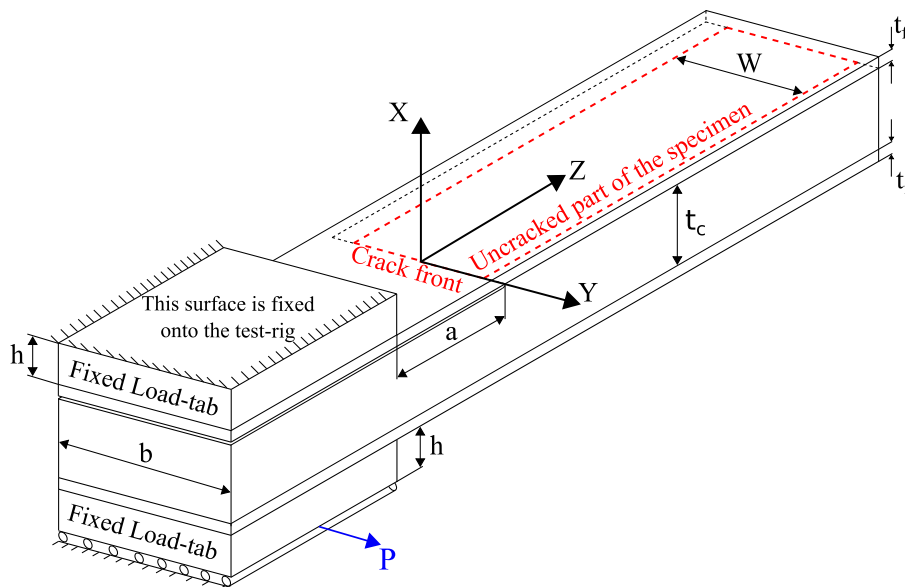
Fig. 3. Representation of the specimen with its geometrical parameters and the applied load P.
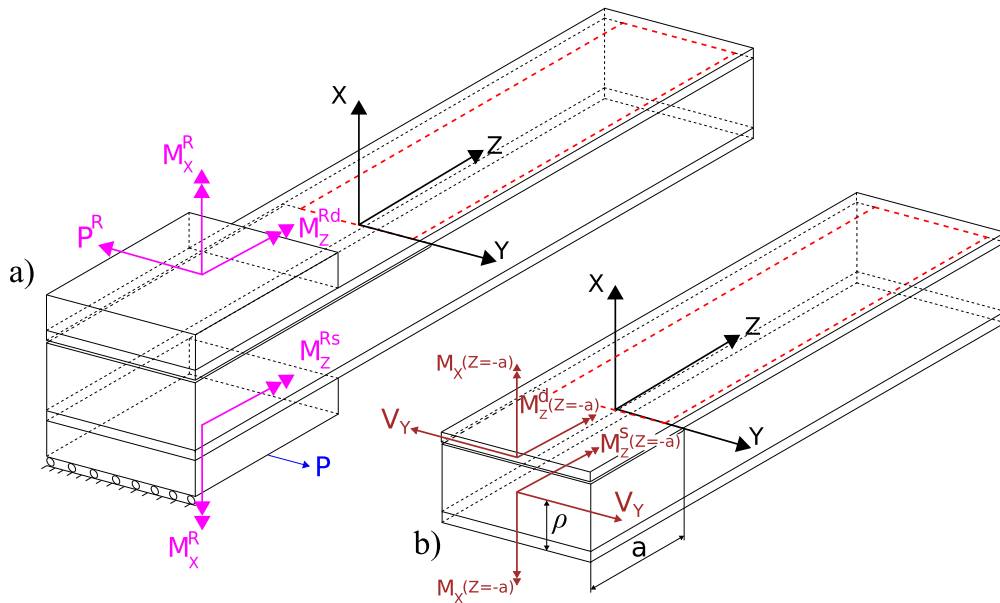
Fig. 4. (a) Specimen with load tabs and reaction loads, (b) loads acting at the shear center of each debonded arm.

2. Method

2.1. Specimen geometry, materials and loads

The specimen is presented with the main geometrical parameters in Fig. 3. Two steel load tabs are attached to the delaminated part of a sandwich specimen. Two different specimen widths are considered as it is shown in Fig. 3: b is the width of the delaminated part of the specimen and W is the width of the intact interface ahead of the crack front, where two longitudinal cuts have been introduced. W is the geometrical parameter, which defines the fracture surface where the crack propagates.

The two face sheets have the same thickness t_f and the core thickness is t_c. The crack length a is the distance between the end of the load tab and the crack tip. h is the height of each load-tab. The geometrical values considered in this work are summarized in Table 1.

Table 1
Main geometrical parameters, all lenghts are expressed in mm.

	t_f	t_c	a	b	W	L	L_{tab}	h
Laminate	2	–	40	30	26	160	60	10
Sandwich	2	20	40	40	24	160	60	10

Moreover, the index d is used to indicate the upper delaminated face sheet and the index s is utilized to denote all the parameters related to the lower substrate (made of the core and lower face sheet).

Two types of specimens are studied: a glass fiber monolithic laminate and a foam-cored sandwich. The laminate and face sheets of the sandwich specimen are modelled as linear elastic, homogeneous and orthotropic materials whose equivalent elastic properties are reported in Table 2. The core is modelled as linear elastic, homogeneous and orthotropic material. The case studied uses the properties in Table 3 that are representative of a PVC foam considered as isotropic. The upper delaminated arm consists of a beam having a homogeneous cross-section, and the lower arm has an in-homogeneous cross-section composed of two different materials: the core and the face sheet. The $X − Y − Z$ axes are coincident with the principal material directions for both face sheets and core. Each XY-plane is a plane of elastic symmetry, so that torsional moments (acting along the Z-axis) are not coupled with bending moments acting along X-Y axes. Consequently, orthotropic face sheets that comply with the aforementioned requirements can be either unidirectional or cross-ply (see [36]). The properties in Tables 2 and 3 describe a monolithic laminate and sandwich face-sheets having a lay-up of Devold® glass fiber fabric infused with the Pro-Set® INF-114 epoxy resin. Instead, the core consists in a open-cell PVC foam core of class H100 manufactured by Diab®. The monolithic laminate specimen has the following lay-up $[(0/45/90/−45)_{2S}||]_S$, where the symbol "||" designates the location of the Teflon insert. Instead, the lay-up sequence of each sandwich face-sheet is $[(0/45/90/−45)_2]_S$. Hence, the delaminated arms of the monolithic laminate and the face-sheets of the sandwich specimen are symmetric and balanced laminates. The material properties of the laminate and sandwich face sheets are measured from mechanical tests following ASTM standards [37–39]. Tensile tests to measure E_{ZZ}, E_{YY} and ν_{YZ} were conducted according to [37]. The

V-Notched Rail Shear Method [38] was employed to measure the in-plane elastic shear modulus G_{YZ}. Instead, the elastic shear moduli G_{XZ} and G_{XY} are evaluated using Iosipescu shear test [39]. No ASTM standards are available for measurement of E_{XX}, ν_{XY} and ν_{XZ} for a FRP laminate. Nevertheless, a test method suggested in [40] was adopted to measure E_{XX}, ν_{XY} and ν_{XZ}. Test specimen having dimensions of $15 \times 15 \times 30$ (mm) were inserted between two compressive platens. Digital image correlation (DIC) Aramis® system was used to monitor the strains on the specimen sides. Material properties for the PVC foam core were taken from the manufacturer catalogue [41] and the load tabs are made of C40 structural steel.

Table 2
Laminate material properties measured experimentally with their coefficient of variation, see Fig. 3 for axes directions.

Material	Elastic Moduli [GPa]						Poisson ratios		
	E_{XX}	E_{YY}	$E_{ZZ} = E_f$	G_{XY}	G_{XZ}	$G_{YZ} = G_f$	ν_{XY}	ν_{XZ}	ν_{YZ}
Face sheet	9.5	19.8	19.8	2.9	2.9	7.5	0.43	0.37	0.32
CV [%]	10.5	3.3	5.0	7.8	7.8	1.7	13.5	10.1	1.3

Table 3
Core and load tab material properties.

Material	Elastic Moduli [GPa]						Poisson ratios		
	E_{XX}	E_{YY}	$E_{ZZ} = E_c$	G_{XY}	G_{XZ}	$G_{YZ} = G_c$	ν_{XY}	ν_{XZ}	ν_{YZ}
Core	0.095	0.095	0.095	0.035	0.035	0.035	0.4	0.4	0.4
Load-Tabs	200	200	200	77	77	77	0.3	0.3	0.3

The following notation is used in all the following equations: E_f and E_c denote the longitudinal elastic moduli E_{ZZ} of the face sheets and core, while G_f and G_c refer to the elastic shear moduli of face and core in the YZ-plane.

Fig. 4 shows loads and reaction forces on the load tabs and loads transferred to each debonded arm of the sandwich composite. The lower-tab surface can only translate in the Y-direction, while points on the upper-tab surface are fixed. The load tabs prevent rotations and torsional warping of the arm cross section located at $Z = -a$. The intact part of the specimen is traction free and it follows rigidly the displacements/rotations of the debonded arms.

The only external load is the load P and it is applied on the lower load tab. A reaction force P^R arises in the upper load-tab, parallel to the Y-axis, which is equal and opposite to P in order to satisfy equilibrium. Two different reaction moments M_Z^{Rd} and M_Z^{Rs} set in parallel with the Z-axis on the surface of each load tab, since rotations around the Z-axis are not permitted. Moreover, reaction moments around the X-axis (M_X^R) arise on each load tab, since rotations of the specimen around the X-axis are locked.

The loads are transferred from the load tabs to each cross-section shear center in the specimen. As shown in Fig. 4b, the loads consist of two out-of-plane shear forces $V_Y = P$ equal and opposite in each debonded arm, two moments M_Z^d and M_Z^s acting on the upper and lower delaminated arms at $Z = -a$ and a moment $M_X(Z = -a)$ acting on both debonded arms. Where the two delaminated arms join, at the crack front (see Fig. 5), internal moments and forces must constitute an auto-equilibrated system since the intact part of the specimen is traction-free. The value of the two internal moments $M_X(Z = 0)$ have opposite directions and same magnitude. The two shear forces $V_Y = P$ generate a resultant moment in the Z-direction which equilibrate the sum of the two moments $M_Z^d(Z = 0) + M_Z^s(Z = 0)$.

The shear center of the upper debonded arm is the geometrical centroid of the face sheet cross section. The lower debonded arm presents a rectangular cross-section composed by two materials having different elastic properties. Classical laminate theory (CLT) is used in order to find the position of the shear center of the bi-material cross section. The reference plane chosen is the middle plane of the substrate. CLT defines the distance e of the shear center respect to the middle plane as $e = -(b_{66}/d_{66})$, where b_{66} and d_{66} are the
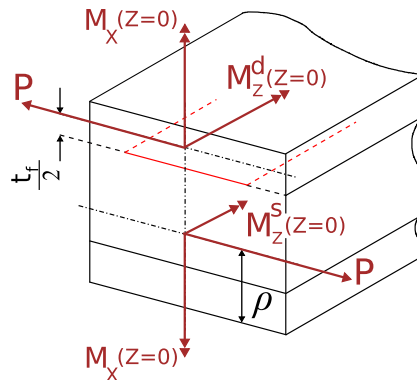
Fig. 5. Close view of the auto-equilibrated internal force set at crack front ($Z = 0$), where the two debonded arms join.

components of the inverse ABD matrix. In this way, the distances e and ρ are expressed in terms of the geometry and material properties of the cross section (Fig. 6):

$$e = \frac{t_c t_f (G_f - G_c)}{2(G_c t_c + G_f t_f)} \tag{1}$$

$$\rho = \frac{t_f + t_c}{2} - e. \tag{2}$$

2.2. Structural model of the sandwich specimen

A new coordinate system $x - y - z$ is introduced in Fig. 7 with origin at $Z = -a$. The schematics in Fig. 7a–b are used to analyse the in-plane (a) and torsional (b) response of the upper and lower delaminated arms.

The two debonded arms of length a in Fig. 7 are modelled as shear deformable beams in order to analyze the contributions to the energy release rate resulting from the external applied load P, the internal bending moment $M_x(z)$ and shear force V_y. The beam left end is clamped with free sliding, while the right end rotations and transverse displacements are controlled by two elastic springs. The elastic springs are introduced to account for the deformation of the material ahead of the crack front and will be described in the next section.

The torsional contribution to the energy release rate is studied separately using the structural scheme represented in Fig. 7b: the left end of the beam is torsionally clamped by the load tab, while the right end is considered free to warp and subjected to the moment $M_z^i(z = a)$. $M_z^i(z = a)$ is not an external load and represents the internal torsional moment that satisfies the rotational equilibrium at the crack front cross-section. Therefore $M_z^s(z = a)$ and $M_z^d(z = a)$ are the internal torsional moments that come from the upper and lower delaminated beam respectively. Simple equilibrium considerations relate the internal torsional moments and the reaction forces:

$$\begin{cases} M_z^s(z = a) = V_y A - M_z^d(z = 0) \\ M_z^d(z = a) = V_y A - M_z^s(z = 0) \end{cases} \tag{3}$$

where $A = t_c + t_f/2 - \rho$ is the distance between the shear centres of the beams. The torsional reaction forces in Eq. (3) are defined as functions of the applied load P, by imposing compatibility on the torsional angles at the crack front sections, see Appendix A, in Eqs. 74.

2.3. In-plane problem

The bending and shear stiffnesses of the substrate are expressed through equivalent quantities $(EI)_s$ and $(GA)_s$ using the following relationships:

$$(EI)_s = E_f I_f + E_c I_c \tag{4}$$

$$(GA)_s = (G_f A_f + G_c A_c) \kappa_s \tag{5}$$

where I_f and I_c are the second moment area of the face and core cross sections about the x-axis, A_f and A_c are the areas of the face and core cross sections and κ_s is a shear correction factor given in Eq. 43 (see appendix A for the derivation of κ_s). The upper arm has a bending stiffness $E_f I_f$ and shear stiffness $G_f A_f \kappa_d$, where κ_d is the shear correction factor. The two elastic springs of stiffnesses k_r^i and k_t^i (with $i = d, s$) describe the compliance of the material ahead of the crack front, through a structural mechanics approximation.

The translational spring of stiffness k_t^i mimics the shear deformations of the material ahead of the crack front in the xy-plane (see Figs. 16 and 17). The values of k_t are calculated for the delaminated and subtrate parts using the procedure shown in the Appendix A. The following equations present k_t^d and k_t^s, with $G_{xy} = G_{XY}$:
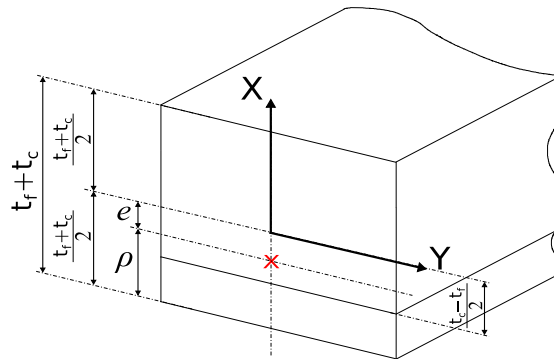
× Bi-material beam shear center

Fig. 6. Scheme used to find the shear center of the bi-material cross-section.

(a) In plane loads.

(b) Torsional loads.
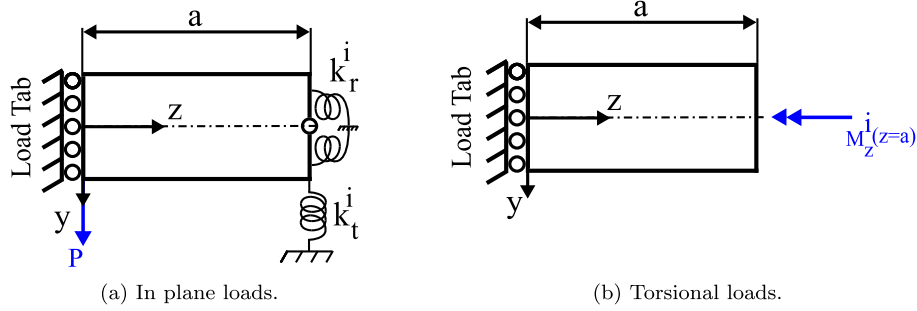
Fig. 7. a) Structural scheme used to analyse the in plane loads, b) structural scheme used to analyze the torsion problem on each beam. The index $i = d, s$.

$$k_t^s = \frac{G_{xy} A_f G_c A_c}{G_c A_c (t_f - \rho) + G_{xy} A_f t_c}. \tag{6}$$

$$k_t^d = \frac{2 G_{xy} A_f}{t_f}. \tag{7}$$

The values of the elastic constants k_r^d and k_r^s of the rotational springs are deduced using the reaction moments at the load tabs, the external load P measured in the experiments and Eqs. (50), (54):

$$k_r^d = \frac{2 P a E_f I_f - 2 M_x^d (z = 0) E_f I_f}{2 M_x^d (z = 0) a - P a^2} \tag{8}$$

$$k_r^s = \frac{2 P a (EI)_s - 2 M_x^s (z = 0)(EI)_s}{2 M_x^s (z = 0) a - P a^2}. \tag{9}$$

In the applications presented in this paper the constants will be defined using a finite element model of the specimen which simulates the experimental test. An analytical expression for k_r will be defined in Section 3.6 for the monolithic laminate.

The differential equations for a shear deformable beam are:

$$\begin{cases} (EI)_s \varphi_s'''(z) = 0 \\ (EI)_s \varphi_s''(z) = (GA)_s ((u_y^s(z))' + \varphi_s(z)) \end{cases} \tag{10}$$

where $\varphi_s(z)$ is the rotation about the x-axis and $u_y^s(z)$ is the displacement in the y-direction of the beam axis. The bending moment $M_x^s(z)$ and out-of-plane shear $V_y^s(z)$ are related to the generalized displacements by the constitutive equations:

$$M_x^s(z) = (EI)_s \varphi_s'(z) \tag{11}$$

$$V_y^s(z) = (GA)_s ((u_y^s(z))' + \varphi_s(z)) \tag{12}$$

The following boundary conditions are applied:

$$\varphi_s(z = 0) = 0 \tag{13}$$

$$V_y^s(z = 0) = -P \tag{14}$$

$$\varphi_s(z = a) = -\frac{M_x^s(z = a)}{k_r^s} = -\frac{(EI)_s \varphi_s'(z = a)}{k_r^s} \tag{15}$$

$$u_y^s(z = a) = -\frac{V_y^s(z = a)}{k_t^s} = -\frac{(GA)_s}{k_t^s} ((u_y^s(z))' + \varphi_s(z)). \tag{16}$$

Solving Eqs. (10), together with the boundary conditions (13)–(16), the analytical expressions for $M_x^s(z)$, $V_y^s(z)$, $\varphi_s(z)$ and $u_y^s(z)$ for the lower debonded arm are found in closed form (see appendix A, Eqs. (50)–(53)). The equations for the upper arm have a similar analytical form of Eqs. 50,51,52,53, (see appendix A, Eqs. (54)–(57)).

2.4. Torsional problem

The torsional problem in Fig. 7b is analyzed using Vlasov theory [42] for non-uniform torsion of beams having open and thin-walled sections, since the left beam-ends are not free to warp. The hypothesis of open and thin-walled section is satisfied by the delaminated part, since the ratio $b/t_f = 15$. The substrate part can also be studied as an open thin-walled section, because of the large mismatch between the elastic shear moduli of face sheet and core of typical foam core sandwich. This implies that the internal

torsional stresses τ_{zx} and τ_{zy} concentrate mainly in the lower face sheet as it is shown in the FE results (see Fig. 18 in appendix A). Therefore, the torsional structural response of the substrate is governed by the lower face sheet.

The problem of non-uniform torsion is described by the following differential equation which is applied to both upper and lower delaminated arms:

$$(\theta_z^i)''' - c_i^2(\theta_z^i)'' = 0, \quad i = d, s \tag{17}$$

where $\theta_z^i(z)$ is the angle of twist about the z-axis and c_s and c_d:

$$c_d = \sqrt{\frac{D_d}{(E\Gamma)_d}} \tag{18}$$

$$c_s = \sqrt{\frac{D_s}{(E\Gamma)_s}} \tag{19}$$

where D_d and D_s are the torsional rigidities. Equivalently, $(E\Gamma)_d$ and $(E\Gamma)_s$ are the warping rigidities and they are defined in Appendix A.

The internal torque moments $M_z^i(z)$ are related to $\theta_z^i(z)$ by the constitutive equation:

$$(\theta_z^i)''' - c_i^2(\theta_z^i)' = \frac{M_z^i(z)}{(E\Gamma)_i}, \quad i = d, s. \tag{20}$$

The closed form solution for the torsional problem is found applying the following boundary conditions (valid for both delaminated arms) to Eq. (17) and using Eq. (20):

$$\begin{cases} \theta_z^i(z=0) = 0 \\ (\theta_z^i)'(z=0) = 0 \\ (\theta_z^i)''(z=a) = 0 \\ \theta_z^d(z=a) = \theta_z^s(z=a) \end{cases} \tag{21}$$

The differential equations describing the torsional behaviour of the two delaminated beams are coupled. The coupling kinematic condition is given at the crack front beam section at $z = a$ where $\theta_z^d(z=a) = \theta_z^s(z=a)$ is imposed between the twist angles of the delaminated and substrate part. The boundary condition $(\theta_z^i)'(z=0) = 0$ implies that the axial displacements in the z-direction of all points of the cross section at $z = 0$ are zero [42]. The boundary condition $(\theta_z^i)''(z=a) = 0$ implies that at $z = a$ the secondary normal stresses, induced by preventing the section warping, are zero [42].

The solution of the torsional problem is:

$$\theta_z^i(z) = \frac{M_z^i(z=a)a}{D_i}\mu_i(z), \ \mu_i(z) = \frac{z}{a} - \frac{e^{c_iz} + e^{2c_ia}(1 - e^{-c_iz}) - 1}{ac_i(1 + e^{2c_ia})} \quad i = d, s \tag{22}$$

where $M_z(z=a)$ is given in Eq. (74) and $\mu_i(z)$ is a correction factor for the classical De Saint Venant solution, where restrained warping is not accounted. The $\mu_i(z)$ factor becomes equal to 1 when the solution converges to the uniform torsion case.

2.5. Energy release rate calculation for the sandwich configuration

The energy release rate, for the uniform propagation of the crack front, is calculated from the total potential energy Π of the system:

$$\Pi = U_{tot} - L_{ext} \tag{23}$$

where $U_{tot} = U_d + U_s$. Each beam gives four contributions: the energies due to bending, out-of-plane shear, torsion and the elastic energy stored in the linear elastic springs:

$$\begin{cases} U_d = U_{bending}^d + U_{shear}^d + U_{torsion}^d + U_r^d + U_t^d \\ U_{bending}^d = \int_0^a \frac{(M_x^d(z))^2}{2E_fI_f}dz \\ U_{shear}^d = \int_0^a \frac{(V_y(z))^2}{2G_fA_f\kappa_d}dz \\ U_{torsion}^d = \int_0^a \frac{(M_z^d(z))}{2}(\theta_z^d)'dz \\ U_r^d = \frac{1}{2}k_r^d(\varphi_d(a))^2 \\ U_t^d = \frac{1}{2}k_t^d(u_y^d(a))^2 \end{cases} \tag{24}$$

9

$$\begin{cases} U_s = U_{bending}^s + U_{shear}^s + U_{torsion}^s + U_r^s + U_t^s \\ U_{bending}^s = \int_0^a \frac{(M_x^s(z))^2}{2(EI)_s} dz \\ U_{shear}^s = \int_0^a \frac{(V_y(z))^2}{2(GA)_s} dz \\ U_{torsion}^s = \int_0^a \frac{(M_z^s(z))}{2} (\theta_z^s)' dz \\ U_r^s = \frac{1}{2} k_r^s (\varphi_s(a))^2 \\ U_t^s = \frac{1}{2} k_t^s (u_y^s(a))^2. \end{cases} \tag{25}$$

The work done by the external forces is:

$$\begin{cases} L_{ext} = L_d + L_s \\ L_d = [Pu_y^d(z=0) + M_z^d(z=a)\theta_z^d(z=a)] \\ L_s = [Pu_y^s(z=0) + M_z^s(z=a)\theta_z^s(z=a)] \end{cases} \tag{26}$$

where $\theta_z^d(z=a) = \theta_z^s(z=a)$.

The energy release rate is defined here as the variation of the total potential energy due to a unit crack area extension, which implies a uniform extension of the crack front:

$$G = -\frac{1}{W} \frac{d\Pi}{da} \tag{27}$$

where W is the specimen width linked to the cracked surface area (see Fig. 3). As a result, a closed form expression for the energy release rate for a debonded sandwich specimen can be found as function of the applied load P using Eq. (27) by inserting in Eqs. (24)–(26) the expressions found in Eqs. (50)–(57):

$$\begin{cases} G_{SAN} = G_d + G_s \\ G_d = \frac{P^2}{2WG_f A_f \kappa_d} + \frac{P^2 a^2}{8WE_f I_f} \frac{(ak_r^d + 2E_f I_f)^2}{(ak_r^d + E_f I_f)^2} + \frac{(M_z^d(z=a))^2}{2WD_d} \frac{(1-e^{2ac_d})^2}{(1+e^{2ac_d})^2} \\ G_s = \frac{P^2}{2W(GA)_s} + \frac{P^2 a^2}{8W(EI)_s} \frac{(ak_r^s + 2(EI)_s)^2}{(ak_r^s + (EI)_s)^2} + \frac{(M_z^s(z=a))^2}{2WD_s} \frac{(1-e^{2ac_s})^2}{(1+e^{2ac_s})^2}. \end{cases} \tag{28}$$

where $M_z^d(z=a)$ and $M_z^s(z=a)$ are defined in terms of the applied load P by Eq. (74).

2.6. Structural modelling for a monolithic laminate

The energy release rate expression for a monolithic laminate can be derived following the same procedure described with Eqs. (1)–(28). In this case, the two delaminated arms are beams with homogeneous and same cross-section properties. Therefore the constants k_t, k_r, D, Γ are the same for the upper and lower beam.

Furthermore, it is possible to express k_r only through material and geometrical properties. Following the work done in [8,43–45], the strain energy density in the intact portion of the specimen is bounded by the following inequality:

$$\frac{\partial U}{\partial z} \leqslant 2\frac{\partial U}{\partial z}(z=a)e^{-2kz} \qquad a \leqslant z \leqslant \infty \tag{29}$$

where characteristic decay rates k in an isotropic material and in an orthotropic material with $E_f \gg E_y$, $E_f \gg G_f$ or $G_f \simeq E_f$ are:

$$k = \frac{2 \cdot 2.1061}{b} \quad \text{forisotropy} \tag{30}$$

$$k = \frac{2\pi}{b}\left(\frac{G_f}{E_f}\right)^{\frac{1}{2}} \quad \text{for orthotropy.} \tag{31}$$

The decay rate k is related to the characteristic decay length of Saint Venant's end effects by $d = ln(100)/k$, with d the distance where stresses decay to 1% of their value at $z = 0$. Additional values of d and k for general orthotropic materials can be found in [46].

The elastic strain energy density can be expressed as a function of the bending moment, material properties and geometry of the face sheet:

$$\frac{\partial U}{\partial z}(z=a) = \frac{1}{2}I_f E_f(u_y'')^2 = \frac{1}{2}\frac{M_x^2(z=a)}{I_f E_f} = \frac{6M_x^2(z=a)}{b^3 t_f E_f}. \tag{32}$$

Then, the strain energy can be found integrating Eq. (29) and using the relationship (32):

$$U \leqslant \int_0^\infty 2\frac{\partial U}{\partial z}(z=a)e^{-2kz}dz = \frac{12M_x^2(z=a)}{b^3 t_f E_f}\int_0^\infty e^{-2kz}dz = \frac{6M_x^2(z=a)}{b^3 t_f E_f k}. \tag{33}$$

Finally using Castigliano's second theorem k_r can be expressed only in function of material properties and geometry of the specimen:

$$\varphi(z) = \frac{\partial U}{\partial M_x} \tag{34}$$

$$k_r = \frac{M_x(z = a)}{\varphi(z = a)} = \frac{b^3 t_f E_z k}{12}. \tag{35}$$

The bending and shear stiffnesses are $E_f I_f$ and $G_f A_f \kappa_d$. Moreover, Eq. (73) becomes:

$$C_1 = t_f + h = C_2 \tag{36}$$

since $D_d = D_s = D$, $\mu_d = \mu_s = \mu$ and $\rho = \frac{t_f}{2}$. This shows that $M_z^d(z = a) = M_z^s(z = a) = M_z(z = a)$. Consequently, the equation for the energy release rate can be expressed for the monolithic laminate as:

$$G_{LAM} = \frac{P^2}{W G_f A_f \kappa_d} + \frac{P^2 a^2}{4 W E_f I_f} \frac{(a k_r + 2 E_f I_f)^2}{(a k_r + E_f I_f)^2} + \frac{(M_z(z = a))^2}{W D} \frac{(1 - e^{2ac})^2}{(1 + e^{2ac})^2} \tag{37}$$

2.7. Numerical model

A high-fidelity 3D FE based fracture mechanical model is formulated in order to verify the accuracy of the analytical solution. The FE mesh is presented in Fig. 8.

A global model and a submodel have been created. The global model represents the whole specimen with boundary conditions applied as in Fig. 3. The submodel includes only a material region surrounding the crack tip. Accordingly, the global model has been run first utilizing the sub-modelling technique [47]. Then, the displacements found as results of the global model are applied to the sub-model on its boundaries. A mesh sensitivity study on the G distribution along the crack front has been carried out in order to set the minimum element size in the width direction (y-direction in Fig. 8). The submodel has 100 elements along its width direction and an edge seeding has been made to have a finer mesh in proximity of crack edges. The ratio between the maximum and minimum element length (along the y-direction) is set equal to 6 and the width of the elements at the center of the specimen $y = 0$ has a size ratio of $l/t_f = 0.4$, where l is the length of the element in the y-direction.

The global model is employed in order to extract the numerical specimen compliance $C_{FE} = \Delta/P$, where Δ is the displacement corresponding to the applied load P. The variation of C_{FE} respect to a is used to calculate a global value for the energy release rate using the compliance method. Instead, the submodel is used to extract locally the energy release rate along the crack front. Both the global model and submodel are created and solved using the FE commercial software Abaqus® 2018. Brick elements are used with quadratic shape functions (element C3D20) for both the global model and submodel.

The compliance C_{FE} is extracted for different values of crack lengths. The energy release rate is thus defined through global structure parameters like P and C_{FE} as:
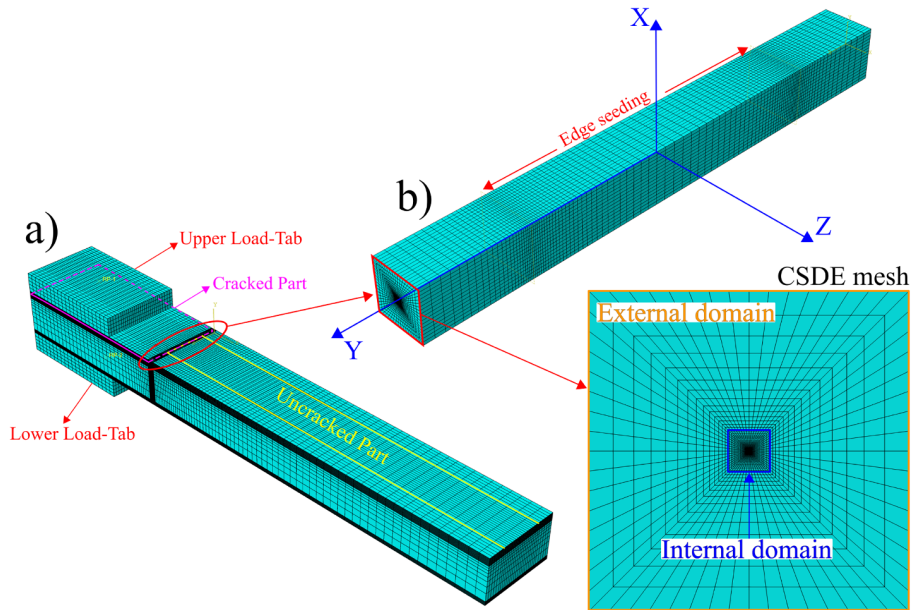

Fig. 8. (a) FE global model and (b) submodel.

$$G_{FE} = \frac{P^2}{2W} \frac{\partial C_{FE}}{\partial a}.$$

(38)

The local distribution of the energy release rate along the crack front is also extracted and compared with G_{FE} and the analytical values G_{SAN} and G_{LAM}, Eqs. (28, 37). The method used to extract the local energy release rate is the Crack Surface Extrapolation (CSDE) method and it is presented in [48]. A structured mesh consisting of two domains is adopted to accurately capture the displacement field near the crack tip. There are two domains of 17 rectangular rigs having decreasing element size towards the crack tip (Fig. 8). The smallest element size ratio used is $e_s/t_f = 1.5 \cdot 10^{-3}$. The number of elements inside the inner domain and along the 3D crack front is approximately $540 \cdot 10^3$. The CSDE method extracts the displacement jumps behind the crack front from the FE model (from the nodes lying on the crack flanks in the inner rig) and inserts them into the equations that relate the local displacement field behind the crack front to the local stress intensity factors and energy release rate components [15] (see appendix B).

Moreover, the FE model is used to perform parametric analyses to study the influence of the geometry on the local distribution of the energy release rate. The geometrical parameters, that have been investigated, are: the width b varying the ratio b/t_f and the crack length a varying the ratio a/t_f (fixing all the other geometrical parameters in both cases, see Table 1).

3. Results and discussion

The aim of building the FE model is triple: in the first place, the FE analysis verifies if a true anti-plane stress state is achieved locally along the crack front, secondly the FE model is useful to check the percentage of mode-III component in the energy release rate distribution at the crack front and thirdly the numerical model is necessary to validate the assumptions made in the analytical model.

The steady-state (crack length independent) solution of the energy release rate for antiplane conditions is:

$$G_{antiplane} = \frac{\tau_{zy}^2 b t_f}{W G_f}$$

(39)

where $\tau_{zy} = P/b t_f$.

The results for the parametric study varying the ratio b/t_f for $a/t_f = 10$ are presented in the figure below (all the other geometrical parameter used can be found in Table 1).

The graph in Fig. 9 reports the dimensionless mode-III component G_{III} (Eq. 75) of the energy release rate versus the dimensionless y-coordinate, that runs along the crack front. The local G_{III} distribution becomes progressively more constant on increasing b/t_f and approaches the limit anti-plane distribution for very large b/t_f, above 200. Since the width b of the specimen cannot be very large because of the load capability limit of the test rig presented in [35], a value of $b/t_f = 15$ is used to show the results in the dedicated section.

The finite element analyses are used to define the geometries where the mode-III component of the energy release rate dominates over the other components. This is shown in Fig. 10a, where the variations of the ratio G_{III}/G_{Tot} are presented for $b/t_f = 15$. Here, G_{Tot} is the total value of the energy release rate at different locations on the crack front calculated using (Eq. 75). The mode-III component of the energy release rate is always dominant in the central part of the crack front for all values of the crack length a/t_f. The mode-III component percentage decreases when a free edge is approached. When the crack length a/t_f increases, the edge effects intensify. As a matter of fact, the ratio G_{III}/G_{Tot} decreases substantially from $G_{III}/G_{Tot} = 0.9$ for $a/t_f = 15$ to $G_{III}/G_{Tot} = 0.47$ for $a/t_f = 35$. The geometry with $a/t_f = 15$ displays the widest portion of the crack front (from $y/W = 0.1$ to $y/W = 0.9$) that has a ratio $G_{III}/G_{Tot} \geqslant 0.9$. Fig. 10b illustrates the G_{III}/G_{Tot} variations for a sandwich composite specimen having $b/t_f = 20$. As expected the geometrical parameter b/t_f has a strong influence on the G_{III}/G_{Tot} distribution. The larger specimen width used for the sandwich, respect to the laminate case, promotes higher values of G_{III} for all crack lengths. The ratio G_{III}/G_{Tot} is as high as $\geqslant 0.8$, at the crack corners, even for values of $a/t_f = 50$.

A comparison between the analytical and the FE results is carried out next in order to verify the accuracy of the analytical model.
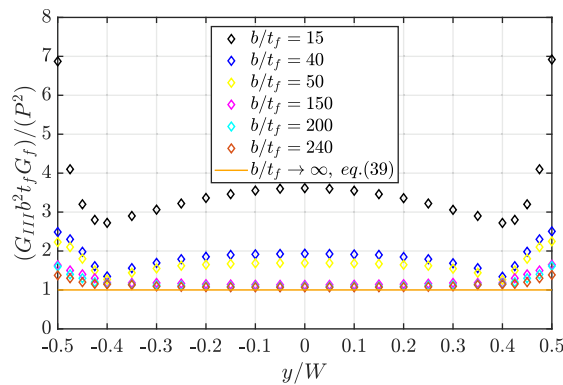
Fig. 9. Local distribution of the mode-III component of the energy release rate along the crack front for different values of b/t_f and a fixed $a/t_f = 10$. Monolithic laminate. CSDE method.

(a) Monolithic Laminate.

(b) Foam-cored Sandwich.
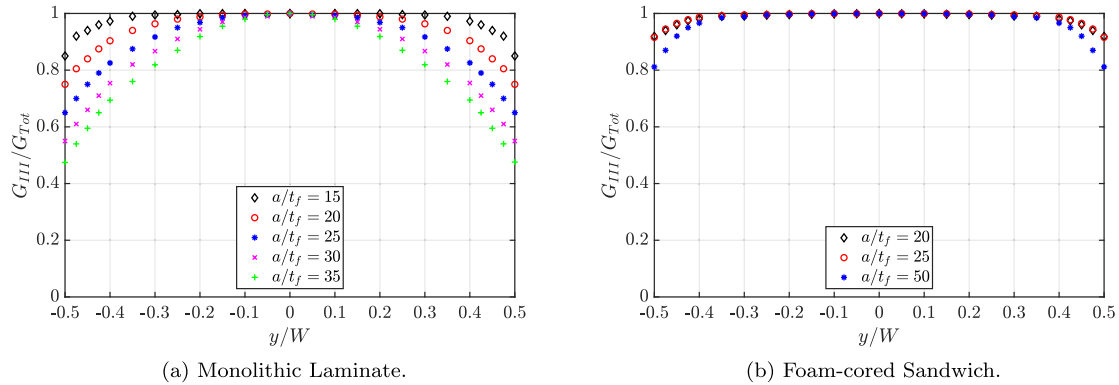
Fig. 10. Percentage of the mode-III component of the local energy release rate, along the crack front for different values of a/t_f. $b/t_f = 15$ for the monolithic laminate and $b/t_f = 20$ for the sandwich specimen.

The rotational stiffnesses of the crack front springs are plotted in Fig. 11 vs the crack length. Fig. 11a refers to the laminate and shows how k_r computed from the numerical model using Eqs. (8, 9) converges to the analytical value calculated using Eq. (35) when the defect length $a/t_f \geqslant 35$. For, shorter beams $a/t_f \leq 35$ the values of k_r, calculated numerically, deviate substantially from the analytical value and k_r becomes dependent on a/t_f.

The analytical value of k_r calculated from Eq. (35) and reported in Table 4 is used in the following applications for the monolithic laminate case. The rotational stiffnesses k_r^i of the sandwich specimen calculated with Eqs. 8,9 show a similar behaviour in Fig. 11b. There is a plateau for values of the normalized crack length $a/t_f \geqslant 40$ while for $a/t_f \leq 40$, k_r^i varies with the crack length. (see Table 5).

Eqs. (8, 9) are derived using the assumptions of the first order shear deformation beam theory and they use the values of the reaction moments $M_z^i(z = 0)$ (see Fig. 4), extracted from the FE model. Therefore, Fig. 11a-b highlight the range of applicability of the beam theory used to derive Eqs. (8 and 9). It is only for sufficiently long cracks that the rotational constants become approximately constant as they should be, and for short cracks the beam theory approximation becomes questionable. An average value $(k_r^i)_{avg}$ for k_r^i is computed using the values plotted in Fig. 11b for $40 \leqslant a/t_f \leq 50$.

The analytical values of the energy release rate G_{SAN} and G_{LAM} (Eqs. (28)–(37)) are compared with the numerical values G_{FE} on varying the normalized crack length a/t_f in Fig. 12. The relative difference between the analytical and the FE results is reported in Table 6 for three crack lengths.

Table 6 shows that for increasing values of the normalized crack length, the relative difference between the analytical and numerical energy release rate decreases.

The analytical and numerical values of the energy release rate are compared with the distribution of the local G along the crack front in Fig. 13a-b. The values of G_{FE} calculated with Eq. (38), G_{SAN} and G_{LAM} match the local values of G_{CSDE} at the center of the specimen where $y/W = 0.5$. The relative differences between G_{LAM} and G_{SAN} and the local value of the energy release rate at $y/W = 0.5$ are 1.5% and 11.1%. Moreover, the local distribution of G_{tot} is more uniformly distributed in the laminate. A complex and oscillating stress field is present locally at the crack tip due to the presence of a bi-material interface in the sandwich specimen [15]. This could explain the reduced accuracy of the analytical model when applied to the sandwich case.

The energy release rate peaks which are visible in Figs. 13a-b at coordinates $y/W = 0$ and $y/W = 1$, are due to the discontinuity of

(a) Monolithic Laminate.

(b) Foam-cored Sandwich.
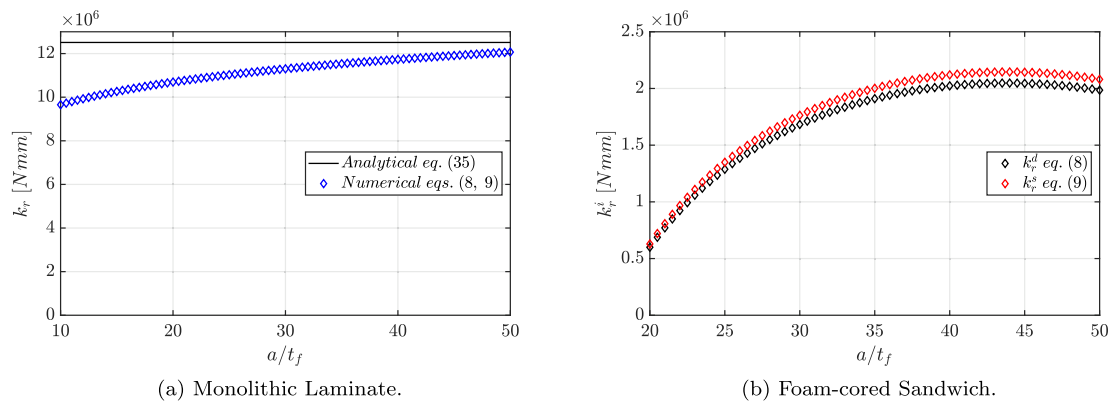
Fig. 11. (a) Plot of k_r computed analytically and numerically for the monolithic laminate with $b/t_f = 15$. (b) Plot of k_r^i computed numerically for the sandwich specimen with $b/t_f = 20$.

13

Table 4
Values of the parameters used to plot Eqs. (37) in Fig. 12a.

b/t_f	κ	$D\ [Nmm^2]$	$E\Gamma\ [Nmm^4]$	$k_r\ [Nmm]$
15	5/6	$2.80 \cdot 10^5$	$2.96 \cdot 10^7$	$1.25 \cdot 10^7$

Table 5
Values of the parameters used to plot Eqs. (28) in Fig. 12b.

	b/t_f	κ_i	$D_i\ [Nmm^2]$	$(E\Gamma)_i\ [Nmm^4]$	$k_r^i\ [Nmm]$	$(k_r^i)_{avg}\ [Nmm]$
$i = d$	20	5/6	$2.80 \cdot 10^5$	$2.96 \cdot 10^7$	Eq. (8)	$2.03 \cdot 10^6$
$i = s$	20	$4.5 \cdot 10^{-2}$	$7.91 \cdot 10^6$	$2.96 \cdot 10^7$	Eq. (9)	$2.13 \cdot 10^6$
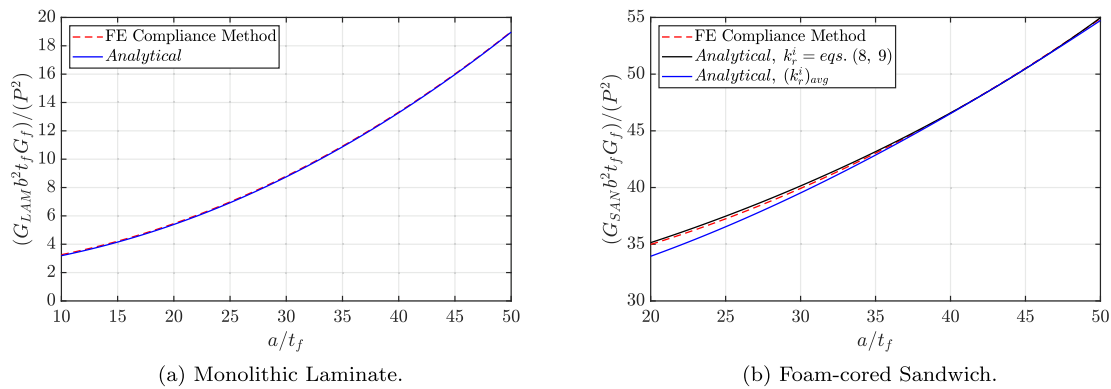
Fig. 12. Comparison between the analytical, Eqs. (28), (37)the numerical dimensionless energy release rate vs. normalized crack length. $b/t_f = 15$ for the monolithic laminate and $b/t_f = 20$ for the sandwich specimen.

Table 6
Comparisons between the analytical and numerical results $i = S, L$. The values of energy release rate for the sandwich G_S are taken from Eq. (28) using $(k_r^i)_{avg}$.

i	$t_f\ [mm]$	a/t_f	b/t_f	W/t_f	$(G_i - G_{FE})/G_i\ [\%]$
Laminate	2	10	15	13	2.23
	2	25	15	13	0.83
	2	40	15	13	0.33
Sandwich	2	20	20	12	3.07
	2	25	20	12	1.91
	2	30	20	12	1.00

the crack front. The crack front intersects the longitudinal cuts (see Fig. 3) at $y/W = 0$ and $y/W = 1$. In this region, the computation of the energy release rate is not accurate using the CSDE method, which is based on the solutions for plane and anti-plane conditions (Appendix A). The local displacement field at the crack front is described by other solutions near the free edges of the specimen, as it is explained in [49,50]. The value of W (see Table 1) has been chosen in order to maximize the uniformity of the distribution of the local G_{Tot}.

It is important for specimen design and sizing to understand how the different deformation mechanisms (shear, bending and torsion) contribute to the total energy release rate G_{LAM} and G_{SAN}. Fig. 14a-b represent the different terms appearing in Eqs. (28) and (37) for a ratio $b/t_f = 15$ for the monolithic laminate and $b/t_f = 20$ for the sandwich specimen. The plot in Fig. 14a shows that for very short crack lengths $a/t_f < 12$ the shear deformation contribution dominates over those of bending and torsion, this is when the anti-plane conditions dominate. On the other hand, for long crack lengths $a/t_f > 20$ the bending deformation term prevails. However, there are intermediate crack lengths values $12 < a/t_f < 20$ for which all deformation contributions (shear, torsion and bending) are relevant. Fig. 14b displays a different trend for the composite sandwich case. The dominant energetic term is the torsional term in the

(a) Monolithic GFRP Laminate.

(b) Foam-cored Sandwich.
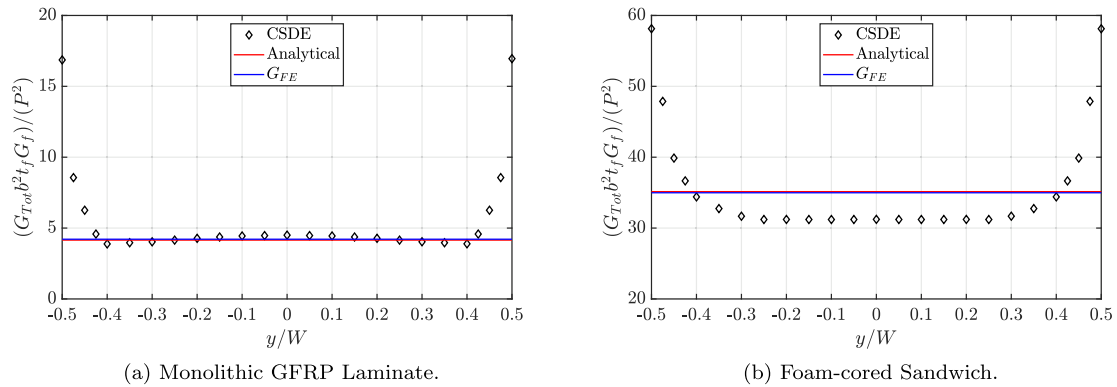
Fig. 13. Comparison between distributions of G computed analytically, numerically with compliance method and numerically through the CSDE. The y coordinate is running along the crack front, where $y = 0.5$ corresponds to the specimen center. The analytical values of G_{tot} Eqs. (28), (37) are plotted using the data from tabs. (1–5). The data are plotted for $a/tf = 15$ and $b/tf = 15$ for the monolithic laminate, $a/tf = 20$ and $b/tf = 20$ for the sandwich specimen.

range of crack lenghts considered for the sandwich $a/t_f < 50$. For $a/t_f > 50$, the energetic term representing the bending deformations varies quadratically with a/t_f (as for the monolithic laminate case) and it is always greater than the shear term.

(a) Monolithic GFRP Laminate.

(b) Foam-cored Sandwich.
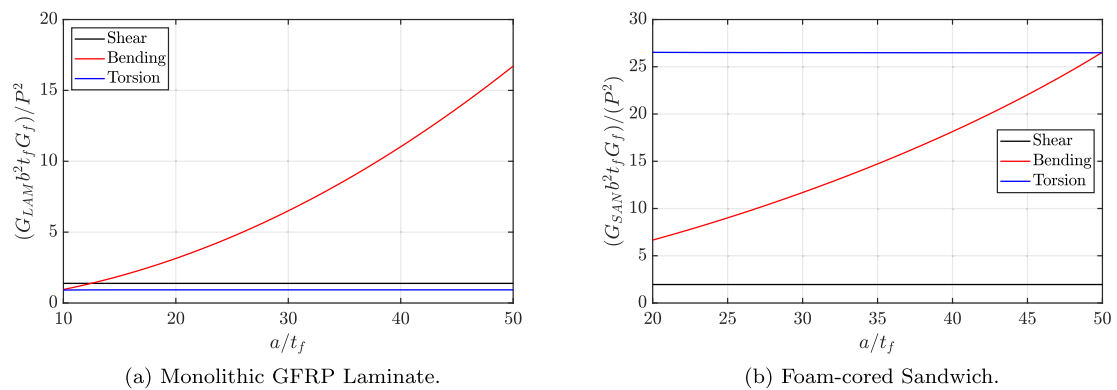
Fig. 14. The contributions from shear, bending and torsion to G are shown when the defect length varies. The different contribution from Eqs. (28, 37) are plotted using the data from tabs. (1–5). The data are plotted for $b/t_f = 15$ for the monolithic laminate and $b/t_f = 20$ for the sa.ndwich specimen.

The torsional contribution to G remains constant (over the range of a/t_f studied) and equal to the uniform torsion solution of the problem both for the monolithic laminate and sandwich. Results presented in Appendix A point out why the effects of non-uniform torsion are absent on G.

4. Conclusions

Analytical expressions for the global energy release rate G are derived for cracked composite sandwich and monolithic laminate specimens loaded in STB configuration. The analytical model is derived using first order shear deformation theory and Vlasov theory for non-uniform torsion of elastic beams and accounting for the effects of the near front deformations. The expressions of G can be used in connection with data reduction for the fracture test specimen presented in [35]. The analytical equations for G take into account the influence of all the geometrical/material parameters of the specimen. An expression for G was derived before in [9] for monolithic laminates. The main difference is that the equation derived here is fully analytical for monolithic laminates and requires, for a sandwich, just one parameter that can be determined experimentally or numerically. Moreover, the equations for G are expressed in function of the crack length instead the one presented in [9] can be used only for one value of a.

The analytical expressions of G are particularized for the presented material combinations. A comparison between the analytical model and a high-fidelity FE based fracture mechanics model is performed. The energy release rate is extracted from the numerical model globally using a compliance-based method and locally employing a displacement-based method. The biggest mismatch between analytical and numerical results is present in the sandwich specimen case, probably because local effects close to the crack front have a relevant influence on the local G distribution. These local effects are confined to a region surrounding the crack front and the beam theory, that has been used, is not capable to describe them accurately. Moreover, the analytical model predicts an unstable

crack growth if the fracture test presented in [35] is carried out in load control both for the monolithic laminate and for the foam-cored sandwich case. The analysis also confirms how it is not possible to achieve a pure anti-plane stress state (even in the central region of the crack front), because of the finite value of the specimen width b. Although, it is feasible to have a dominant mode-III component of the energy release rate in a rather big zone along the crack front using the specimen geometry selected for the fracture characterization test.

Declaration of Competing Interest

None.

Acknowledgements

Appendix A

A.1. Calculation of κ_s for the lower beam section

The shear correction factor of the substrate κ_s is computed imposing the equality between elastic energies associated with the substrate deformation, calculated using approximate beam theory and a Jourawski's type distribution. Fig. 15 shows the substrate section cut at a generic coordinate Z along the beam axis. It consists of a rectangular bi-material section, where the shear force V_Y is applied parallel to the layers width b together with the moment M_X^s. Here, τ_{avg} is considered the average value of the shear stress τ_{ZY} on the points lying at the same distance y from the cross section center. The Jouwraski approximation is used to compute the variation of τ_{avg} along the y-coordinate using: the Navier's stress distribution for bending stresses $\sigma_{ZZ} = \frac{M_X^s y E_i(X)}{(EI)_s}$, the local equilibrium for stresses $\sigma_{ZZ,Z} + \tau_{ZY,Y} = 0$ and equilibrium $\partial M_{X,Z}^s = V_Y$. Thus, the parameter τ_{avg} can be computed as function of the Y-coordinate:

$$\tau_{avg} = \frac{V_Y}{(t_f + t_c)(EI)_s}\left(\frac{b^2}{8} - \frac{Y^2}{2}\right)(E_f t_f + E_c t_c). \tag{40}$$
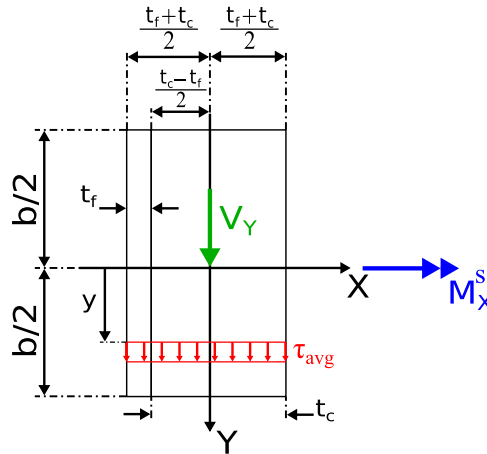
Fig. 15. Scheme of the substrate beam section, used to compute κ_s with the Jourawski approximation.

The equivalence between the elastic energies expressed by local and global variables:

$$\frac{1}{2}V_Y \gamma_{ZY} = \frac{1}{2}\int_{-b/2}^{b/2}\left(\int_{d_1}^{d_2}\frac{\tau_{ZY}^2}{G_i(x)}dZ\right)dY \tag{41}$$

where $\tau_{ZY} = \tau_{avg}$, $d_1 = -(t_f + t_c)/2$, $d_2 = (t_f + t_c)/2$ and $G_i(x)$:

16

$$G_i(x) = \begin{cases} G_f & \text{for} & \frac{t_c - t_f}{2} \leqslant x \leqslant \frac{t_c + t_f}{2} \\ G_c & \text{for} & -\frac{t_c + t_f}{2} \leqslant x \leqslant \frac{t_c - t_f}{2}. \end{cases} \tag{42}$$

Hence, solving Eq. (41) and since $\gamma_{ZY} = V_Y/((GA)_s \kappa_s)$, κ_s can be found in closed form as:

$$\kappa_s = \frac{5}{6} \frac{G_f G_c (t_c + t_f)^2}{(G_f t_f + G_c t_c)(G_f t_c + G_c t_f)}. \tag{43}$$

A.2. Calculation of k_t^d and k_t^s

The cross section of the lower delaminated arm at $z = a$ (in the xy-plane, Fig. 16) is modeled as built-in at its top edge (the crack front) and subjected to the shear force P. The core and face sheet shear deformations are γ_c and γ_f. The transverse spring stiffness is $k_t^s = P/\delta_{tot}^s$ with $\delta_{tot}^s = \delta_c + \delta_f$:

$$\gamma_c = \frac{\delta_c}{t_c} = \frac{P}{G_c A_c} \longrightarrow \delta_c = \frac{P t_c}{G_c A_c} \tag{44}$$

$$\gamma_f = \frac{\delta_f}{(t_f - \rho)} = \frac{P}{G_{XY} A_f} \longrightarrow \delta_f = \frac{P(t_f - \rho)}{G_{XY} A_f} \tag{45}$$

$$\delta_{tot}^s = \delta_c + \delta_f = P \left[\frac{t_c}{G_c A_c} + \frac{t_f - \rho}{G_{XY} A_f} \right] \tag{46}$$

$$k_t^s = \frac{P}{\delta_{tot}^s} = \frac{G_{XY} A_f G_c A_c}{G_c A_c (t_f - \rho) + G_{XY} A_f t_c}. \tag{47}$$
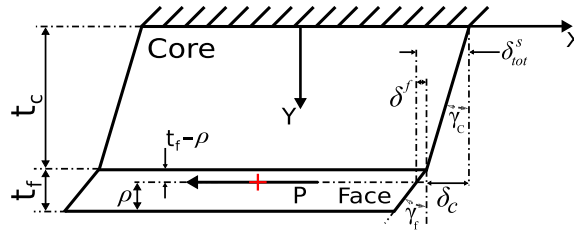
Fig. 16. Structural scheme used to calculate the expression for k_t^s (lower debonded arm). The red cross symbolize the shear center of the cross-section. (For interpretation of the references to colour in this figure legend, the reader is referred to the web version of this article.)

Following the procedure explained above k_t^d is calculated:

$$\gamma_f' = \frac{2\delta_{tot}^d}{t_f} = \frac{P}{G_{XY} A_f} \longrightarrow \delta_{tot}^d = \frac{P t_f}{2 G_{XY} A_f} \tag{48}$$

$$k_t^d = \frac{P}{\delta_{tot}^d} = \frac{2 G_{XY} A_f}{t_f}. \tag{49}$$
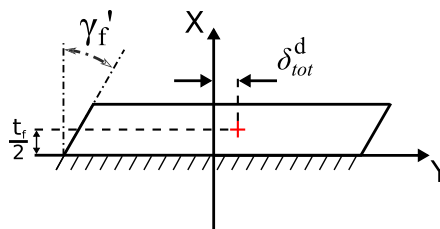
Fig. 17. Structural scheme used to calculate the expression for k_t^d (upper debonded arm), the red cross symbolize the shear center of the cross-section. (For interpretation of the references to colour in this figure legend, the reader is referred to the web version of this article.)

17

A.3. Closed form solution of the in plane problem

The closed form solutions for the internal forces, displacements and section rotation are reported below for the substrate:

$$M_x^s(z) = -Pz + \frac{Pa(ak_r^s + 2(EI)_s)}{2(ak_r^s + (EI)_s)} \tag{50}$$

$$V_y^s(z) = -P \tag{51}$$

$$\varphi_s(z) = -\frac{Pz^2}{2(EI)_s} + \frac{Pa(ak_r^s + 2(EI)_s)z}{2(ak_r^s + (EI)_s)(EI)_s} \tag{52}$$

$$\begin{cases} u_y^s(z) = P(Az^3 - Bz^2 - Cz + D) \\ A = \frac{1}{6(EI)_s} \\ B = \frac{a(ak_r^s + 2(EI)_s)}{4(ak_r^s + (EI)_s)} \\ C = \frac{1}{(GA)_s} \\ D = \frac{1}{k_t^s} + \frac{a}{(GA)_s} + \frac{a^3}{12(EI)_s}\frac{ak_r^s + 4(EI)_s}{ak_r^s + (EI)_s} \end{cases} \tag{53}$$

and for the delaminated face sheet:

$$M_x^d(z) = -Pz + \frac{Pa(ak_r^d + 2E_fI_f)}{2(ak_r^d + E_fI_f)} \tag{54}$$

$$V_y(z) = -P \tag{55}$$

$$\varphi_d(z) = -\frac{Pz^2}{2E_fI_f} + \frac{Pa(ak_r^d + 2E_fI_f)z}{2(ak_r^d + E_fI_f)E_fI_f} \tag{56}$$

$$\begin{cases} u_y^d(z) = P(Az^3 - Bz^2 - Cz + D) \\ A = \frac{1}{6E_fI_f} \\ B = \frac{a(ak_r^d + 2E_fI_f)}{4(ak_r^d + E_fI_f)} \\ C = \frac{1}{G_fA_f\kappa_d} \\ D = \frac{1}{k_t^d} + \frac{a}{G_fA_f\kappa_d} + \frac{a^3}{12E_fI_f}\frac{ak_r^d + 4E_fI_f}{ak_r^d + E_fI_f}. \end{cases} \tag{57}$$

The solution for the monolithic laminate has the same analytical form and is give by:

$$M_x(z) = -Pz + \frac{Pa(ak_r + 2E_fI_f)}{2(ak_r + E_fI_f)} \tag{58}$$

$$V_y(z) = -P \tag{59}$$

$$\varphi_f(z) = -\frac{Pz^2}{2E_fI_f} + \frac{Pa(ak_r^f + 2E_fI_f)z}{2(ak_r + E_fI_f)E_fI_f} \tag{60}$$

$$\begin{cases} u_y(z) = P(Az^3 - Bz^2 - Cz + D) \\ A = \frac{1}{6E_fI_f} \\ B = \frac{a(ak_r + 2E_fI_{xx})}{4(ak_r + E_fI_f)} \\ C = \frac{1}{G_fA_f\kappa_d} \\ D = \frac{1}{k_t} + \frac{a}{G_fA_f\kappa_d} + \frac{a^3}{12E_fI_f}\frac{ak_r + 4E_fI_f}{ak_r + E_fI_f}. \end{cases} \tag{61}$$

A.4. Calculation of the torsional and warping rigidities

The torsional and warping rigidities for the upper arm are defined as follows:

$$D_d = G_f bt_f^3 \beta \quad (E\Gamma)_d = E_f \iint (\psi_f)^2 dA \tag{62}$$

where ψ_d is the warping function of the upper arm cross-section which is considered a thin rectangle. Values of β for a prismatic homogeneous orthotropic beam are tabulated in [51] for different ratios of G_{yz}/G_{xz} and b/t_f. The expression for the torsional warping function of a mono-layer orthotropic beam ψ_f can be found in [51]. Whereas, the torsional and warping rigidity of the lower arm were found in [52] where the torsional case of a multi-layered orthotropic beam subjected to uniform torsion is studied. The torsional rigidity of the substrate D_s is reported in series form from [52]:

$$D_s = \frac{1}{3}b(t_f + t_c)^3(G_f K_f + G_c K_c) \tag{63}$$

where the terms K_f and K_c are given in [52] and refer to the face sheet and core. The warping rigidity $(E\Gamma)_s$ is defined as in Eq. (62):

$$(E\Gamma)_s = E_f \iint (\psi_f)^2 dA + E_c \iint (\psi_c)^2 dA \tag{64}$$

where the warping functions ψ_f and ψ_c are taken from [52]. The warping stiffness of the substrate $(E\Gamma)_s$ is dominated by the response of the lower face sheet, since $E_f \gg E_c$ (see Table 2). Values for β, K_f and Kc are presented in Table 7.

Table 7
Values of the constants used to compute the torsional rigidities of the delaminated part and the substrate.

β	K_f	K_c
0.307	$1.191 \cdot 10^{-3}$	1.335

Table 8 compares the values of torsional rigidities of the substrate part under uniform torsion (D_s, Eq. (63)) and non-uniform torsion (D_s^{FEM}) using a FE model. The beam is torsionally clamped at one end and subjected to a torque moment on the other end. The parameter $\mu_s(a)$ can be computed as the ratio between D_s and D_s^{FEM}. It is clear that bigger a/t_f is, more the uniform torsion solution is met. Although, the effects of non-uniform torsion are negligible even for $a/t_f = 20$, because $\mu_s(a) = 0.928$ that is close to 1. Effects of non-uniform torsion on the monolithic laminate beam follow the same trend showed in Table 8.

Table 8
Effects of non-uniform torsion on the substrate beam. Results are valid for $b/t_f = 20$.

a/t_f	D_s [Nmm^2]	$\mu_s(a)$	D_s^{FEM} [Nmm^2]	$\frac{D_s - D_s^{FEM}}{D_s}$ [%]
20	$7.9057 \cdot 10^6$	0.928	$8.5910 \cdot 10^6$	8.6
50	$7.9057 \cdot 10^6$	0.968	$8.1670 \cdot 10^6$	3.3
100	$7.9057 \cdot 10^6$	0.982	$8.0506 \cdot 10^6$	7.8
500	$7.9057 \cdot 10^6$	0.995	$7.9454 \cdot 10^6$	0.5

A.5. Calculation of the reaction moments in the torsional problem

The reaction torsional moments M_z^{Rd} and M_z^{Rs} depend linearly on the applied load through two C_1 and C_2:

$$M_Z^{Rd} = C_1 P \tag{65}$$

$$M_Z^{Rs} = C_2 P \tag{66}$$

The constants are found using rotational equilibrium about the z-axis and imposing kinematic compatibility for the rotations θ_z at coordinate $z = a$. The moments acting on each delaminated arm at $z = 0$ ($M_z^d(z = 0)$ and $M_z^s(z = 0)$) can be expressed in the following way, when all the loads are reported to the beams shear centres:

$$\begin{cases} M_z^d(z = 0) = M_Z^{Rd} - P(h + \frac{t_f}{2}) = C_1 P - P(h + \frac{t_f}{2}) \\ M_z^s(z = 0) = M_Z^{Rs} - P(h + \rho) = C_2 P - P(h + \rho) \end{cases} \tag{67}$$

The equilibrium equation yields a relationship between C_1 and C_2:

$$M_z^{Rd} + M_z^{Rd} - P(2t_f + 2h + t_c) = 0 \tag{68}$$

$$C_2 = -C_1 + 2t_f + 2h + t_c. \tag{69}$$

Kinematic compatibility is expressed as:

$$\theta_z^d(z = a) = \theta_z^s(z = a). \tag{70}$$

Hence, substituting Eq. 22 into Eq. 70 results in:

$$\frac{M_z^d(z = a)\mu_d(z = a)}{D_d} = \frac{M_z^s(z = a)\mu_s(z = a)}{D_s} \tag{71}$$

and remembering that $M_z^d(z = 0) = M_z^d(z = a)$ and $M_z^s(z = 0) = M_z^s(z = a)$:

$$\frac{(C_1 - h - t_f/2)\mu_d(z = a)}{D_d} = \frac{(C_2 - h - \rho)\mu_s(z = a)}{D_s}. \tag{72}$$

Now, using Eq. (69) and setting $\chi = \frac{D_s}{D_d}\frac{\mu_d(z=a)}{\mu_s(z=a)}$, C_1 can be found:

$$C_1 = [1 + \chi]^{-1}\left[h(1 + \chi) + t_f\left(\frac{\chi}{2} + 2\right) + t_c - \rho\right]. \tag{73}$$

Therefore the equations above also define the internal torsional moments at the crack front:

$$\begin{cases} M_z^d(z = a) = P(t_c + h + \frac{t_f}{2} - C_2) \\ M_z^s(z = a) = P(t_c + t_f + h - \rho - C_1). \end{cases} \tag{74}$$

A.6. Torsional stress distribution on substrate cross section

Fig. 18.
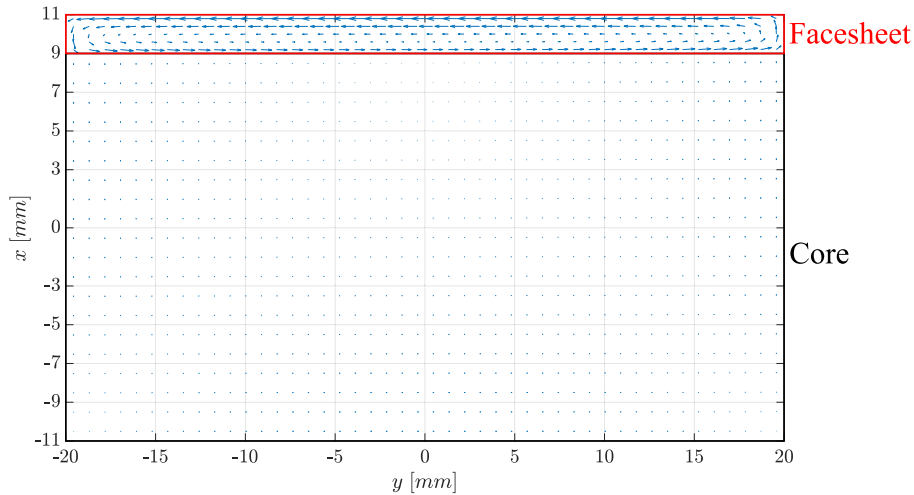
Fig. 18. Vectorial plot of the torsional shear stresses τ_{zx} and τ_{zy} on the substrate beam section. The geometrical and material properties used in this plot can be found in Tables 1 and 2.

Appendix B

B.1. CSDE Method

The local values of the energy release rate can be calculated using finite element measurements of the displacements along the crack surfaces behind the crack front [15]. The numerical solution gives the relative openings δ_x, δ_y and δ_z between two nodes lying on the crack flanks at $\theta = \pm\pi$, see Fig. 19. Then δ_x, δ_y and δ_z can be substituted in the local field equation Eq. (75) presented in [15] to compute the local values (for each node pair that lies in a plane intersecting the crack front at a coordinate y and orthogonal to the front) of the energy release rate:

$$G^{CSDE}(r, \theta, y) = \frac{\pi(1 + 4\,\epsilon^2)}{8H_{11}|r|}\left(\frac{H_{11}}{H_{22}}\delta_x^2 + \delta_z^2\right) + \frac{\pi\delta_y^2}{8|r|(B_1 + B_2)}. \tag{75}$$

Eq. (75) should provide a unique value of G for each xz-plane when $r \to 0$. The bi-material constants H_{11} and H_{22} are defined in [15] as follows:

Fig. 19. Interface crack-tip geometry in sandwich composite.

$$H_{11} = (2n\lambda^{\frac{1}{4}}\sqrt{S_{11}S_{22}})_1 + (2n\lambda^{\frac{1}{4}}\sqrt{S_{11}S_{22}})_2 \tag{76a}$$

$$H_{22} = (2n\lambda^{-\frac{1}{4}}\sqrt{S_{11}S_{22}})_1 + (2n\lambda^{-\frac{1}{4}}\sqrt{S_{11}S_{22}})_2 \tag{76b}$$

where S_{ij} are the material compliances defined in [15] and B_1 and B_2:

$$B_1 = (\sqrt{S_{44}S_{55} - S_{45}^2})_1 \tag{77a}$$

$$B_2 = (\sqrt{S_{44}S_{55} - S_{45}^2})_2 \tag{77b}$$

The parameters λ and n are defined in [15] as:

$$\lambda = \frac{S_{11}}{S_{22}} \tag{78a}$$

$$n = \sqrt{0.5(1 + \rho)} \quad where \quad \rho = \frac{2S_{12} + S_{66}}{2\sqrt{S_{11}S_{22}}} \tag{78b}$$

The subscripts 1 and 2, on the parameters B_i, S_{ij}, refer to the two different materials that join at the interface. Fig. 19 shows the crack geometry and the meaning of the terms δ_x, δ_y, δ_z in Eq. (75). Two coincident points in the crack un-deformed configuration, they are separated in the deformed configuration by a jump equal to δ_y in the y-direction, equal to δ_x in the x-direction and equal to δ_z in the z-direction. The oscillatory index ϵ is given by:

$$\epsilon = \frac{1}{2\pi}\ln\left(\frac{1 - \beta}{1 + \beta}\right) \tag{79}$$

where β is the Dundurs [53] bi-material parameter defined in [15] as:

$$\beta = \frac{[\sqrt{S_{11}S_{22}} + S_{12}]_2 - [\sqrt{S_{11}S_{22}} - S_{12}]_1}{\sqrt{H_{11}H_{22}}} \tag{80}$$

Parameters H_{11} and H_{22} must be computed differently if the problem is treated as plane stress or plane strain. The material compliances S_{ij} have to be computed differently if the problem analysed presents a plane stress or strain state. The plane strain formulation of H_{11} and H_{22} is used to extract the values of the energy release rate in this work.

The stress field associated with the in-plane crack opening modes (I-II) shows an oscillatory character due to the presence of the oscillatory index ϵ. Instead, the stress field related to the out-of-plane sliding mode (mode III) does not present any oscillatory feature and it is not coupled with the in-plane stress field as found in [15]. Therefore, it is possible to compute separately the mode III component G_{III} (second term on the right-hand side of Eq. 75). Then, it possible to find G_{I-II} (first term on the right-hand side of Eq. 75) subtracting G_{III} from the total value of G.

The main issue is the presence of a zone, close to the crack tip, where the stress and displacement fields oscillate due to the presence of the index ϵ. The oscillating field is present in the case of composite sandwich because there is a mismatch between the elastic properties of the face sheets and the core. Numerical errors in the vicinity of the crack front makes the direct use of Eq. (75) difficult.

A numerical method which circumvents the numerical errors in computing G using Eq. (75) in the limit for $r \to 0$ is developed in [54]. This method is called Crack Surface Extrapolation (CSDE). The CSDE method extracts the displacement jumps between the nodes lying on the crack flanks in the K-dominant zone (see Fig. 20). Then, the CSDE extracts the jumps δ_x, δ_y and δ_z for each nodal pair and it calculates G using Eq. (75). Thus, the trend of the energy release rate can be plotted against the x-coordinate along the crack bisector. Finally, the method fits with a straight line the values of G vs. r and it extrapolates the value of the energy release rate to the crack tip. The extrapolation allows to shoot-over the numerical error zone. The CSDE method is implemented in the commercial FE software Abaqus® as a Python script.
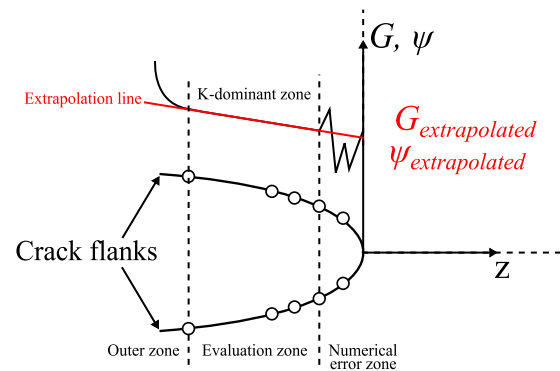
Fig. 20. Schematics of the CSDE method.

References

[1] Carlsson L, Kardomateas G. Structural and failure mechanics of sandwich composite. Springer Science & Business Media 2011;1(1): 10–20.

[2] Zenckert D. An investigation to sandwich construction. Chamaleon Press.

[3] T. of Canada, Loss of rudder, airbus 310–308, air transat flight 961, TSB 1 (1); 2005 –.

[4] Glaessagen E, Reeder J, Sleigth D, Wang J, Raju I, Harris C. Debonding failure of sandwich-composite cryogenic fuel tank with internal core pressure. J Spacecr Rock 2005;42(4):613–27. https://doi.org/10.2514/1.5567.

[5] Vantini U. Investigating effects of pure shear deformation in wind turbine blade sub-structures, Master Thesis, Politecnico di Milano 2014;1(1)–.

[6] Quispitupa A, Berggreen C, Carlsson L. On the analysis of a mixed mode bending sandwich specimen for debond fracture characterization. Eng Frac Mech 2009;76(4):594–613. https://doi.org/10.1016/j.engfracmech.2008.12.008.

[7] Lee S. An edge crack torsion method for mode iii delamination fracture testing. J Compos Technol 1993;15(3):193–201.

[8] Szekrenyes A. Improved analysis of the modified split-cantilever beam for mode-iii fracture. Int J Mech Sci 2009;51(9–10):682–93. https://doi.org/10.1016/j.ijmecsci.2009.07.005.

[9] Davidson B, Sediles F. Mixed mode i–ii–iii delamination toughness determination via shear-torsion-bending test. Compos Part A-Appl Sci Manuf 2011;42(6):589–603. https://doi.org/10.1016/j.compositesa.2011.01.018.

[10] Ratcliffe J. Characterization of the edge crack torsion test for mode iii fracture toughness measurement of laminated composites, NASA-TM-2004-213269 2004;1(1)–.

[11] Morais AD, Pereira A, De Moura M, Magalhaes A. Mode iii interlaminar fracture of carbon/epoxy laminates using the edge crack torsion (ect) test. Compos Sci Technol 2009;69(5):670–6. https://doi.org/10.1016/j.compscitech.2008.12.019.

[12] Pennas D, Cantwell W, Compston P. The influence of strain rate on the mode iii interlaminar fracture of composite materials. J Compos Mater 2007;41(21):2595–614. https://doi.org/10.1177/0021998307078690.

[13] Robinson P, Song D. The development of an improved mode iii delamination test for composites. Compos Sci Technol 1994;52(2):217–33. https://doi.org/10.1016/0266-3538(94)90207-0.

[14] Cicci D, Kortschot T. Data reduction for the split cantilever beam mode iii delamination test. fatigue and fracture. In: Proceedings of the 10th International conference on composite materials 1995;1(1): 189–96. doi:-.

[15] Suo Z. Singularities, interfaces and cracks in dissimilar anisotropic media. Royal Soc A: Math, Phys Eng Sci 1990;427(1873):331–58.

[16] Benthem JP. State of stress at the vertex of a quarter-infinite crack in a half-space. Int J Solids Struct 1977;13(5):479–92. https://doi.org/10.1016/0020-7683(77)90042-7.

[17] Dhondt G. Analysis of the boundary layer at the free surface of a half circular crack. Eng Fract Mech 1998;60(3):273–90. https://doi.org/10.1016/S0013-7944(98)00026-5.

[18] Hartranft RJ, Sih GC. An approximate three-dimensional theory of plates with application to crack problems. Int J Eng Sci 1970;8(8):711–29. https://doi.org/10.1016/0020-7225(70)90054-6.

[19] Fenner DN, Abdul Mihsein MJ. Crack front elastic stress state for three-dimensional crack problems. Int J Fract 1984;25(2):121–31. https://doi.org/10.1007/BF01141555.

[20] Nakamura T, Parks DM. Antisymmetrical 3-D stress field near the crack front of a thin elastic plate. Int J Solids Struct 1989;25(12):1411–26. https://doi.org/10.1016/0020-7683(89)90109-1.

[21] Nakamura T. Three-dimensional stress fields of elastic interface cracks. ASME 1991;58(4):939–46.

[22] Pook LP. A 50-year retrospective review of three-dimensional effects at cracks and sharp notches. Fatigue Fract Eng Mater Struct 2013;36(8):699–723. https://doi.org/10.1111/ffe.12074.

[23] Pook LP, Berto F, Campagnolo A, Lazzarin P. Coupled fracture mode of a cracked disc under anti-plane loading. Eng Frac Mech 2014;128(C):22–36. https://doi.org/10.1016/j.engfracmech.2014.07.001.

[24] Pook LP, Berto F, Campagnolo A, Lazzarin P. Coupled fracture mode of a cracked disc under anti-plane loading. Eng Frac Mech 2014;128(C):22–36. https://doi.org/10.1016/j.engfracmech.2014.12.021.

[25] Campagnolo A, Berto F, Lazzarin P. The effects of different boundary conditions on three-dimensional cracked discs under anti-plane loading. Eur J Mech, A/Solids 2015;50:76–86. https://doi.org/10.1016/j.euromechsol.2014.11.001.

[26] Campagnolo A, Berto F, Pook LP. Three-dimensional effects on cracked discs and plates under nominal Mode III loading. Frattura ed Integrita Strutturale 2015;9(34):190–9. https://doi.org/10.3221/IGF-ESIS.34.20.

[27] Kotousov A, Lazzarin P, Berto F, Harding S. Effect of the thickness on elastic deformation and quasi-brittle fracture of plate components. Eng Frac Mech 2010;77(11):1665–81. https://doi.org/10.1016/j.engfracmech.2010.04.008.

[28] Kotousov A, Berto F, Lazzarin P, Pegorin F. Three dimensional finite element mixed fracture mode under anti-plane loading of a crack. Theoret Appl Fract Mech 2012;62(1):26–33. https://doi.org/10.1016/j.tafmec.2013.01.003.

[29] Kotousov A, Lazzarin P, Berto F, Pook LP. Three-dimensional stress states at crack tip induced by shear and anti-plane loading. Eng Frac Mech 2013;108:65–74. https://doi.org/10.1016/j.engfracmech.2013.04.010.

[30] Barbieri L, Massabo' R, Berggreen C. The effects of shear and near tip deformations on interface fracture of symmetric sandwich beams. J Compos Tech Res 2018;201(1):298–321. https://doi.org/10.1016/j.engfracmech.2018.06.039.

[31] Andrews M, Massabó R. The effects of shear and near tip deformations on energy release rate and mode mixity of edge-cracked orthotropic layers. Eng Frac Mech

2007;1(74):2700–20.

[32] Czabaj M, Ratcliffe J, Davidson B. Observation of intralaminar cracking in the edge crack torsion specimen. Eng Fract Mech 2014;120:1–4.

[33] Horner A, Czabaj M, Davidson B, Ratcliffe J. Three-dimensional crack surface evolution in mode III delamination toughness tests. Eng Fract Mech 2015;149:313–25.

[34] Horner A, Davidson B. Fracture surface evolution and apparent delamination toughness in split composite beam specimens subjected to mixed mode I-III loading. Compos Part A: Appl Sci Manuf 2015;79:92–102.

[35] Sabbadin P, Berggreen C, Legarth B. Development of a mode i/ii/iii test fixture for composite laminates and sandwich face/core fracture characterization. in: Proceedings of 12th international conference on sandwich structures 2018;1(1): 35–7. doi:-.

[36] Jones R. Mechanics of composite materials. Taylor and Francis.

[37] ASTM, Standard Test Method for Tensile Properties of Polymer Matrix Composite Materials, D3039/D3039M-17 1–13.

[38] ASTM, Standard Test Method for Shear Properties of Composite Materials by V-Notched Rail Shear Method, D7078/D7078M-12 1–15.

[39] ASTM, Standard test Method for Shear Properties of Composite Materials by the V-Notched Beam Method, D5379/D5379M-12 1–14.

[40] Adams D, Carlsson L, Pipes R. Experimental characterization of advance composite materials. CRC Press; 2003. p. 87–96.

[41] Diab. Divinycell H technical data sheet 2018; 1–2.

[42] Vlasov V. Thin-walled elastic bars, Fizmatgiz, Moscow 1959;1(1) doi:-.

[43] Horgan C. On saint-venant's principle in plane anisotropic elasticity. J Elast 1972;2(1):169–80.

[44] Olsson R. A simplified improved beam analysis of the dcb specimen. Compos Sci Technol 1992;43(1):329–38. https://doi.org/10.1016/0266-3538(92)90056-9.

[45] Horgan C, Carlsson L. Saint-venant end effects for anisotropic materials. Reference Module Mater Sci Mater Eng 2018;1(1):38–55.

[46] Ustinov K, Massabó R, Lisovenko D. Orthotropic strip with central semi-infinite crack under arbitrary loads applied far apart the crack tip. analytical solution. Eng Fail Anal 2018;110(104410):1–12. https://doi.org/10.1016/j.engfailanal.2020.104410.

[47] D. Systems, Abaqus online manual.

[48] Berggreen C. Damage tolerance of debonded sandwich structures, PhD Thesis 2004;1(1): 7–21.

[49] Benthem J. State of stress at the vertex of a quarter-infinite crack in a half-space. Int J Solids Struct 1977;13:479–92.

[50] Bazant Z, Estenssoro L. Surface singularity and crack propagation. Int J Solids Struct 1979;15(-): 405–26. doi:-.

[51] L.S.G. Theory of elasticity of an anisotropic body, p. 283–8.

[52] Systems D. Torsional response of inhomogeneous and multilayered composite beams. Compos Struct 1993;25:587–94.

[53] D.J. Edge-bonded dissimilar orthogonal elastic wedge, J Appl Mech 1969; 650–52.

[54] Berggreen C, Simonsen BC. Non-uniform compressive strength of debonded sandwich panels - II. Fracture mechanics investigation, Vol. 7; 2005. https://doi.org/10.1177/1099636205054790.

9. Paper 2

[P2]
A novel test fixture for mode III fracture characterization of monolithic laminates and composite sandwich specimens.

A novel test fixture for mode III fracture characterization of monolithic laminates and composite sandwich specimens

Pietro Sabbadin

Department of Mechanical Engineering, Technical University of Denmark, Kgs. Lyngby, Niels Koppels Allé, Building 404

Christian Berggreen*

Department of Mechanical Engineering, Technical University of Denmark, Denmark

Brian Nyvang Legarth

Department of Mechanical Engineering, Technical University of Denmark, Denmark

Lujin Lin

Department of Mechanical Engineering, Technical University of Denmark, Denmark

Abstract

This work presents a novel test fixture for mode III fracture characterization of delaminations in monolithic laminates and face-core debonds in foam core composite sandwich specimens. The test fixture is configured as an extension of the already existing shear-torsion-bending (STB) test designed for monolithic laminates. The specimen sizing, lay-up configuration and the manufacturing process are presented. Accordingly, an overview of the test fixture is provided along with the data reduction method employed to compute the energy release rate. The results from representable fracture characterization tests are presented as force vs. displacement curves, where different definitions of the critical load for crack propagation can be defined. Thus, the critical value of the energy release rate is computed using analytically based equations for the different definitions given for the critical loads. The results show a stable crack growth for monolithic laminate specimens. However, a highly non-linear response of the sandwich specimens, before the onset of crack propagation, is observed. A non-linear numerical analysis and destructive specimen inspections are carried out in order to identify the source of the non-linear behaviour observed in the experimental results.

Keywords: Debonding, Interface, Fracture toughness, Mode III, Test Rig

---
*Corresponding author
Email address: cbe@mek.dtu.dk (Christian Berggreen)

1. Symbols

Latin Symbols

a Crack length.

b Specimen width.

L Total specimen length.

P External load.

t_f Face sheet thickness.

t_c Core thickness.

W Width of the bonded part of the specimen.

X, Y, Z Axes labels of coordinate reference system for the specimen.

G Energy release rate.

Indexes

c, f Indices to indicate the face sheet and the core.

d, s Indices for delaminated (upper beam) and substrate (lower beam).

LAM, SAN Indices referring either to the monolithic laminate or the sandwich.

2

2. Introduction

Interlaminar fracture characterization of composite materials under mode III loading represents a challenging topic. Mode III loading is de-coupled from mode I and mode II in the case of an interface crack between two dissimilar anisotropic materials as reported in [1]. Furthermore, mode III opening of cracks in composite materials can represent a non-negligible part of the total energy release rate at the crack tip in real engineering loading scenarios where also mixed mode I/II loadings are present as reported in [2]. Mode III fracture characterization is less covered by the present literature compared to mode I/II fracture characterization testing. Four main early publications focused on mode III fracture testing are the following: [3] proposes the Crack Rail Shear (CRS) specimen to characterize the mode III interlaminar fracture toughness of a composite laminate, [4, 5] present a study on interlaminar fracture propagation (under mode III loads) using a split cantilever beam specimen (SCB) and [6] introduces the Edge Crack Torsion (ECT) specimen to study mode III fracture in composite laminates. More recently, SCB geometries in [7–11] and plate-like specimens in [12, 13] have been proposed as suitable experimental tests for mode III interlaminar fracture characterization of composite laminates and wooden materials. Specimens with a SCB geometry are also employed in mode III fracture characterization tests for metals in [14] along with specimens with a geometry similar to the compact tension specimen as in [15–18]. However, three experimental test specimens exist in the literature which can be considered the more matured candidates in terms of mode III fracture characterization of monolithic laminates. These three test specimens include: the Edge Crack Torsion test (ECT) [19], the Modified Split Cantilever Beam (MSCB) test [20] and the Shear Torsion Bending test (STB) [21] (fig. 1).
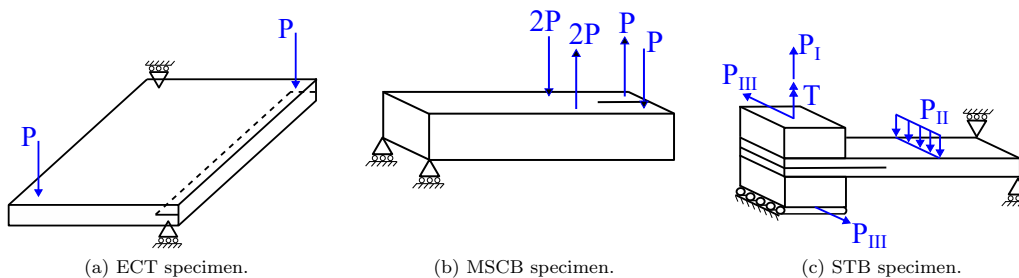

Figure 1: Simplified and schematic illustrations of the test fixtures designed to perform fracture characterization tests under out-of-plane shear loadings.

In the ECT test, a delaminated plate subjected to a twisting moment, which results in a distribution of out-of-plane shear stresses along the debonded front is used to generate a mode III stress field at the crack front. In the MSCB test, a beam-like specimen is used, and two scissoring forces are applied on the two delaminated arms, in order to induce mode-III openings of the crack flanks. A common characteristic of the ECT and MSCB tests is the lack of local uniformity in the stress field along the crack front. The load-free lateral edges of the specimen are the principal source of non-uniformity in the stress field along the crack front, and these edges cause the out-of-plane shear stresses to change abruptly from the central part of the crack front to the crack edges, where they have to be zero according to static equilibrium. This phenomenon is causing the variation of the mode-III energy release rate component (see fig. 2) in a zone close to the lateral specimen free-edges as observed in [22]. Hence, the mode III fracture toughness measured using these specimens, will be associated with a certain mode-mixity between mode II and III and thus not accurate. Moreover, recent experimental studies on the ECT specimen [23–25] proved that the presence of additional damaging modes, like intra-laminar cracks, makes the ECT not directly suitable to pure mode III fracture toughness values in monolithic laminates.

In the STB test, the specimen is loaded using two stiff load blocks, which prevent the rotation of the specimen's arms due to the bending moments present. Moreover, the crack front geometry is
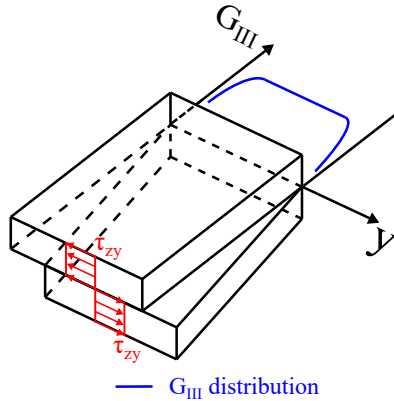
<div align="center">3</div>

Figure 2: Distribution of the energy release rate mode III component G_{III} along the crack front in the ECT and MSCB specimens. τ_{zy} are the shear stresses applied on the crack flanks.

modified to favour a more uniform distribution of mode III along the crack front, compared with the ECT and MSCB tests. However, the STB test fixture in [21] can also apply mode I and II loading. Therefore, the novel test fixture presented in this work, is inspired by the STB test fixture in its pure mode III configuration only. The main difference between the STB fixture ([21]) and the novel test fixture is related to testing of sandwich specimens (in addition to monolithic laminates) and to the fact that a new data reduction method ([26]) was used to reduce the energy release rate at the crack front from measured data.

The main scope of this work is to present a pilot experimental study. It is carried out on a limited amount of monolithic laminates and foam core sandwich specimens loaded under pure mode III loading, to investigate the experimental performance of the novel dedicated mode III test fixture and modified STB specimen geometry presented in this study. The analytical equations derived in [26] are used to extract the energy release rate from measured forces and moments.

3. Test fixture, specimens and data reduction method

3.1. Test rig presentation

The test fixture is installed in a MTS 858 axial-torsional servo-hydraulic test machine operated with a MTS FlexTest 100 controller and the MTS TestSuite software package (fig. 3). Two servo-hydraulic actuators are present: one horizontal and one vertical. The horizontal actuator is clamped to a T-slot table in the test machine, and has a maximum capacity of 5 kN. It allows the application of the external mode III load P (fig. 4) onto the cracked specimen. The vertical main actuator in the test machine, is an axial-torsional actuator with an axial capacity of 25 kN and torsional capacity of 250 Nm. The vertical actuator allows to sufficiently open the crack flanks in order to avoid contact friction between the crack flanks during mode III testing due to the torsional moments described in [26].

Two load cells are present in the text fixture: one is mounted on the horizontal actuator and has a capacity of 5 kN (fig. 4) and a second one is installed on the vertical actuator and has an axial capacity of 10 kN and torsional capacity of 200 Nm (fig. 3). The shearing load P is applied through compressive contact between the horizontal actuator and the load-block which is allowed to slide on a rail with linear bearings. However, the load-block is rigidly connected to the lower load-tab of the specimen, and this allows the load P to be transmitted through the specimen to the upper-load tab (fig. 4). An extensometer (MTS model 634.31F-25, with a 25 mm gauge length) is used to measure the relative sliding δ of the two load-tabs along the load application direction (fig. 4). The extensometer is linked to the two load tabs employing two steel connectors (fig. 4). In addition, a steel beam is clamped to the test machine lateral columns to prevent horizontal deformations to be applied to the

4

vertical axial-torsional actuator, due to the presence of the horizontal side load P (fig. 4). The vertical actuator slides through a bearing positioned in a hole positioned at the middle of the steel beam.
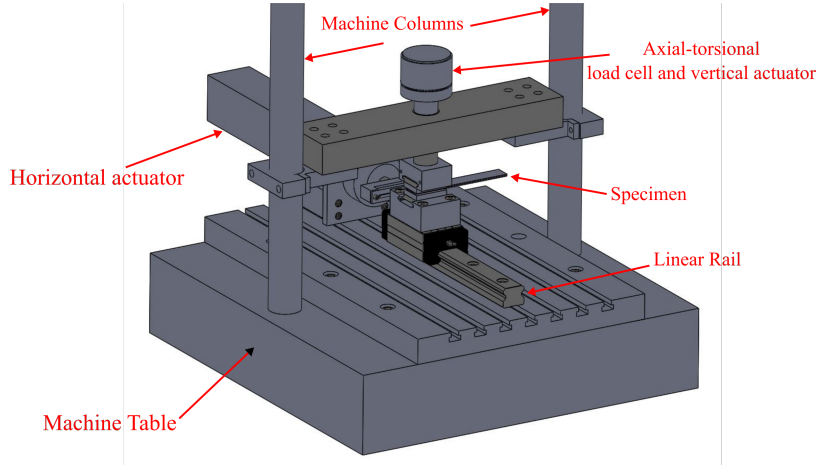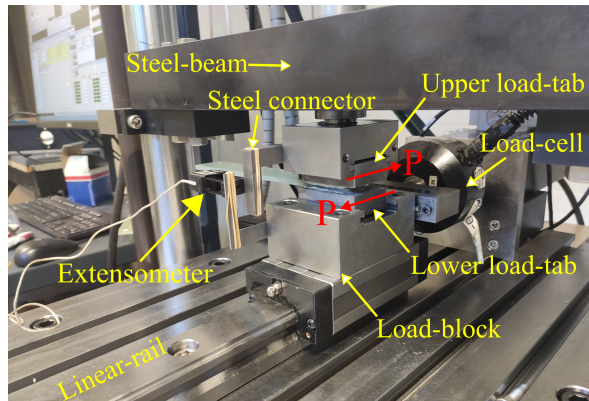

Figure 3: Overview of the test rig.

Figure 4: Test rig.

The upper load-tab is connected rigidly to the vertical actuator. Therefore, displacements and rotations of the surface of the upper load-tab are fully fixed. Instead, the lower load tab is capable of translating along the Y-axis (see fig. 5a). Thus, when the load P is applied along the Y-direction a reaction force P^R and two reaction moments M_X^R and M_Y^R act on the upper load tab (see fig. 5a). Fig. 5b shows the force and moment loads reported at the sections shear center of the two delaminated beams located at the crack front.
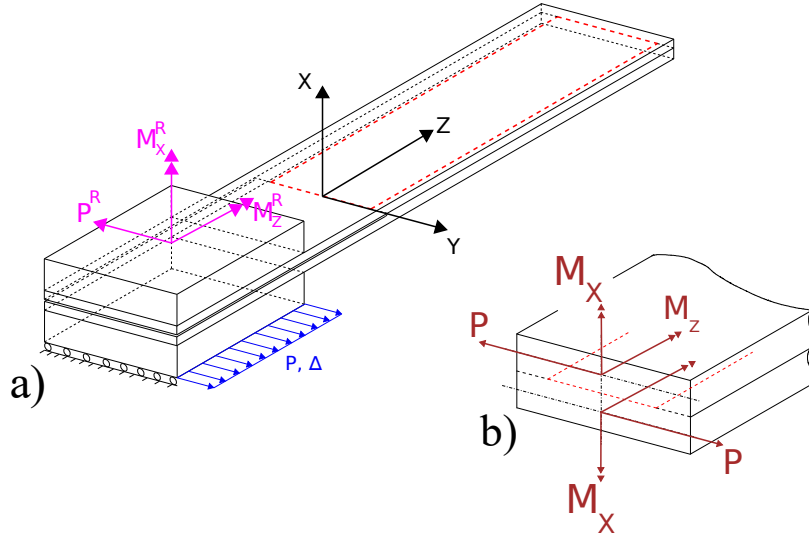
5

100

Figure 5: Illustration of the boundary conditions and load components applied to the specimen (monolithic laminate reported in the figure). a) The specimen with the external load applied to the lower load-tab (in blue) and the reaction force and moments on the upper load tab (purple) and b) the internal set of forces and moments acting at the crack front.

3.2. Specimens and fabrication

Two monolithic laminate and composite sandwich plates were manufactured from which specimens were sourced (fig. 6). Both plates were manufactured using a vacuum infusion process (VIP), and the the fibre volume fraction of the monolithic laminate plate was measured according to [27]. Four samples were manufactured from the laminate plate from different locations and an average fiber volume fraction of 49.6% was measured according to [27]. The curing of the laminate panels occurred at room temperatures for approximately two weeks as suggested by the data sheets provided by the resin supplier. A 350 x 500 mm plate was manufactured for the monolithic laminate specimens, and a 300 x 400 mm plate for the composite sandwich specimens (fig. 6). Figure 6 shows the location of Teflon® inserts (grey parts) to facilitate a delamination between two plies or debond between the face sheet and core. The inserts consisted of 13 μm thick Teflon® film. The plates were cured at room temperature for 2 weeks. The purple lines in fig. 6 indicate the lines along which cuts were made, using water-jet technology, to partition the specimens. The dimensions reported in fig. 6 should be considered as nominal without design tolerances. The nominal geometric dimensions of the monolithic laminate and the composite sandwich specimens are reported in tab. 1. The initial crack length is different in the sandwich specimen compared to the monolitic specimen for the following reason: longer delaminated arms are needed in the sandwich specimen in order to satisfy the assumptions originating from modelling the lower cracked arm as a composite beam (see [26]). The specific geometrical parameters of the individual specimens varied only slightly (+/- 0.5 mm) with respect to the nominal values in tab. 1.

The monolithic laminate plate consisted of 8 quadriaxial plies of Devold® glass fiber crimp woven fabric infused with the Pro-Set® INF-114 epoxy resin. The composite sandwich face sheets were made of the same glass fiber fabric and epoxy resin used for the monolithic laminate. The lay-up sequence for the monolithic laminate is $[(0/45/90/-45)_4||(0/45/90/-45)_4]$ where the symbol || designates the Teflon® insert. The composite sandwich specimens have the following lay-up configuration $[(0/45/90/-45)_4/Core/(0/45/90/-45)_4]$. The core is made of the open-cell H-series PVC foam manufactured by Diab® having a density of 80 $[kg/m^3]$. Additional sandwich specimens, also with a PVC H-series foam core but with a density of 45 $[kg/m^3]$ and a lay-up sequence $[(0/45/90/-45)_4/Core/(0/45/90/-45)_4]$, were also tested.
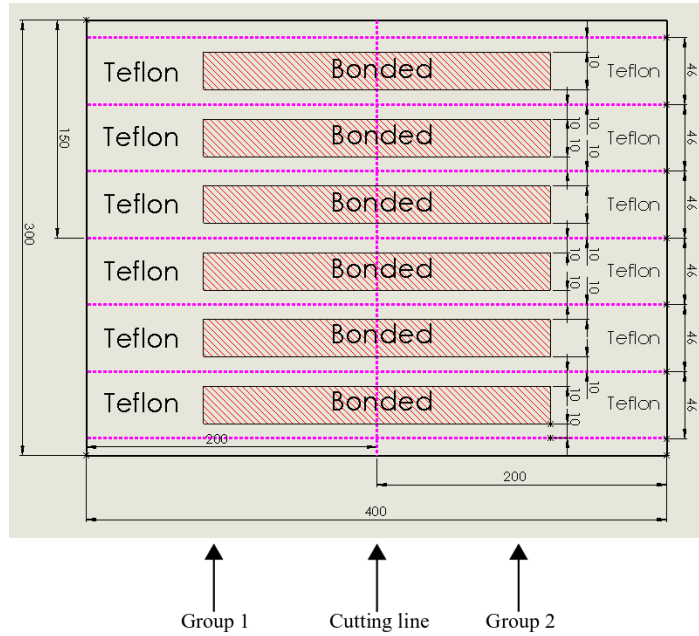
6

101

Figure 6: Example of plate layout used for manufacturing sandwich specimens.

Geometry [mm]						
	t_f	t_c	a	b	W	L
Laminate	2	-	30	36	24	230
Sandwich	2	20	40	46	26	200

Table 1: Nominal geometrical parameters of the monolithic laminate and composite sandwich specimens. The parameters reported in the table symbolize the following geometrical dimensions: t_f is the semi-laminate and face-sheet thickness of the sandwich specimens, t_c is the core thickness, a is the crack length, b is the total specimen width, W is the width of the un-cracked specimen part, L is the specimen length.
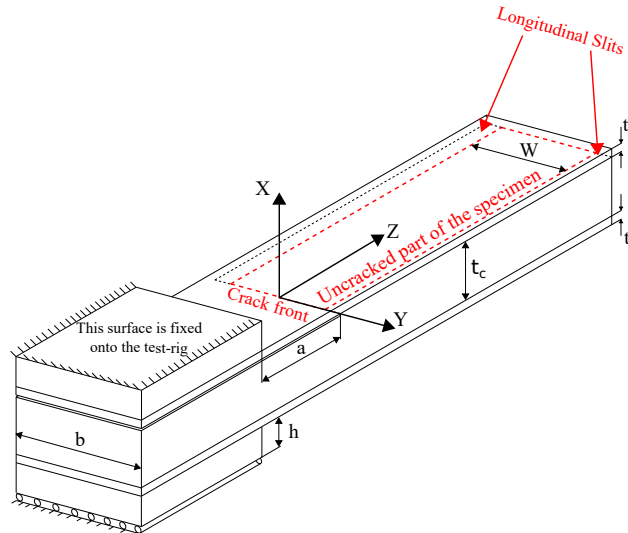

Figure 7: Sandwich specimen with the geometrical dimensions reported in tab. 1

7

The lay-up chosen for the monolithic laminate and for the sandwich face sheets is neither balanced nor symmetric. Therefore, the twist-bending coupling terms are non-zero for a quasi-isotropic lamina having a $(0/45/90/-45)_n$ lay-up. Nevertheless, the twist-bending coupling terms of the ABD matrix (D_{16} and D_{26}) become quite small when the number of plies is ≥ 16. No plate warpage was observed during the curing phase of the plate or during cutting.

The material properties of the laminate and sandwich face sheets are reported in tab. 2 and they were measured from mechanical tests following ASTM standards [28–30]. Two separate laminates have been manufactured in order to measure the properties reported in tab. 2. The first laminate (3 mm thick) has been used to cut out specimens for measuring in-plane Young's elastic moduli and Poisson ratio (E_{YY} E_{ZZ}, ν_{YZ} and G_{YZ}) following [28, 29]. The second laminate (19 mm thick) has been used to cut out specimens to measure the out-of-plane shear modulus G_{XY} following [30]. The identity has been set $G_{XZ}=G_{XY}$ due to the quasi-isotropic lay-up. The out-of-plane Young's modulus E_{YY} and Poisson ratios ν_{XY} and ν_{XZ} were measured not following a standard measuring procedure. A 19x19x19 mm block (cut out from the manufactured thick laminate) was subjected to a compressive load. Longitudinal and transverse (with respect to the load direction) strains were measured during the compression test in order to compute E_{YY}, ν_{XY} and ν_{XZ}. According to theory, $\nu_{XY}=\nu_{XZ}$ since the lay-up of the laminate. The difference observed between ν_{XY} and ν_{XZ} (in table 2) could be the consequence of inaccuracies in the measurement of the transverse strains on the 19x19x19 mm block. The mechanical properties for the PVC foam core were taken from the manufacturer catalogue [31] and the load tabs are made of C40 structural steel.

	E_{YY}	E_{ZZ}	G_{XY}	G_{XZ}	G_{YZ}	ν_{XY}	ν_{XZ}	ν_{YZ}
Elastic moduli [GPa]	19.8	19.8	2.9	2.9	7.5	0.43	0.37	0.32
Nr. Specimens	5	5	5	5	-	5	5	5
CV [%]	3.3	5.0	7.8	7.8	1.7	13.5	10.1	1.3

Table 2: Laminate material properties measured experimentally with their coefficient of variation, see fig. 7 for axes directions. X direction is through the laminate thickness, instead Y and Z are in the laminate plane.

Material	Elastic Moduli [GPa]						Poisson ratios		
	E_{XX}	E_{YY}	E_{ZZ}	G_{XY}	G_{XZ}	G_{YZ}	ν_{XY}	ν_{XZ}	ν_{YZ}
Core H80	0.095	0.095	0.095	0.035	0.035	0.035	0.4	0.4	0.4
Core H45	0.055	0.055	0.055	0.015	0.015	0.015	0.4	0.4	0.4
Load-Tabs	200	200	200	77	77	77	0.3	0.3	0.3

Table 3: Core and load tab material properties.

3.3. Specimen geometry and sizing

The monolithic laminate and the sandwich specimens include two longitudinal slits on the sides as illustrated in fig. 7. The longitudinal slits were created by using a specific pattern for the Teflon insert as shown in fig. 6. The presence of the side slits is needed in order to mitigate the free-edge influence on the mode-III energy release rate distribution along the crack front as it is discussed in [26]. The longitudinal side slits have already been used in the literature and their influence on the energy release rate distribution is accurately studied in [21] for monolithic laminates. The mode-III energy release rate component trend is studied along the crack front for different widths of the longitudinal slits for monolithic laminates in [21]. The width of the longitudinal slits has been chosen using the study done in [21]. The width of the slits is sized, for composite sandwich specimens, using the FE model and the numerical technique documented in [26].

Fig. 8 shows for the H80 cored specimens how the ratio between the mode III component of the energy release rate G_{III} and the total energy release rate G_{tot}, varies along the crack front when two different widths for the longitudinal slits are used (fig. 7). The parameter β is defined as the ratio between the width of the slits and the total specimen width, $\beta = (b - W)/2b$ (see fig. 7). A value of

8

$\beta = 1/5$ has been chosen both for the sandwich specimen having the H80 and H45 core in order to have a dominant G_{III} component along the crack front. In fact, using $\beta = 1/5$ the ratio G_{III}/G_{tot} is equal to 0.87 at the specimen edges.
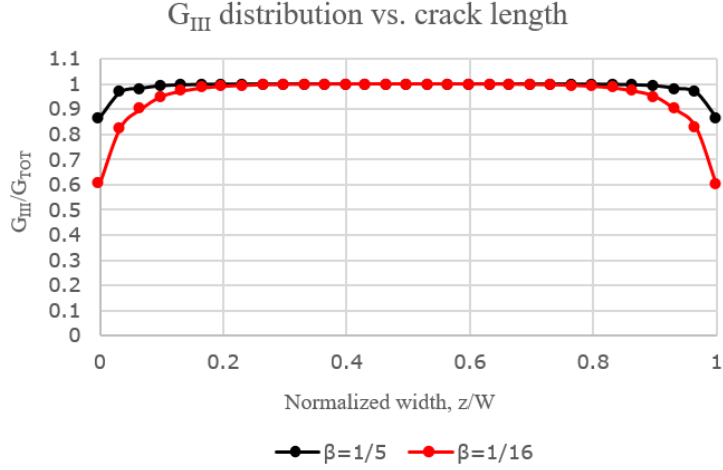

Figure 8: Effect of the side slits ratio on the energy release rate distribution along the crack front for a sandwich specimen having a H80 core.

3.4. Test procedure

A compliance calibration of the text fixture was carried out inserting a stiff steel block between the upper and lower load tabs. The compliance of the rig was then subtracted from the total compliance measured for each performed test. All tests were carried out quasi-statically in displacement control at a loading rate of 0.5 mm/min. The horizontal applied force P and fixture displacement δ were recorded throughout each test at a frequency of 3 Hz.

3.5. Data reduction method

A representative force-displacement curve obtained for the monolithic laminate specimens is shown in fig. 9 as the black curve. The four load levels taken into consideration are:

- P_{Onset} The load at which the onset crack propagation can visually be observed during the experimental tests;

- P_{NL} The load value at which the load vs. displacement curve starts to deviate from linearity

- $P_{5\%}$ The load point where the compliance has increased by 5%;

- P_{MAX} is the maximum load recorder during the tests.

The initial slope of the experimental curve used to calculate the compliance was calculated for a load in the range of $250 - 500\ N$, and P_{NL} is calculated following the procedure outlined in Appendix A.
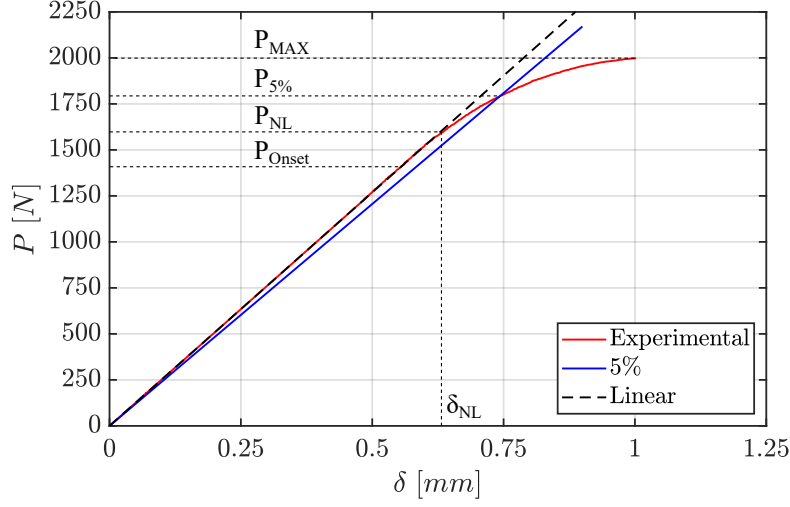
9

Figure 9: Force vs. displacement curve for a monolithic laminate specimen subjected to out-of-plane shear loads. The picture shows the different loads used to compute the critical value of the energy release rate for crack propagation.

The critical value for energy release rate is then calculated substituting P_{Onset}, P_{NL}, $P_{5\%}$ and P_{MAX} to P into the expression for G found for the monolithic laminates in [26]:

$$G_{LAM} = \frac{P^2}{WG_f A_f \kappa_d} + \frac{P^2 a^2}{4WE_f I_f} \frac{(ak_r + 2E_f I_f)^2}{(ak_r + E_f I_f)^2} + \frac{(M_z(z=a))^2}{WD} \frac{(1-e^{2ac})^2}{(1+e^{2ac})^2}. \tag{1}$$

and the composite sandwich specimens:

$$\begin{cases} G_{SAN} = G_d + G_s \\ G_d = \frac{P^2}{2WG_f A_f \kappa_d} + \frac{P^2 a^2}{8WE_f I_f} \frac{(ak_r^d + 2E_f I_f)^2}{(ak_r^d + E_f I_f)^2} + \frac{(M_z^d(z=a))^2}{2WD_d} \frac{(1-e^{2ac_d})^2}{(1+e^{2ac_d})^2} \\ G_s = \frac{P^2}{2W(GA)_s} + \frac{P^2 a^2}{8W(EI)_s} \frac{(ak_r^s + 2(EI)_s)^2}{(ak_r^s + (EI)_s)^2} + \frac{(M_z^s(z=a))^2}{2WD_s} \frac{(1-e^{2ac_s})^2}{(1+e^{2ac_s})^2}. \end{cases} \tag{2}$$

Both expressions have been derived and presented in [26] and all the parameters are defined in appendix B.

The crack propagation was monitored from the top of the specimen both for the monolithic laminates and for the sandwich specimens. The transparency of the glass fibre laminate and sandwich face sheets allows visual monitoring of crack advance. It was not possible to detect the crack propagation from the side of the specimens (as it is usually done for other fracture tests such as in [32]), because the crack front is embedded in the specimen, and the crack edges are not visible from the specimen sides.

The crack propagation increment Δa is measured along the specimen width as it is shown in fig. 10. The parameter Δa is measured as the average distance (between the distances Δa_1, Δa_2, $\Delta a_n...\Delta a_{n+1}$) since the crack front shows for all the tested specimens a curved crack front as it is shown in fig. 10.

Figure 10 shows a characteristic shape of the crack front after propagation. This characteristic shape is concave and it was also observed in [21], in monolithic carbon fiber laminates, where it is defined an *inverted thumbnail* shape. At the crack corners a mixed mode II/III state is present and the distribution of the total energy release rate G_{Tot} presents its peak values (as reported in [21, 26]). Therefore, these peak values of G_{Tot} are responsible for the quicker crack propagation at the corner crack locations with respect to the central part of the crack front.
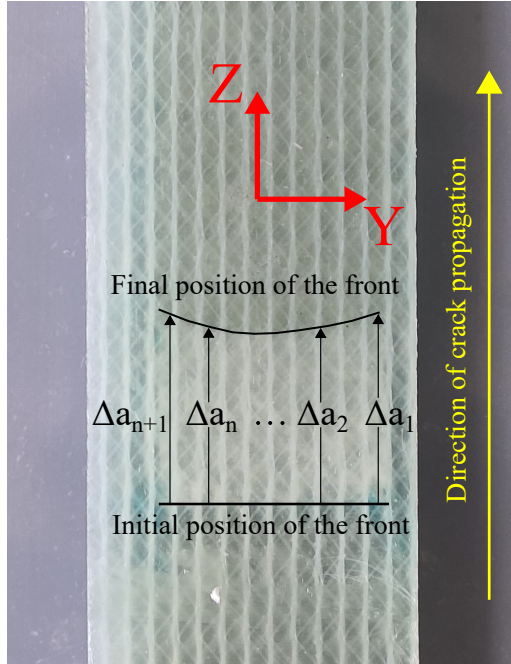
10

Figure 10: Top view of a cracked monolithic laminate specimen. The total crack length is computed as the average of the through-the-width distances between the Teflon® insert and the final position of the crack front.

4. Results and discussion

4.1. Experimental tests and results for the monolithic laminate specimens

The monolithic laminate specimens have been tested with a single crack propagation run per specimen. All specimens had the same initial crack length $a_0 = 30$ mm. After each propagation of the crack front, the specimen is unloaded and the crack propagation length $\Delta a = a_f - a_0$ (where a_f is the crack length after propagation) is measured. Seven monolithic laminate specimens were tested.

Figure 11 illustrates the load vs. displacement curves for the seven monolithic laminates specimens tested. The plots report the point where the onset of crack propagation is observed through a visual inspection of the specimen. The crack propagation length for each specimen is different because the specimens were unloaded at different propagation lengths.

All curves presented in fig. 11 exhibit a linear trend in the first loading phase until around 1300-1800 [N]. A stable crack propagation was observed for all specimen tested. The laminate is quasi-isotropic in the laminate plane (YZ plane in fig. 10). This multidirectional lay-up has been chosen in order to inhibit the propagation of intra-laminar cracks as it is suggested in [33]. Hence, the primary damage mode should be the advance of the original crack front. Moreover, it was visually observed that the crack propagated on the plane of the pre-implanted Teflon® insert without macroscopic kinking into other laminae as it was noticed in [33].

11

(a) Specimen 1

(b) Specimen 2

(c) Specimen 3

(d) Specimen 4

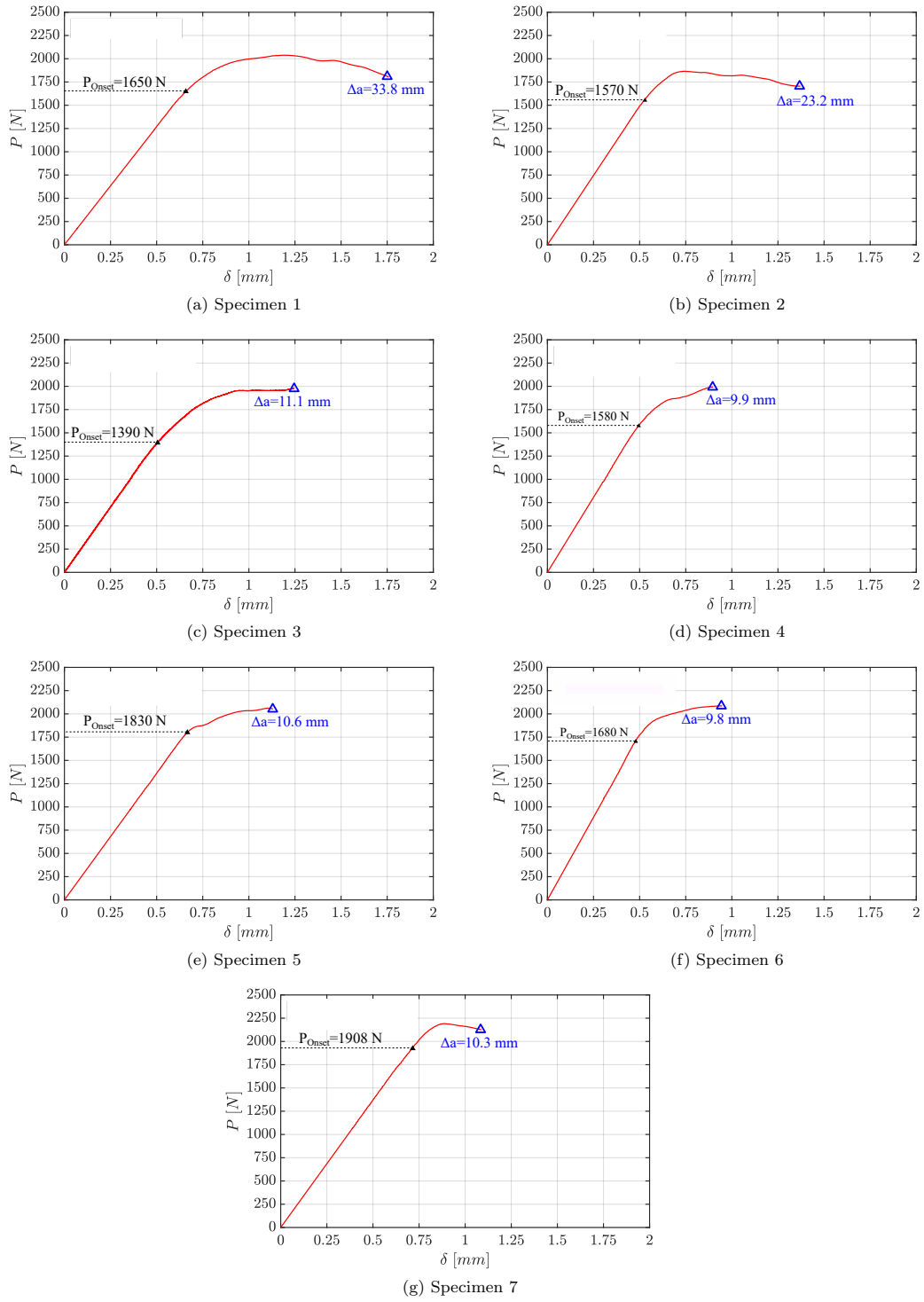(e) Specimen 5

(f) Specimen 6

(g) Specimen 7

Figure 11: Experimental load vs displacement curve plots of the monolithic laminates specimens tested. P_{Onset} and the final crack propagation length $\Delta a = a_f - a_0$ are reported in each plot. The initial crack length is set $a_0 = 30mm$ for all the specimens.

12

107

The critical load points P_{NL}, $P_{5\%}$, P_{MAX} and P_{Onset} are reported in tab. 4. All the three critical loads P_{NL}, $P_{5\%}$ and P_{MAX} have a coefficient of variation which is lower than 10%. P_{MAX} has the lowest coefficient of variation (CV). $P_{5\%}$ has the highest CV. Usually, P_{NL} marks the deviation from linearity in the load vs displacement curve and therefore P_{NL} is the load level at which damage (i.e. crack advance) starts to initiate in the specimen. In fact, the onset of crack propagation (from visual inspection) was observed at a load level equal to P_{Onset} and the relative difference between P_{Onset} and P_{NL} is lower than 4%.

Specimen	$P_{5\%}$ [N]	P_{max} [N]	P_{NL} [N]	P_{Onset} [N]	$(P_{Onset} - P_{NL})/P_{NL}$ [%]
1	1790	2038	1623	1650	1.6
2	1730	1865	1558	1570	0.8
3	1550	1979	1347	1390	3.2
4	1710	1992	1556	1580	1.5
5	1865	2061	1811	1830	1.1
6	1915	2086	1652	1680	1.7
7	2150	2191	1840	1908	3.7
Average [N]	1816	2030	1627	1658	-
Std [N]	174.8	93.6	154.9	159.6	-
CV [%]	9.6	4.6	9.5	9.6	-

Table 4: P_{NL}, $P_{5\%}$, P_{MAX}, P_{Onset} and the relative difference between P_{Onset} and P_{NL} are computed for each monolithic laminate specimen along with their average, standard deviation (Std) and coefficient of variation (CV). The initial value for the crack length is $a_0 = 30\ mm$ for all the specimens, see figs. 9 and 11.

Specimen	$G_c^{5\%}$	G_c^{max}	G_c^{NL}	G_c^{Onset}	$(G_c^{Onset} - G_c^{NL})/G_c^{NL}$
-		[J/m^2]			[%]
1	483	626	397	410	3.3
2	447	519	362	368	1.6
3	518	844	391	416	6.4
4	463	629	384	396	3.2
5	620	757	584	596	2.0
6	615	730	458	473	3.4
7	766	796	561	603	7.5
Average [J/m^2]	559	700	448	446	-
Std [J/m^2]	115	114	90	96	-
CV [%]	20.5	16.2	20.1	20.7	-

Table 5: The critical values of the energy release rate $G_c^{5\%}$ G_c^{max}, G_c^{NL}, G_c^{Onset} by inserting $P_{5\%}$, P_{MAX}, P_{NL}, P_{Onset} (tab. 4) into eq. 1 are reported.

Table 5 reports the critical values for the energy release rate computed by inserting $P_{5\%}$, P_{MAX}, P_{NL}, P_{Onset} into eq. 1. The critical energy release rate that shows the highest average value is G_c^{max} (700 [J/m^2]) followed by $G_c^{5\%}$ (559 [J/m^2]) and G_c^{NL} (448 [J/m^2]). G_c^{max} has the lowest coefficient of variation of 16.2 %, and $G_c^{5\%}$ has the highest CV equal to 20.5 %. G_c^{Onset} is also reported and its maximum relative difference with respect to G_c^{NL} is 7.5 %. G_c^{Onset} corresponds to the delamination initiation from the insert and therefore it cannot be affected by non-linear effects, such as fiber bridging.

The high scatter (high coefficient of variance) in the values for the critical energy release rates G_c^{max} shows how the length of crack propagation Δa has an effect on the value of the critical energy release rate.

The four different load values (among $P_{5\%}$, P_{MAX}, P_{NL}, P_{Onset}) chosen for fracture toughness computation present different characteristics relatively to the computation of mode III fracture toughness. G_c^{Onset} and G_c^{NL} are influenced by the presence of the artificial crack tip formed using the Teflon

13

insert. $G_c^{5\%}$ and G_c^{max} are more representative of the propagation of the crack with a sharp tip, since the crack front is far away from the Teflon insert. Therefore, $G_c^{5\%}$ and G_c^{max} could be considered the most representative of the mode III fracture toughness. The average value of $G_c^{5\%}$ is more conservative with respect to the average value of G_c^{max}. Thus, $G_c^{5\%}$ is suggested here to be used as representative of the mode III fracture toughness. However, a larger data set from more tested specimens may improve the statistical decision making, so that several or all load values identify the same load level. Furthermore, the effect of the micro-mechanical shape of the Teflon-dominated initial crack front may have an influence on the onset of crack propagation.

4.2. Experimental tests and results for sandwich composite specimens

The same experimental procedure employed for the monolithic laminate specimens has been used for the composite sandwich specimens. An initial crack length of $a_0 = 40 \ mm$ was used for all specimens tested. Eight specimens with a Divinycell® H80 core and two H45 specimens were tested. The specimens with the H80 core were pre-cracked because often in PVC foam cores with an artificial Teflon®-filmed debond, the artificial Teflon® insert forms a crack tip which is usually composed of partially resin filled core cells. This will create an artificial tough region at the crack front, which acts like a barrier for initiation of crack propagation and the onset of crack propagation could not be observed. In order to break this tough region and to perform pre-cracking (see fig. 12), the specimen were installed in the test fixture, but only the vertical actuator was applied in order pre-crack the specimen with a mode-I dominant loading. Initially, pre-cracking was performed by applying: a sinusoidal cyclic load with an amplitude of 10-15 % of the static mode-I propagation load, and with a load ratio $R = 0.1$ and a frequency of 3 Hz, until a propagation of $2 \pm 0.5 \ mm$ was observed. The amplitude was however increased up to 35 % of the static propagation load when crack growth was not observed. This increase in amplitude was applied to 6 specimens out of 8 (with the H80 core) in order to pre-crack the specimens. The length of the new crack after propagation was measured with the method illustrated in fig. 10.

The experimental load vs displacement curves showed a rather strong non-linear behaviour as shown in appendix C fig. 21. A representative experimental curve (calculated as the average of the experimental curves corresponding to the specimens with the H80 core) is shown in figure 13. Moreover, a macroscopic crack propagation was not visible throughout the loading phase during the experiment. Hence, the data reduction method developed in section 4.1 cannot be used to extract a critical value for the energy release rate. In fact, the two main assumptions required to apply eq. 2 are not satisfied: the specimen response is neither linear nor onset of crack propagation can be observed during the experiments. Therefore, the non-linear behaviour in fig. 13 must be considered as a consequence of a damage mechanism in the specimen which dissipates energy when the load P is applied. Two different hypotheses were proposed in order to justify the non-linear behaviour showed in fig. 13: (i) either a large-scale damage process zone (i.e. formation of secondary cracks in the core) is present at the crack front (see fig. 12) or (ii) the foam core behaves in a non-linear manner under the shear and torsional load applied , which is the case when H-series foam core material is subjected to high shear strain magnitudes [34]. In order to verify these two hypotheses, two investigations were carried out.
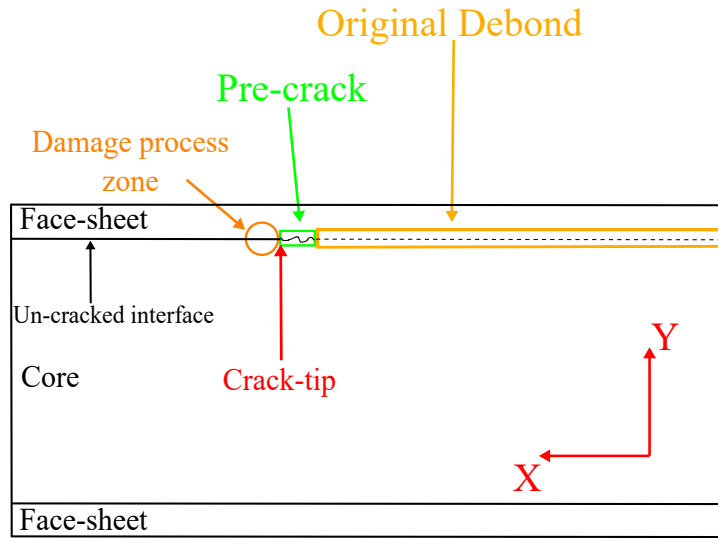
14

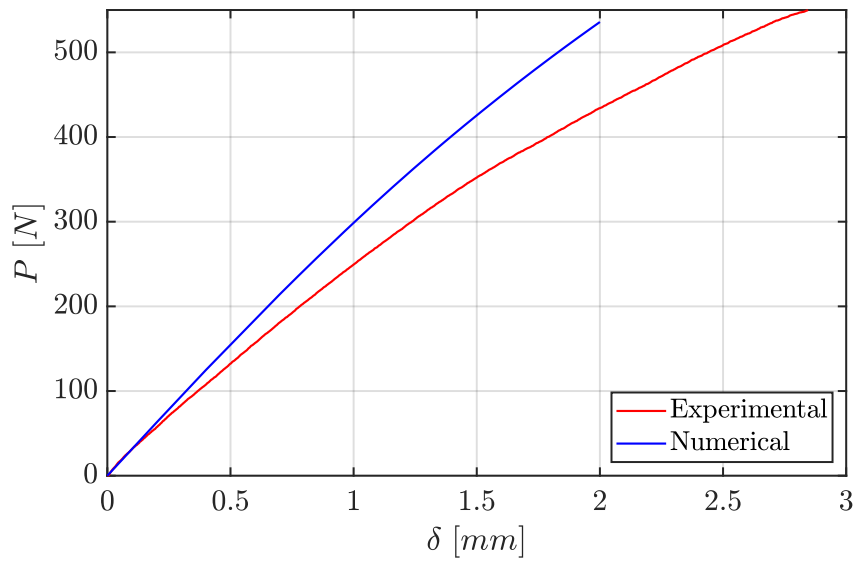Figure 12: Crack front detail of a cracked sandwich specimen.

Figure 13: Average experimental and numerical force vs. displacement curves for H80 specimens having quasi-isotropic face sheets and a Divinycell® H80 core ($[(0/45/90/-45)_4/Core/(0/45/90/-45)_4]$) subjected to out-of-plane shear loads. The initial crack length is set $a_0 = 40mm$.

PVC foams can exhibit a non-linear relationship between stresses and strains in shear loading, as reported in [34]. Therefore, the same FE model described and documented in [26] has been modified in order to adopt non-linear material behaviour of the foam core in shear with no damage modeling. The shear stress/strain curve, taken from [35], is converted into a tensile stress/strain curve following the procedure outlined in [35] for the H80 PVC foam used in the experimental setup. The methodology

15

110

proposed in [35] assumes a von-Mises based criterion to model the yielding response of a closed cell foam. The load vs. displacement curve computed from the FE model is presented in fig. 13 along with the experimental curve. Fig. 13 shows that the numerical results also predict a non-linear response of the specimen subjected to the same load levels applied during the fracture characterization testing. The experimental curve (see fig. 13) deviates significantly from the numerical results (the relative difference is 21 % at $\delta = 1\,mm$). Hence, the contribution to the total non-linear experimental behaviour (fig. 13) could be a combination of a non-linear material behaviour of the foam itself as well as the presence of large-scale damage at the crack front region.

All foam cored sandwich specimens were investigated by destructive inspection after load application, in order to investigate whether damage was visible at or near the crack front. Each specimen was cut along the plane represented in fig. 14a. The distance d (along the Y-axis, see 14a) between the plane of cutting and the crack plane was 2 mm. Fig. 14b illustrate that multiple cracks are present just below the face-sheet/core interface embedded in the core. The presence of these cracks in the core could be associated to either the kinking of the initial debond front into the core, or to a damage mechanism similar to the one observed and described for monolithic laminates in [33]. In the latter case, the intra-laminar cracks observed in [33] can be related to the core-cracks observed herein. Further studies are necessary to investigate the cause of the initiation of these embedded core-cracks appearing under pure mode III loading, as mode III crack mechanisms in foam cored sandwich specimens are not currently reported in the open literature.
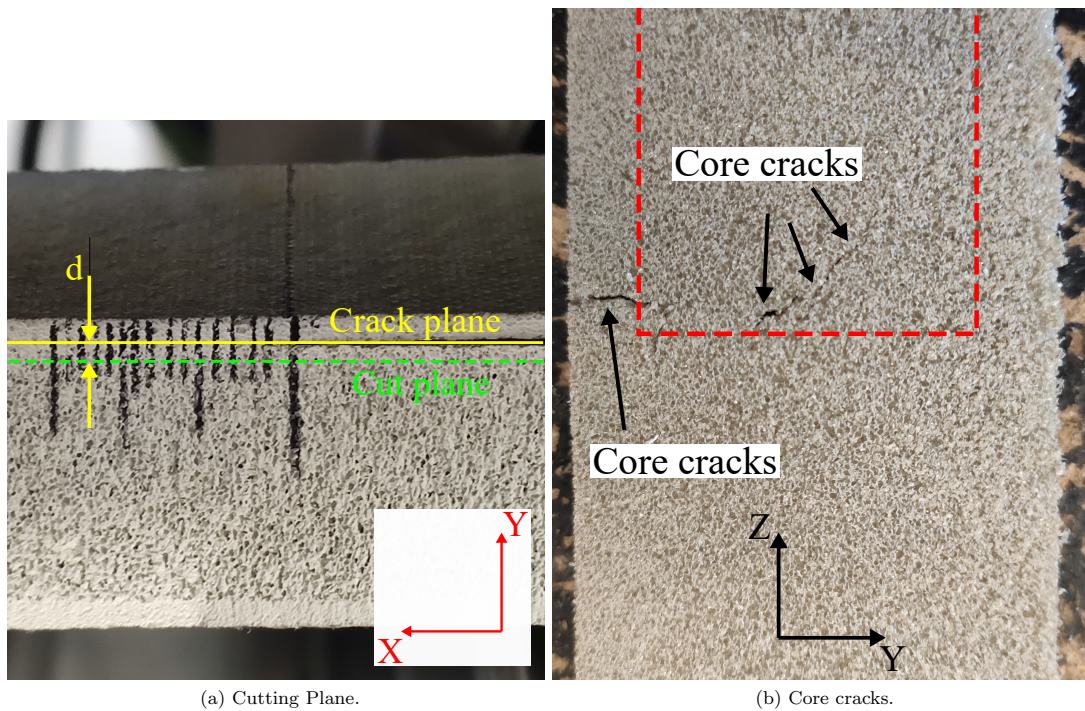

(a) Cutting Plane. (b) Core cracks.

Figure 14: The plane of cut and core cracks are shown.

The sandwich specimens with a H45 core were additionally tested in order to understand if a specimen with a more brittle core, compared to the H80 core, was showing a less non-linear behaviour.
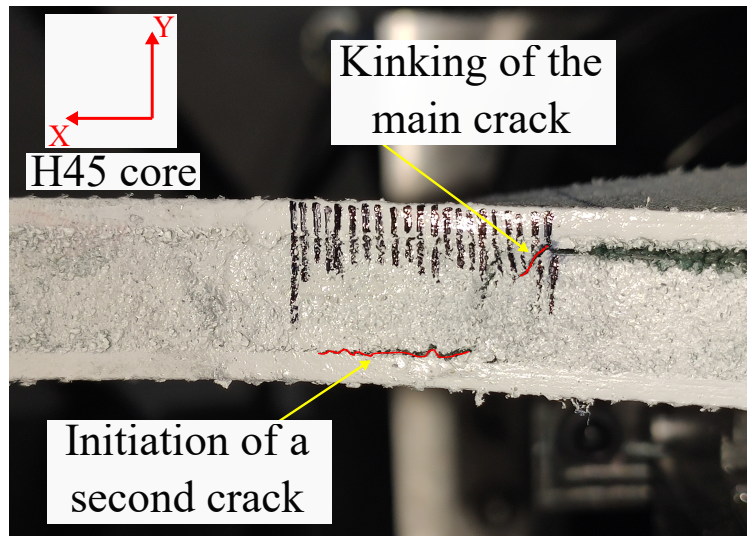
16

Figure 15: Crack front detail of a cracked H45 sandwich specimen.

Fig. 15 illustrates one of the tests done on the H45 cored specimens. The picture is representative of the crack propagation behaviour of all the specimens having an H45 core. The crack kinks into the core and initiation of secondary cracks is present between the core and the lower face sheet. The low shear strength value (0.56 MPa) of the H45 cores makes this kind of mode III fracture characterization test not suitable for sandwich specimens.

4.3. Stress distribution in front of the crack tip

A linear elastic FE model has been defined in order to investigate the distribution of stresses in front of the crack. The magnitude of the stresses in a region close to the crack tip can be the cause of the core cracks observed in fig. 14b. The FE model is identical to the one used in [26] and it reproduces the specimen geometry and loads applied by the test fixture. The model is defined in 3D, is linear elastic and is built in Abaqus®, where the 3D solid element C3D8R is used. The sandwich face sheets are modelled as homogeneous and orthotropic material. The core is represented as homogeneous and isotropic. Therefore, the maximum principal stress σ_1 has been selected as an indication of the main stress component driving the initiation of the core cracks in fig. 14b. The mesh close to the crack tip, the paths (along the z axis) used for the extraction of σ_1 and the definition of the angles with respect to the coordinate system axes are shown in fig. 16. The smallest element size used is equal to 0.1 mm. Three paths have been selected at the following coordinate positions, with the coordinate z varying along the width of the specimen: (0.375, -0.375, z), (0.75, -0.75, z) and (2, -2, z), defined in mm. The location of these paths have been chosen close to the crack front where the core cracks were observed in the specimen (see fig. 14b). All the extracted results for σ_1 are corresponding to an applied load $P = 97\ N$ (for H45 core) and $P = 164\ N$ (for H80 core).
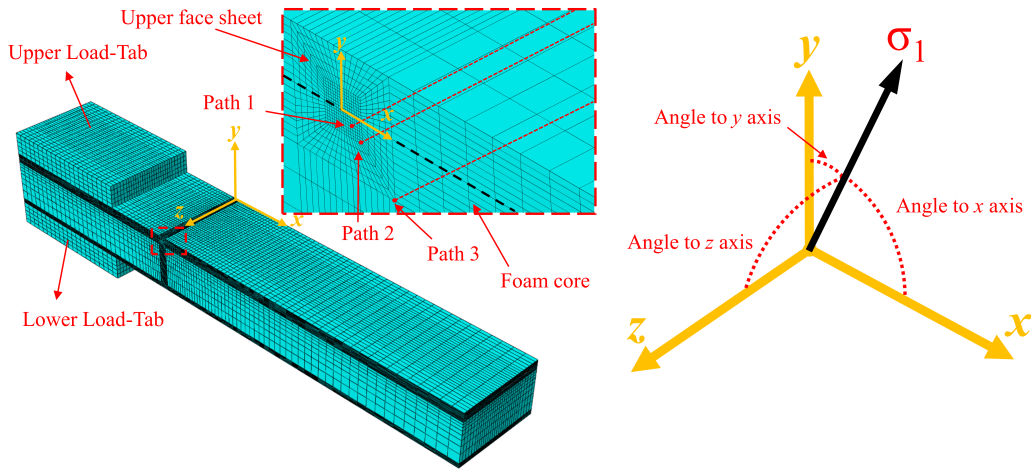
17

112

Figure 16: Illustration of the FE model along with the three paths used for extraction of stresses and the definition of the angles between the coordinate system reference axes and the maximum principal stress σ_1.

Figure 17 is reporting the orientation of the maximum principal stress σ_1 with respect to the coordinate system axes along the three paths illustrated in fig. 17. It can be seen that in the central part of the specimen along path 3 (where the crack front is embedded in the specimen between 15 to 25 mm) the orientation of σ_1 remains constant and equal to 135°.

(a) H45   (b) H80
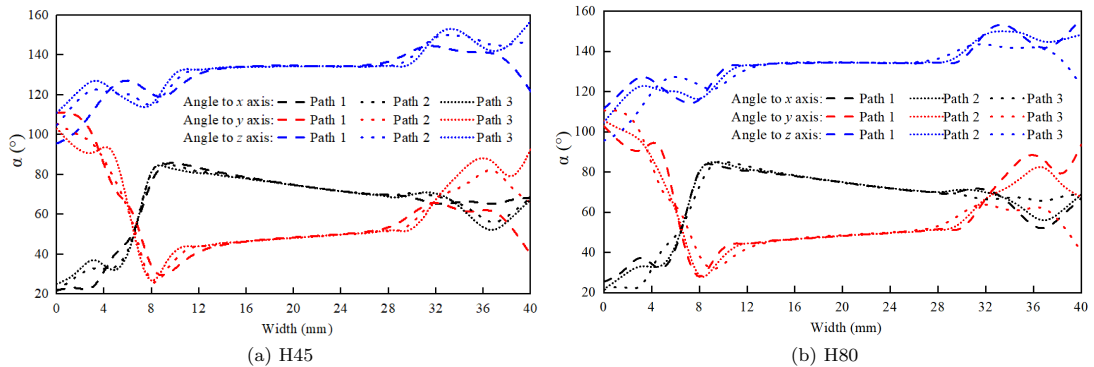
Figure 17: Orientation of the maximum principal stress σ_1 respect to the coordinate system axes along the selected paths for the two different core materials (H45 and H80).

The local magnitudes of σ_1 along the z-axis (width of the specimen) have also been extracted along the three different paths (see fig. 18). It can be seen that the absolute magnitudes of σ_1 (in the central portion of the specimen where the crack front is located) are almost constant. Two additional paths (4 and 5, defined in fig. 18a) were also selected closer to the crack front in order to monitor the magnitudes of σ_1 in the crack tip region. Fig. 19b shows a plot of the maximum value of σ_1 vs. the external applied load P for paths 4 and 5. Figure 19b clearly shows that the maximum value of σ_1 exceeds the tensile strength of the core for stresses calculated for values of $P = 97 \ N$ (for H45 core) and $P = 164 \ N$ (for H80 core). These magnitudes of σ_1 exceed the tensile strength of the core at the load levels investigated, both for H45 and H80 cored specimens (see tab. 6). Hence, the early appearance (during the loading phase) of the core cracks (see fig. 14b) could be explained by the maximum values of σ_1 exceeding the tensile strength of the H45 and H80 core materials. This behavior is also confirmed

18

113

by the study reported in fig. 13.
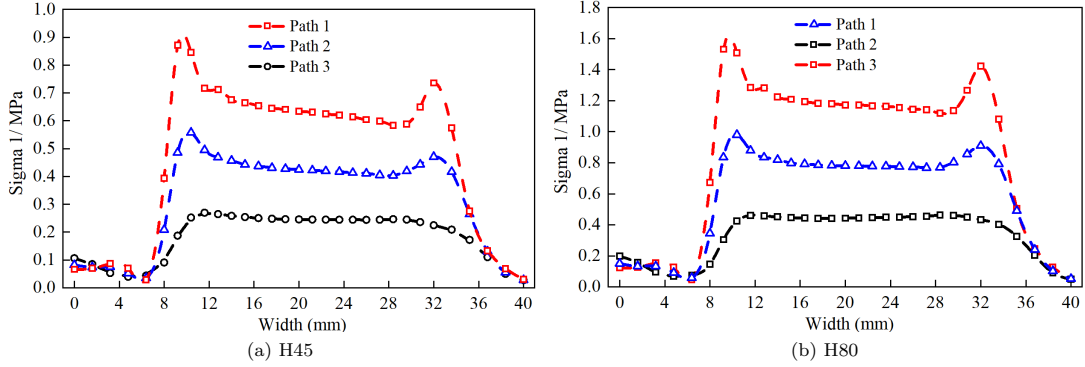

(a) H45

(b) H80

Figure 18: Distribution of the maximum principal stress σ_1 the selected paths for the two different tested core materials (H45 and H80).

Core type	H_{45}	H_{80}
Tensile strength [MPa]	1.4	2.5

Table 6: Core tensile strengths taken from [31]

(a) FE model

(b) σ_1 vs applied force P
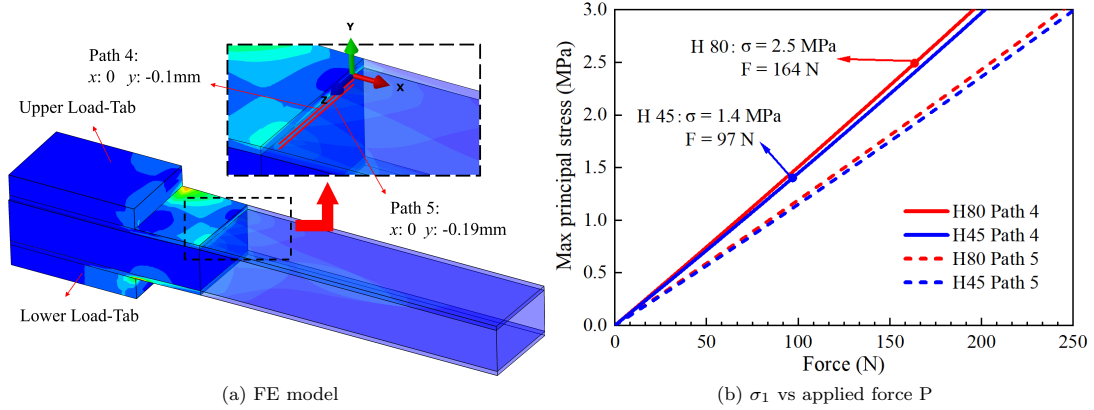
Figure 19: (a) shows the paths 4 and 5 along which σ_1 is extracted and (b) illustrates the relationship between the maximum value of σ_1 extracted along the paths in (a) and the external applied force P.

5. Conclusions

This manuscript presents a pilot experimental campaign on mode III fracture characterization testing of monolithic laminates and foam-cored sandwich specimens. The monolithic laminates exhibited a linear elastic behaviour until onset of crack propagation. Furthermore, it was observed that the crack propagates along the initial delamination plane. Hence, the analytical linear elastic fracture mechanics (LEFM) expressions developed in [26] were applied to extract the critical value of G (the fracture toughness) at different selected experimental load levels. The foam cored sandwich specimens with

19

an H80 core showed a strong non-linear behaviour in the load vs. displacements plots and no crack propagation was visible during the experiments. While, the specimens having an H45 core exhibited kinking of the crack into the core along with the appearance of secondary cracks between the core and the lower face sheet.

The non-linear material behaviour (under shear loading) of the PVC foam core material and the presence of large-scale core cracks in front of the crack tip were identified as possible causes of the non-linear specimen response. Thus, the LEFM assumptions (linear elastic behaviour and planar propagation of the main crack along the face/core interface plane) under-pinning the analytical model in [26] are violated in the case of the sandwich specimen and consequently the application of the data reduction method cannot directly be applied for PVC foam cored specimens loaded in pure mode III. More research is necessary to understand the nucleation of large-scale crack tip cracking under mode III loading and thus investigate to which extend mode III crack propagation of sandwich face/core debonds are at all possible and important to consider in practical engineering design of sandwich structures.

Finally, an improved, novel test fixture inspired by the STB mode I/II/III fixture presented in [36] was presented for pure mode III fracture characterization of the initiation fracture toughness in monolithic laminates and composite sandwich specimens, along with an improved STB specimen design with side slits and sizing. The main novelties presented, respect to the fixture presented in [21]), are related to the testing of sandwich composite specimens and to the use of an improved data reduction method presented in [26]. Although, a big scatter was observed in the mode III fracture toughness values for the monolithic laminate specimens, due to a limited amount of specimens tested. The novel test fixture performed well and the data reduction method yielded convincing results. The most representative load for calculation of the pure mode-III fracture toughness is suggested to be P_{Onset}. In fact, P_{Onset} is not affected by non-linear mechanisms. Conversely, the measurement of mode III interface fracture toughness values for the foam core sandwich specimens was not possible because the propagation of the initial crack along the interface plane was not successfully achieved due to appearance of secondary core cracks. The secondary core cracks influence the overall structural specimen behaviour. Thus, the real question is: is it , at all, possible to achieve pure mode III crack propagation in foam cored sandwich specimens? This preliminary work shows that in sandwich specimens having H45 and H80 foam cores it is not possible to propagate the main crack on the interface plane under pure mode III loads without the appearance of secondary core cracks. Although, it is the authors' belief that further studies and research are necessary in order to fully understand pure mode III fracture characterization of foam cored sandwich materials.

6. Acknowledgements

7. References

References

[1] S. Z., Singularities, Interfaces and Cracks in Dissimilar Anisotropic Media, Proceedings of the Royal Society of London (1990) 331–358.

[2] R. Moslemian, Residual strength and fatigue lifetime of debond damaged sandwich structures, PhD Thesis (2011) 77–80.

[3] G. Becht, J. W. Gillespie, Design and analysis of the crack rail shear specimen for mode III interlaminar fracture, Composites Science and Technology 31 (2) (1988) 143–157. `doi:10.1016/0266-3538(88)90088-7`.

[4] S. L. Donaldson, Mode III interlaminar fracture characterization of composite materials, Composites Science and Technology 32 (3) (1988) 225–249. doi:10.1016/0266-3538(88)90022-X.

[5] H. Martin, Evaluation of the Split Cantilever Beam for Mode III Delamination Testing, Composite Materials Fatigue and Fracture (Third Volume), ASTM STP 1110, American Society for Testing and Materials (1991) 243:266.

[6] W. C. Liao, C. T. Sun, The determination of Mode III fracture toughness in thick composite laminates, Composites Science and Technology 56 (4) (1996) 489–499. doi:10.1016/0266-3538(96)00009-7.

[7] R. J. Ehart, S. E. Stanzl-Tschegg, E. K. Tschegg, Crack face interaction and mixed mode fracture of wood composites during mode III loading, Engineering Fracture Mechanics 61 (2) (1998) 253–278. doi:10.1016/S0013-7944(98)00033-2.

[8] S. F. Hwang, C. L. Hu, Tearing mode interlaminar fracture toughness of composite materials, Polymer Composites 22 (1) (2001) 57–64. doi:10.1002/pc.10516.

[9] N. Naik, K. Reddy, S. Meduri, N. Raju, P. Prasad, B. R. SK.N.M. Azad, P.A. Ogde, Interlaminar fracture characterization for plain weave fabric composite, Journal of Material Science Vol 37 (2002) 2983:2987.

[10] H. Yoshihara, Exhamination of the 4-ENF test for measuring the mode III R-curve of wood, Engineering Fracture Mechanics 73 (2005) 42:63.

[11] A. Szekrényes, Delamination fracture analysis in the G_{II}-G_{III} plane using prestressed transparent composite beams, international journal of Solids and Structures Vol. 44 (2006) 3359:3378.

[12] M. Farshad, P. Flüeler, Investigation of mode III fracture toughness using an anti-clastic plate bending method, Engineering Fracture Mechanics 60 (5-6) (1998) 597–603. doi:10.1016/s0013-7944(98)00020-4.

[13] F. Podczeck, The determination of fracture mechanics properties of pharmaceutical materials in mode III loading using and anti-clastic plate bending method, International Journal of Pharmaceutics Vol. 227 (2001) 39:46.

[14] G. Fernlund, H. Lanting, J. Spelt, Mixed Mode II-Mode III Fracture of Adhesive Joints, Journal of Composites Technology and Research Vol. 17 (1995) 317:330.

[15] H. Li, R. Jones, J. Hirth, Mixed mode I/III fracture toughness of a V-5Cr-5Ti alloy at 100 °C, Scripta Metallurgica et Materialia Vol. 32 (1995) 611:616.

[16] S. Kamat, M. Srinivas, P. Rao, Mixed mode I/II fracture toughness of ARMCO iron, Acta Metallurgica Vol. 46 (1998) 4985:4992.

[17] V. Lazarus, J. Leblond, S. Mouchrif, Crack front rotation and segmentation in mixed mode $I+III$ or $I+II+III$. Part I: Calculation of stress intensity factors, Journal of Mechanics and Physics of Solids Vol. 49 (2001) 1399:1420.

21

[18] V. Lazarus, J. Leblond, S. Mouchrif, Crack front rotation and segmentation in mixed mode $I+III$ or $I+II+III$. Part II: Comparison with experiments, Journal of Mechanics and Physics of Solids Vol. 49 (2001) 1399:1420.

[19] S. Lee, An edge crack torsion method for mode III delamination fracture testing, Journal of composites technology and research 15 (3) (1993) 193–201. `doi:10.1520/CTR10369J`.

[20] A. Szekrényes, Improved analysis of the modified split-cantilever beam for mode-III fracture, International Journal of Mechanical Sciences 51 (9-10) (2009) 682–693. `doi:10.1016/j.ijmecsci.2009.07.005`.

[21] B. D. Davidson, F. O. Sediles, Mixed-mode I-II-III delamination toughness determination via a shear-torsion-bending test, Composites Part A: Applied Science and Manufacturing (2011). `doi:10.1016/j.compositesa.2011.01.018`.

[22] J. Ratcliffe, Characterization of the edge crack torsion test for mode iii fracture toughness measurement of laminated composites, NASA-TM 1 (213269) (2004).

[23] M. Czabaj, J. Ratcliffe, B. Davidson, Observation of intralaminar cracking in the edge crack torsion specimen, Engineering Fracture Mechanics (2014) 120:1–4.

[24] A. Horner, M. Czabaj, B. Davidson, J. Ratcliffe, Three-dimensional crack surface evolution in mode III delamination toughness tests, Engineering Fracture Mechanics (2015) 149:313–25.

[25] A. Horner, B. Davidson, Fracture surface evolution and apparent delamination toughness in split composite beam specimens subjected to mixed mode I-III loading, Composites Part A: Applied Science and Manufacturing (2015) 79:92–102.

[26] P. Sabbadin, M. Massabó, C. Berggreen, An improved analysis of a stb specimen for fracture characterization of laminates and foam-cored sandwich composites under mode iii loads, Engineering Fracture Mechanics 236 (2020). `doi:https://doi.org/10.1016/j.engfracmech.2020.107198`.

[27] ASTM, Standard Test Method for Ignition Loss of Cured Reinforced Resins, D2584-18 1–3.

[28] ASTM, Standard Test Method for Tensile Properties of Polymer Matrix Composite Materials, D3039/D3039M-17 1–13.

[29] ASTM, Standard Test Method for Shear Properties of Composite Materials by V-Notched Rail Shear Method, D7078/D7078M-12 1–15.

[30] ASTM, Standard test Method for Shear Properties of Composite Materials by the V-Notched Beam Method, D5379/D5379M-12 1–14.

[31] Diab, Divinycell H technical data sheet (2018) 1–2.

[32] ASTM, Mixed Mode I-Mode II Interlaminar Fracture Toughness of Unidirectional Fiber Reinforced Polymer Matrix Composites, D6671/D6671M-06 1–13.

[33] M. Czbaj, J. Ratcliffe, B. Davidson, Observation of intralaminar cracking in the edge crack torsion specimen, Engineering Fracture Mechanics (2014) 120–124.

22

[34] K. Branner, Capacity and Lifetime of Foam Core Sandwich Structures, Danmarks Tekniske Universitet, Institut for Skibs-og Havteknik, (1995) ISBN: 8789502329, pages 65–68.

[35] Y. Rothschild, A. Echtermeyer, A. Arnesen, Modelling of the non-linear material behaviour of cellular sandwich foam core, Composites Part A: Applied Science and Manufacturing, Volume 25, Issue 2 (1994) 111–118.

[36] P. Sabbadin, C. Berggreen, B. Legarth, Development of a mode i/ii/iii test fixture for composite laminates and sandwich face/core fracture characterization, Proceedings of 12th International Conference on Sandwich Structures 1 (1) (2018) 35–37. `doi:-`.

8. Appendix A

8.1. Calculation of P_{NL}

The calculation of P_{NL} was carried out using the following procedure:

1) A linear fit of the experimental points in the load range $250 - 500\ N$ was done. The load values lying on the linear extrapolated curve are addressed with the symbol P_{lin};

2) The relative difference between the loads from the linear extrapolated curve P_{lin} and the experimental loads P_{exp} was computed.

Fig. 20 plots the relative difference $(P_{exp} - P_{lin})/P_{lin}$ vs. the out-of-plane crack flanks sliding displacement.

3) Then, δ_{NL} is chosen as the displacement at which the relative error $(P_{exp} - P_{lin})/P_{lin}$ exceeds 0.5%;

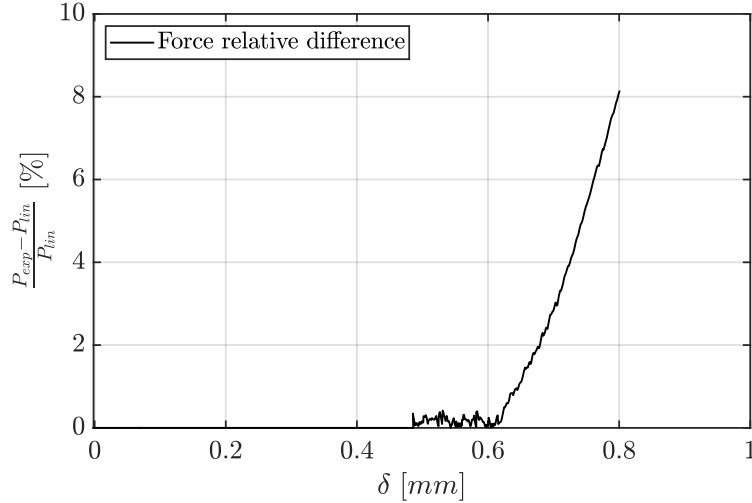4) P_{NL} is the load that corresponds to δ_{NL} on the experimental curve in fig. 9.

Figure 20: The vertical axis represents the relative difference between the experimental applied load P_{exp} and the load relative to the linear curve in fig. 9. The horizontal axis shows the out-of-plane crack flanks openings

23

9. Appendix B

The definition of the parameters appearing in eqs. 1 and 2 are reported below:

- a Crack length.

- b Specimen width.

- t_f Half monolithic laminate and face sheet thickness. item t_c Core thickness.

- E_f Young modulus of the face sheet in the Z-direction.

- E_c Young modulus of the core in the Z-direction.

- G_f Elastic shear modulus of the face sheet in the ZY-plane.

- G_c Elastic shear modulus of the core in the ZY-plane.

- G Energy release rate.

- $A_f = bt_f$ is the cross sectional area of the monolithic laminate and sandwich face sheet.

- $A_c = bt_c$ is the cross sectional area of the core.

- $\kappa_d = 5/6$ is the shear correction factor for a rectangular cross section.

- κ_s is the shear correction factor for a bi-material beam having a rectangular cross section and it is defined as following:

$$\kappa_s = \frac{5}{6} \frac{G_f G_c (t_c + t_f)^2}{(G_f t_f + G_c t_c)(G_f t_c + G_c t_f)}. \tag{3}$$

- I_f and I_c are the second moment area of the face and core cross sections about the x-axis.

- $(EI)_s$ and $(GA)_s$ are defined as following:

$$(EI)_s = E_f I_f + E_c I_c \tag{4}$$

$$(GA)_s = (G_f A_f + G_c A_c)\kappa_s \tag{5}$$

- k_t^d, k_t^s, k_r^d and k_r^s are constants defined as:

$$k_t^s = \frac{G_{xy} A_f G_c A_c}{G_c A_c (t_f - \rho) + G_{xy} A_f t_c} \tag{6}$$

$$k_t^d = \frac{2G_{xy} A_f}{t_f} \tag{7}$$

$$k_r^d = \frac{2Pa E_f I_f - 2M_x^d(z=0) E_f I_f}{2M_x^d(z=0)a - Pa^2} \tag{8}$$

$$k_r^s = \frac{2Pa(EI)_s - 2M_x^s(z=0)(EI)_s}{2M_x^s(z=0)a - Pa^2}. \tag{9}$$

24

- c_d and c_s are constants defined as:
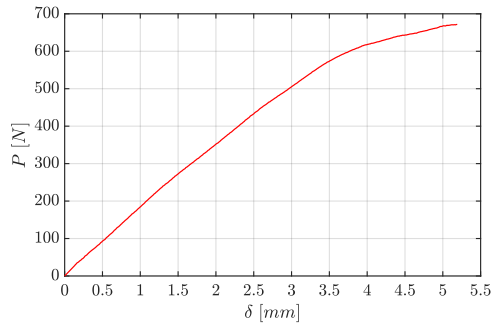
$$c_d = \sqrt{\frac{D_d}{(E\Gamma)_d}} \tag{10}$$

$$c_s = \sqrt{\frac{D_s}{(E\Gamma)_s}} \tag{11}$$

where D_d and D_s are torsional rigidities defined in [26] and $(E\Gamma)_d$ and $(E\Gamma)_s$ are the warping rigidities defined in [26]
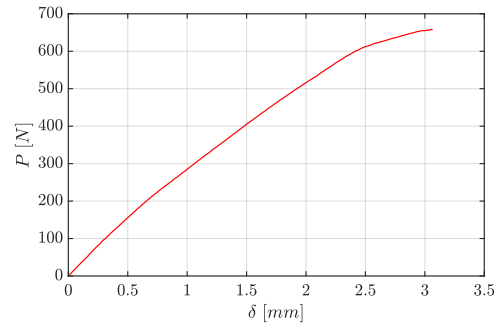
- $M_x^d(z = a)$, $M_x^s(z = a)$ Moment acting along the x-axis on the upper and lower delaminated arms at the crack front.

10. Appendix C

This appendix contains the plots (fig. 21) relative to the experimental tests of foam core sandwich specimens.

25

(a) Specimen 1

(b) Specimen 2

Figures (a) and (b) refers to H80 foam core
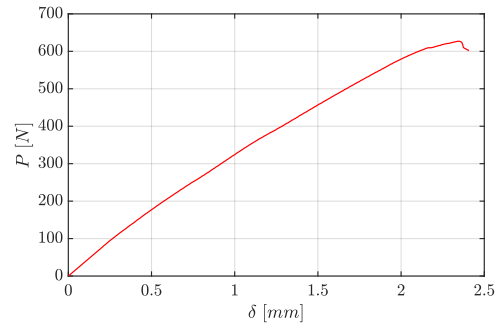

(c) Specimen 3

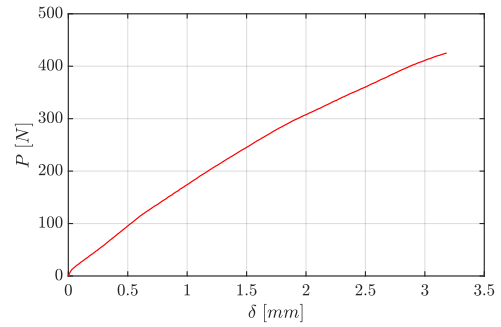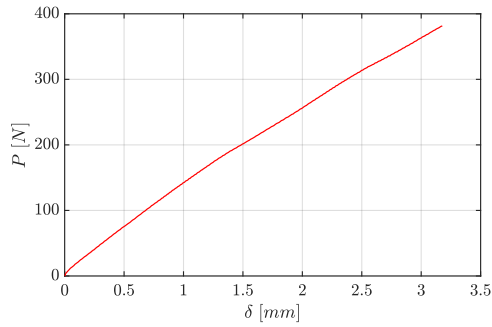(d) Specimen 4

Figures (c) and (d) refers to H80 foam core

(e) Specimen 5
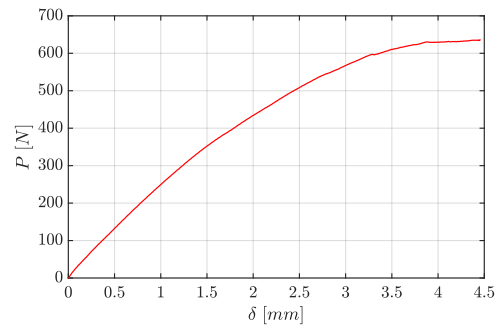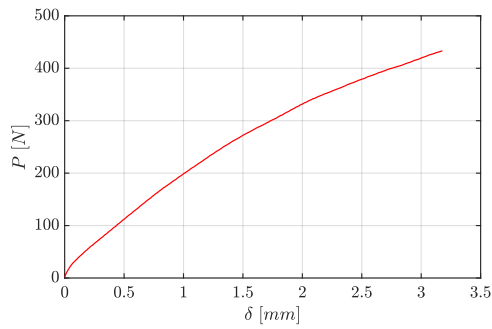

(f) Specimen 6

Figures (e) and (f) refers to H80 foam core

26

121
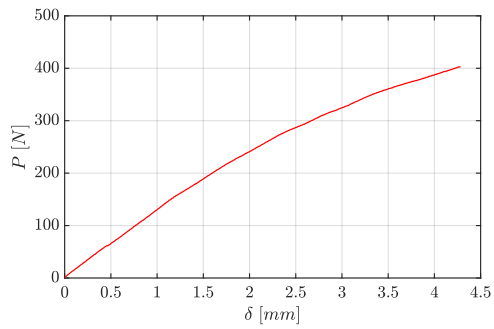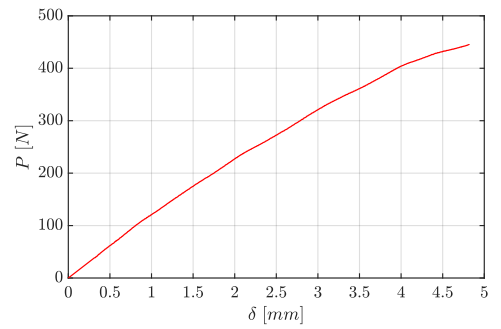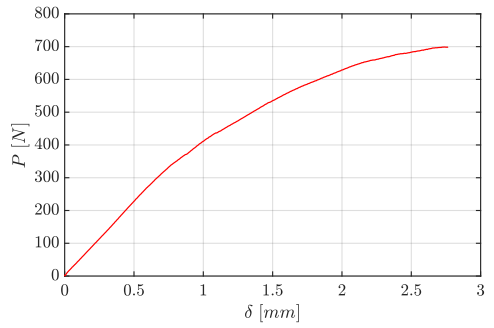
(g) Specimen 7

(h) Specimen 8

Figures (g) and (h) refers to H80 foam core

(i) Specimen 9

(j) Specimen 10

Figure 21: Experimental load vs displacement curve plots of the sandwich specimens tested. Figures (a)-(i) corresponds to specimens having H80 core, instead figure (j) corresponds to H45 foam core.

27

[C1]
Development of a data reduction method for composite fracture characterization under mode III loadings.

DEVELOPMENT OF A DATA REDUCTION METHOD FOR COMPOSITE FRACTURE CHARACTERIZATION UNDER MODE III LOADINGS

P. Sabbadin[1], R. Massabo'[2], and C. Berggreen[3]

[1] Department of Mechanical Engineering, Technical University of Denmark, Kgs. Lyngby, Niels Koppels Alle, Building 404

e-mail: pisabb@mek.dtu.dk

[2] Department of Civil, Chemical and Environmental Engineering, University of Genova, Genova, Italy

e-mail: roberta.massabo@unige.it

[3] Department of Mechanical Engineering, Technical University of Denmark, Kgs. Lyngby, Niels Koppels Alle, Building 404

e-mail: cbe@mek.dtu.dk

Keywords: Debonding, Interface, Fracture Toughness, data reduction method

Abstract. *This work is part of a research aimed at developing a reliable data reduction method for a novel test rig for sandwich composites, which is inspired by the Shear Torsion Bending (STB) rig designed for unidirectional composites. The rig performs fracture characterization tests on pre-delaminated composite sandwich specimens subjected to out-of-plane shear loading. An out-of-plane displacement is applied at the end of the delaminated arms using a hydraulic actuator and the corresponding load is recorded. An analytical equation is required to compute the global value of the energy release rate for an imposed displacement. The preliminary work presented in this paper assumes the material to be quasi-isotropic and linear elastic. The mathematical derivation of the energy release rate relies on Timoshenko Beam Theory and Vlasov theory for non-uniform torsion of beams. The analytical expression is compared with the energy release rate extracted from a 3D FE model of the specimen using the compliance method.*

1   INTRODUCTION

Sandwich structures are considered as key enablers for present and future lightweight structural applications in naval ships because of their superior stiffness/weight and strength/weight ratios compared to traditional metallic concepts as well as monolithic composite materials.

Sandwich composites constitute a wide part of structural components of Naval Vessels. In order to ensure a reliable service, the types of failure associated with composite sandwich materials have to be addressed accurately. The most frequent in-service damage modes are [1-3]: face/core interface debonding, core indentation, core shear failure, face wrinkling, shear crimping, face wrinkling and buckling of the face sheets or of the core. These damages can severely weaken a structural component and compromise its functionality.

One of the most common and severe types of damage is the lack of adhesion between the face sheets and the core commonly known as a "debond". Several in-service collapses have been attributed to the presence of debonds, such as: the structural failure of an airplane rudder [4], of a fuel tank in the aerospace sector [5] and of wind turbine blades under cyclic loading [6]. Therefore, the debond properties of the face/core interface must be characterized in order to provide an assessment of the structural life of a damaged component.

The strength of the bonding interface is assessed measuring the energy required to separate the face-sheet from the core, which is usually addressed as interface fracture toughness and depend on the mode-mixity conditions between the different fracture modes. Studies done in [4-6] consider debonds subjected to multiaxial stress states where out-of-plane shear loadings are present at the debond front. Different studies have been carried out [8-15] in order to measure the fracture toughness of monolithic composites when the debond front is subjected to out-of-plane shear loading.

Experimental methods have been developed for evaluating the fracture toughness G_c under mode III conditions in monolithic composite laminates: the edge crack torsion [8] (ECT), the modified split cantilever beam (MSCB) [9] and the shear bending torsion (SBT) [10] tests. The ECT test consists of a cracked plate subjected to a twisting couple that generates a distribution of out-of-plane stresses along the debonded front. The MSCB test uses a specimen with a pre-cracked beam-like geometry. In this test, two transverse forces are applied to the cracked arms in order to create out-of-plane stresses along the crack front. The ECT and MSCB tests generates a stress field that is not uniformly distributed and presents some undesired contributions related to mode II loading of the lateral parts of the crack front, as observed in [11-12]. Hence, the fracture energy computed using data reduction methods developed for these tests is associated to a certain mode-mixity between mode II and III. Similarly to the MSCB test, the SBT proposed in [10] uses a pre-cracked specimen with a beam-like geometry. However, the specimen is loaded using two stiff load blocks attached at the end of the delaminated arms, which can slide while preventing the end rotations. These loading conditions, along with two longitudinal notches in the intact part of the specimen, favor a uniform distribution of out-of-plane shear stresses along the crack front and therefore more uniform Mode III conditions at the crack tip.

The data reduction method used in [10] for the STB test is applicable only to specific specimen geometry and crack length. The equation of the energy release rate presents some global coefficients, which have been derived numerically and globally account for different effects.

The work presented in this paper is part of a project aimed at developing a reliable data reduction method for the novel test rig presented in [16], which is inspired to the STB test rig for monolithic composites. The test rig applies an out-of-plane shear loading to a pre-debonded

127

sandwich specimen in order to propagate the debond. The physical quantities measured during the test are: the force resultant P (expressed in [N]) and the total out-of-plane displacement Δ (expressed in [mm]). An expression is required to compute the energy release rate in order to define the fracture toughness G_c from experimental measurements. In this paper, the formulation for the closed form derivation of the energy release rate in a homogeneous specimen is presented.

2 METHOD

A data reduction method for fracture toughness characterization consists in an analytical equation for the energy release rate. The equation takes into account the geometrical and material parameters, the applied loads and boundary conditions. The Mode III fracture test rig is presented with the main geometrical parameters in fig. 1. The rig consists in a pre-cracked composite specimen and two steel load tabs are attached to the cracked part of the specimen. Two different widths are considered as it is shown in fig. 1: b is the specimen width and W is the width of the intact interface ahead of the crack front where two longitudinal cuts have been introduced. W is the geometrical parameter, which define the fracture surface when the crack is propagating of a quantity Δa. The two faces have the same thickness t_f and the crack length a is the distance between the end of the load tab and the crack tip. L is the total specimen length and h_{tab} is the height of each load-tab.
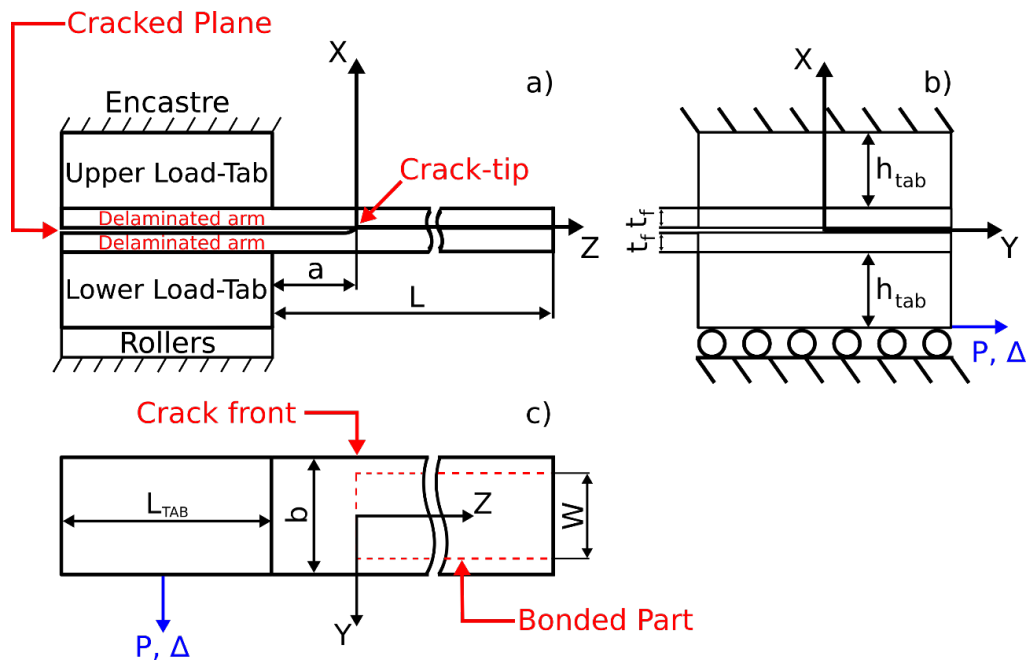

Figure 1: (a) (b) Specimen and load tab side views; (c) top view

An out-of-plane load P, or the corresponding displacement Δ, is applied to the specimen through the lower load-tab. The points on the lower-tab surface can only translate in the Y direction, while points on the upper-tab surface are fixed. The load tabs prevent displacements

and warping of the arm cross section located at $Z = -a$. The intact part of the specimen is traction free and it follows rigidly the displacements/rotations of the delaminated arms.

A reaction force P^R arises at the upper load-tab, along the Y-direction, which is equal and opposite to P in order to satisfy equilibrium. A reaction moment M_Z^R arise along the Z-direction on the surface of each load tab, since the load tabs do not allow specimen rotations along the Z-axis. Moreover, reaction moments along the X-axis, M_X^R, arise on the surface of each load tab because the load tabs do not allow rotations of the specimen along the X-axis.

The internal loads, reported at the cross-section shear center, consist of two out-of-plane shear forces $V_Y = P$, a moment $M_Z = P t_f / 2$ with vector axis-Z and a moment $M_X(z)$ with vector axis-X in the two delaminated arms. Where the two cracked arms join at the crack front, internal moments and forces must constitute an auto-equilibrated system since the intact part of the specimen is traction-free. The two moments M_X have opposite directions and same modulus; the two shear forces V_Y generate a moment in the Z-direction which equilibrate the sum of the two moments M_Z.

The upper cracked arm of length a is modelled as a Timoshenko beam (see fig. 2a) in order to analyze the contributions to the energy release rate resulting from the bending moment M_X and shear force V_Y. The torsional contribution (see fig. 2b) to the energy release rate due to M_Z is studied separately. In this case, the beam is subjected only to an external concentrated moment $M_t = P t_f / 2$ at its right end. The left end of the beam is torsionally clamped in fig. 2b.

The new coordinate system, x-y-z, in Fig. 2 has origin at $Z = -a$. The material is assumed to be quasi-isotropic in the yz-plane and linear elastic. The displacement δ is equal to $\Delta/2$ and refers to only one beam. Two elastic springs of stiffnesses k_r and k_t are introduced at $z = a$ to describe, through a structural mechanics approximation, the compliance of the material ahead of the crack front.
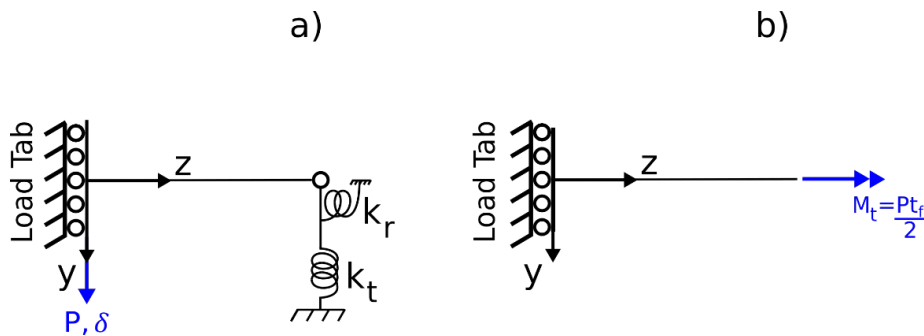
a)   b)

Figure 2: a) Structural scheme for one cracked arm modelled as a Timoshenko beam and b) subjected to a torque moment in the yz-plane.

The rotational spring of stiffness k_r in introduced to account for the crack-front root rotations [17], while the translational spring, of stiffness k_t, describes the shear deformations of the material ahead of the crack front in the xy-plane. The constant k_r is expressed in this work

following the analytical derivation in [18, 19] and referring to the strain-energy decay in the intact part of the specimen.

The equations of a Timoshenko beam in the yz-plane are:

$$\begin{cases} (E_z I_{xx})\dfrac{d^3\varphi}{dz^3} = 0 \\ (E_z I_{xx})\dfrac{d^2\varphi}{dz^2} = G_{yz} A_s\left(\dfrac{du_y}{dz}+\varphi\right). \end{cases} \tag{1}$$

The terms in Eq. (1) are: E_z is the Young modulus of the beam in the z direction, I_{xx} the second area moment of inertia about the x-axis, $\varphi(z)$ is the rotation of the beam section around the axis x-axis, G_{yz} is the shear elastic moduli in the yz-plane, $u_y(z)$ is the displacement in the y direction, $A_s = bt_f\kappa_s$ is the shear area which includes a shear correction factor. The bending moment M_x and out-of-plane shear V_y are related to the generalized displacements by the constitutive equations as follows:

$$M_x = \left(E_z I_{xx}\right)\frac{d\varphi}{dz} \tag{2}$$

$$V_y = G_{yz} A_s\left(\frac{du_y}{dz}+\varphi\right). \tag{3}$$

The following boundary conditions are applied to Eq. (1):

$$\begin{cases} \varphi(z=0)=0 \\ V_y(z=0)=G_{yz}A_s\left(\dfrac{du_y}{dz}(z=0)+\varphi(z=0)\right)=P \end{cases} \quad \begin{cases} \varphi(z=a)=-\dfrac{M_x(z=a)}{k_r}=-(E_z I_{xx})\dfrac{d\varphi}{dz}(z=a) \\ u_y(z=a)=-\dfrac{V_y(z=a)}{k_t}=-\dfrac{G_{yz}A_s}{k_t}\left(\dfrac{du_y}{dz}(z=a)+\varphi(z=a)\right). \end{cases} \tag{4}$$

and the analytical expressions for $M_x(z)$, $V_y(z)$, $\varphi(z)$ and $u_y(z)$ are found in closed form.

The torsion problem is analyzed using Vlasov theory for non-uniform torsion [20] since the left beam end is not free to warp. The problem of non-uniform torsion is governed by the following differential equation:

$$\frac{d^4\theta_z}{dz^4}-c^2\frac{d^2\theta_z}{dz^2}=0 \quad \text{where} \quad c=\sqrt{\frac{G_{yz}J}{E_z\Gamma}} \tag{5}$$

where $\theta_z(z)$ is the angle of twist of the beam section around the z-axis; J is the torsional rigidity of the beam cross section and Γ is the warping rigidity for the given cross section. For a thin rectangular cross section of area A, the torsional and warping rigidities are defined as follows:

$$J = \frac{bt_f^3}{12} \qquad \Gamma = \iint (\psi)^2 \, dA = \frac{b^3 t_f^3}{144} \tag{6}$$

where ψ is the warping function [20]. The internal torque moment M_z is related to θ_z by the constitutive equation:

$$-\frac{d^3\theta_z}{dz^3} + c^2 \frac{d^2\theta_z}{dz^2} = \frac{M_z}{E_z \Gamma}. \tag{7}$$

The following boundary conditions are applied to eqs. (5) in order to find the close solution of the problem:

$$\begin{cases} \theta_z(z=0) = 0 \\ \dfrac{d\theta_z}{dz}(z=0) = 0 \end{cases} \begin{cases} \dfrac{d^2\theta_z}{dz^2}(z=a) = 0 \\ -\dfrac{d^3\theta_z}{dz^3}(z=a) + c^2 \dfrac{d\theta_z}{dz}(z=a) = \dfrac{M_t}{E_z \Gamma} \end{cases} \tag{8}$$

The boundary condition $\dfrac{d\theta_z}{dz}(z=0) = 0$ imposes that the displacements in the z direction of all points of the cross section at $z = 0$ are zero (because the beam is torsionally clamped at the load tab) [20]. The boundary condition $\dfrac{d^2\theta_z}{dz^2}(z=a) = 0$ imposes that at $z = a$ the secondary normal stresses, induced by preventing the section warping, are zero [20]. The fourth boundary condition imposes that the internal torque moment at z=a $M_z(z=a)$ has to be equal to the concentrated moment applied M_t at the right end of fig. 2b.

The solution is:

$$\theta_z(z) = \frac{M_t a}{G_{yz} J} \left(\frac{z}{a} - \frac{e^{cz} + e^{2cza}(1 - e^{-cz}) - 1}{ac(1 + e^{2ca})} \right). \tag{9}$$

The analytical expression for the specimen compliance $C_{analytical}$ can be expressed as follows:

$$C_{analytical} = \frac{\Delta}{P} = \frac{2 \cdot \left(u_y(z=0) + \theta_z(z=a) \cdot t_f / 2 \right)}{P} \tag{10}$$

131

where $u_y(z=0)$ and $\theta_z(z=a)$ are linear functions of the external applied load P. The term $\theta_z(z=a)\cdot t_f/2$ in eq. (10) is present due to the twist of the beams sections at $z=a$ induced by the torque moment M_t (see fig. 3). The angle of twist θ_z causes a displacement equal to $\theta_z(z=a)\cdot t_f/2$ in the y-direction of the beam cross section center as depicted in fig. 3.
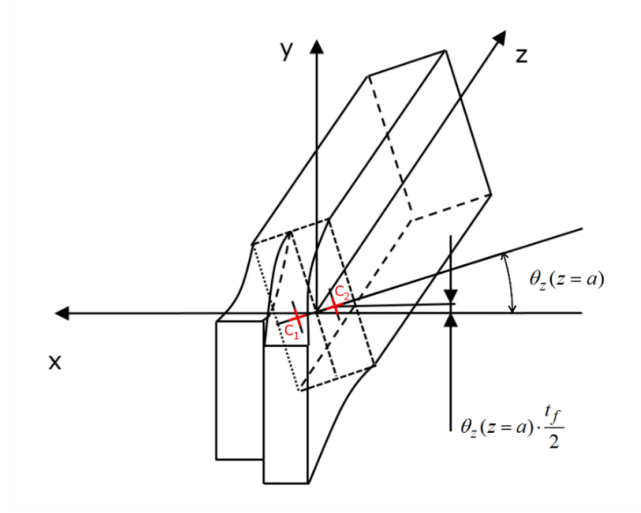

Figure 3: Deformed configuration of the specimen. The torsional deformation contributes to an additional displacement of section geometrical centers of the beams (C_1 and C_2 represented in red) at $z=a$, where the delaminated arms join.

The energy release rate is calculated from the total potential energy Π:

$$\Pi = U_{tot} - L_{ext} \tag{11}$$

where the total strain energy U_{tot} is given by the sum of five contributions in the two beams: the energies due to bending, out-of-plane shear, torsion and the elastic energy stored in the two linear elastic springs.

$$U_{tot} = 2\left(\int_0^a \frac{(M_x(z))^2}{2(E_z I_{xx})}dz + \int_0^a \frac{(V_y(z))^2}{2(G_{yz}A_s)}dz + \int_0^a \frac{(M_z(z))^2}{2}\frac{d\theta_z}{dz}dz + \frac{1}{2}k_t\left(u_y(a)\right)^2 + \frac{1}{2}k_r\left(\varphi(a)\right)^2 \right) \tag{12}$$

The work done by the external forces and moments is:

$$L_{ext} = P \cdot u_y(z=0) + 2M_t \cdot \theta_z(z=a) = P \cdot u_y(z=0) + Pt_f \cdot \theta_z(z=a) \tag{13}$$

Thus, the energy release rate is defined as the variation of the total potential energy due to a unit crack area extension:

$$G^{analytical} = -\frac{1}{W}\frac{d\Pi}{da} \tag{14}$$

where W is the specimen width linked to the cracked surface area (see figure 1).

A 3D FE model is formulated in order to verify the accuracy of the analytical solution. The FE model, shown in fig. 4, is solved in Abaqus 2016 and is composed of $70 \cdot 10^3$ brick elements having quadratic shape functions (Abaqus element C3D20). Loads and BC are applied in order to reproduce fig. 1. The assumed geometry is: $t_f = 2\,mm$, $b = 30\,mm$, $W = 26\,mm$, $L = 160\,mm$, $L_{tab} = 60\,mm$, $h_{tab} = 10\,mm$.

The global value of the energy release rate is extracted from the FE model using a compliance based-method, with the compliance $C_{FE} = \Delta / P$.

The compliance C_{FE} is extracted for different values of crack lengths from the FE model and the energy release rate is defined by considering the variation of the specimen compliance C_{FE} with respect to the crack length a. The energy release rate is:

$$\mathcal{G}^{FE} = \frac{P^2}{2W} \frac{\partial C_{FE}}{\partial a} \tag{15}$$

Numerical analyses are carried out on a glass fiber reinforced laminate (GFRP). The material is modelled as homogeneous and orthotropic with a linear elastic behavior. The load tabs are made of steel, which is treated as linear elastic. Material properties are listed in Table 1.

Material	Elastic Moduli [GPa]						Poisson′s ratios		
	E_x	E_y	E_z	G_{yx}	G_{zx}	G_{zy}	v_{yx}	v_{zx}	v_{zy}
GFRP (-45, 90, 45, 0)	9.5	19.8	19.8	2.9	2.9	7.5	0.43	0.37	0.39
Steel (load tabs)	209	209	209	80.4	80.4	80.4	0.3	0.3	0.3

Table 1: Material properties used in the numerical analyses. The GFRP properties are measured experimentally following [21-22].
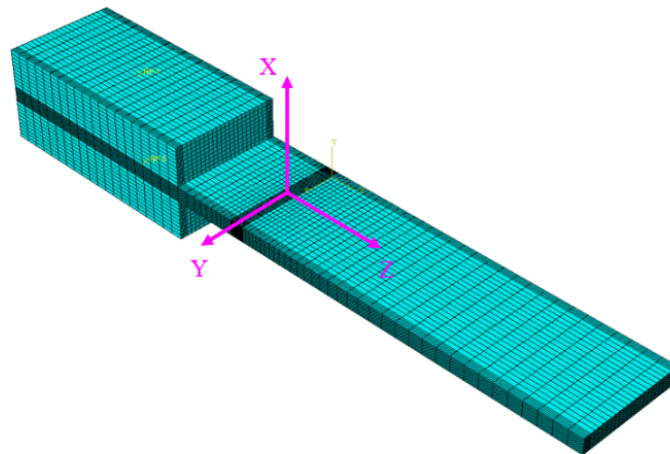

Figure 4: FE model geometry.

3   RESULTS

The analytical eq. (14) expresses the analytical value for the energy release rate $G^{analytical}$. Values for $G^{analytical}$ are compared with the numerical values G^{FE} of the global energy release rate, calculated using (15), fig. 5. The diagram displays how the dimensionless energy release rate varies on varying the normalized crack length, a/t_f. The relative difference between the energy release rate, computed with the analytical model and the one from the FE model is reported in table 2 for different crack lengths. The maximum relative difference between the analytical and the numerical curve is 1.9 % for $a = 20\,mm$. Table 2 shows that for increasing values of the normalized crack length a/t_f the relative difference between the analytical and numerical energy release rate decreases.

Furthermore, the plot shows that when G is a decreasing function of the crack normalized crack length a/t_f. Therefore, the crack propagation is stable if the test is performed in displacement control.
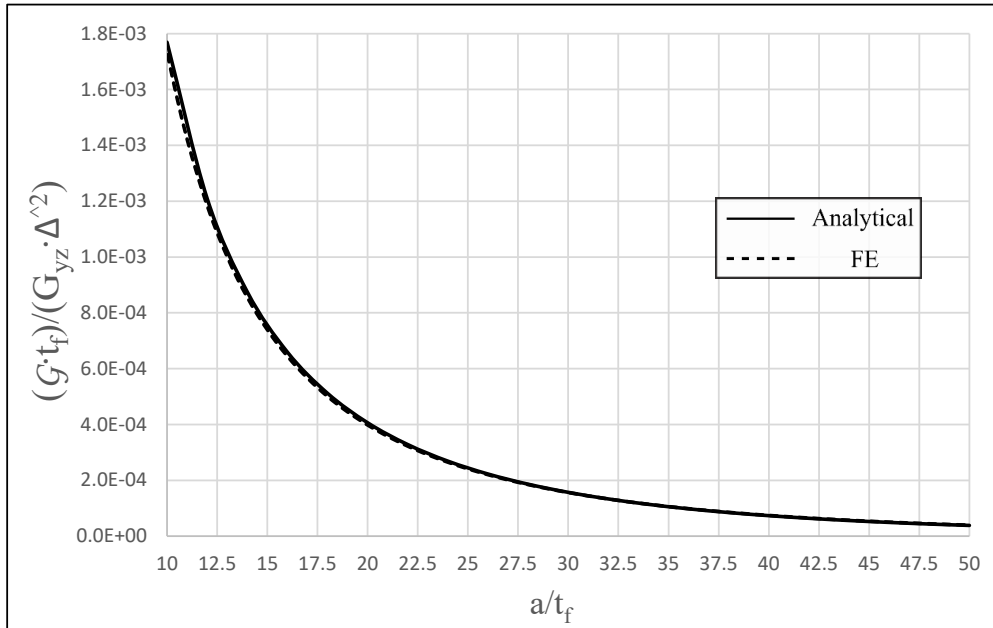

Figure 5: Comparison between analytical and numerical dimensionless energy release rate vs. normalized crack length for a GFRP monolithic laminate.

$t_f\,[mm]$	a/t_f	b/t_f	W/t_f	$\left(G_\Delta^{analytical} - G_\Delta^{numerical}\right)/G_\Delta^{analytical}\;[\%]$
2	10	15	13	1.9
2	25	15	13	1.3
2	40	15	13	1.2

Table 2: Relative difference between energy release rates computed analytically (eq. 14) and numerically (eq. 17) for different crack lengths.

4   CONCLUSIONS

An analytical expression for the global energy release rate $\mathcal{G}$ is derived for a cracked composite specimen subjected to out-of-plane shear. The analytical model is derived using Timoshenko beam theory and Vlasov theory for non-uniform torsion of elastic beams. The expression of $\mathcal{G}$ can be used as data reduction method for the fracture test presented in [16]. The analytical equation of $\mathcal{G}$ takes into account the influence of all the geometrical/material parameters of the specimen. It is possible to highlight clearly each contribution to the energy release rate, coming from the applied loads and boundary conditions. The main difference, with the equation for $\mathcal{G}$ derived in [10], is that the equation derived in this work is purely analytical and it does not include coefficients calibrated on a numerical model.

The analytical expression of $\mathcal{G}$ is particularized to a glass fiber monolithic laminate, under the assumptions of linear elasticity and quasi-isotropic material behavior in the laminate plane, and is compared with 3D FE results. The comparison, between the analytical and the FE results shows a maximum relative difference of 2.7%. Moreover, the analytical model predicts a stable crack growth if the fracture test in [16] is carried out in displacement control mode.

5   ACKNOLEDGEMENTS

REFERENCES

[1]   L. A. Carlsson and G. A. Kardomateas, *Structural and Failure Mechanics of Sandwich Composite.* Springer Science & Business Media, 2011.

[2]   D. Zenkert, *An Investigation to Sandwich Construction.* Chamaleon Press, London, 1995.

[3]   Christian Berggreen. *Damage Tolerance of Debonded Sandwich Structures*. PhD thesis, Technical University of Denmark, 2004.

[4]   T. S. B. of Canada (TSB), "Loss of rudder, Airbus 310-308, Air Transat Flight 961," 2005.

[5]   E. H. Glaessgen, J. R. Reeder, D. W. Sleight, J. T. Wang, I. S. Raju and C. E. Harris, "Debonding failure of sandwich-composite cryogenic fuel tank with internal core pressure", *Journal of spacraft and rockets,* vol. 42, no. 4, pp. 613-627, 2005.

[6]   U. Vantini, *Investigating Effects of Pure Shear Deformation in Wind Turbine Blade Substructures*, Master's Thesis, Politecnico di Milano, 2014.

[8]   Lee SM. An edge crack torsion method for mode III delamination fracture testing, *J Compos Technol,* Res 1993;**15(3)**:193-201.

[9]   Szekrényes A. Improved analysis of the modified split-cantilever beam for mode-III fracture, *Int J Mech Sci* 2009;**51(9-10)**:682-93.

[10] Barry D. Davidson, Felipe O. Sediles, Mixed mode I-II-III delamination toughness determination via shear-torsion-bending test, *Composites Part A-applied Science and Manufacturing* — 2011, Volume **42** Issue 6, pp. 589-603.

[11] Ratcliffe JG. Characterization of the edge crack torsion (ECT) test for mode III fracture toughness measurement of laminated composites, NASA-TM-2004-213269; 2004.

[12] De Morais AB, Pereira AB, De Moura MFSF, Magalhaes AG. Mode III interlaminar fracture of carbon/epoxy laminates using the edge crack torsion (ECT) test, *Compos Sci Technol* 2009;69(5):670–6.

[13] Pennas D, Cantwell WJ, Compston P. The influence of strain rate on the mode III interlaminar fracture of composite materials, *J Compos Mater* 2007;41(21):2595–614.

[14] Robinson P, Song DQ. The development of an improved mode III delamination test for composites, *Compos Sci Technol* 1994;52(2):217–33.

[15] Cicci D, Sharif F, Kortschot MT. Data reduction for the split cantilever beam mode III delamination test. Fatigue and fracture, *In: Proceedings of the 10th International conference on composite materials*, vol. 1. (ICCM-10), British Columbia; Canada; August 14–18 1995. p. 189–96.

[16] P. Sabbadin, C. Berggreen, B.N. Legarth, "Development of a Mode I/II/III Test Fixture for Composite Laminates and Sandwich Face/Core Fracture Characterization", in Proceedings of 12th International Conference on Sandwich Structures, Lausanne, 19 August 2018, pp. 35-37.

[17] L. Barbieri, R. Massabo', C. Berggreen, "The effects of shear and near tip deformations on interface fracture of symmetric sandwich beams" *Journal of Composites Technology and Research*, Vol 201, 2018, pp. 298-321.

[18] R. Olsson, "A simplified improved beam analysis of the DCB specimen" *Composites Science and Technology*, Vol 43, 1992, pp. 329-338.

[19] C. O. Horgan, "On Saint-Venant's principle in plane anisotropic elasticity" *J. Elast.,* Vol 2, 1972, pp. 169-180.

[20] V.Z. Vlasov, *Thin-Walled Elastic Bars,* 2nd ed., Fizmatgiz, Moscow, 1959.

[21] Standard Test Method for Tensile Properties of Polymer Matrix Composite Materials, *ASTM D3039/D3039M – 17.*

[22] Standard Test Method for Shear Properties of Composite Materials by V-Notched Rail Shear Method, *ASTM D7078/D7078M – 12.*